University of Minho
School of Sciences

Tiago Vieira de Castro Martins Antão

Disorder and Topology in Spin Systems

september 2023

Disorder and Topology in Spin Systems
Tiago Antão
UMinho | 2023

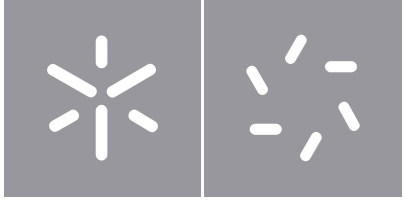

University of Minho
School of Sciences

Tiago Vieira de Castro Martins Antão

Disorder and Topology in Spin Systems

Masters Dissertation
Physics

Dissertation supervised by
Doctor Nuno Miguel Machado Reis Peres

september 2023

Copyright and Terms of Use for Third Party Work

License granted to users of this work:

Acknowledgements

The work presented in this Master's thesis is the fruit of more than one year of labor and more than five years of study at the University of Minho, which would not have been possible without the personal and institutional support given by many people along the way.

I thank especially my supervisor Dr. Nuno Peres for teaching me many years ago that the dream of becoming a theoretical physicist could become a reality and for all his help and guidance in achieving this dream ever since. His patient and attentive attitude, together with his willingness to have long discussions which often prolonged themselves into late hours of the night have made a huge impact on my journey.

I acknowledge also Dr. Bruno Amorim, Dr. Eduardo Castro and Miguel Oliveira for helpful discussions in the topic of dilution, João Carlos Henriques, for discussions regarding topology, spin systems and Floquet theory, Miguel Peixoto, Gabriela Jordão and Fábio Carneiro for helpful tips about numerics, Daniel Miranda for discussions about quasidisorder and 1D models, and Dr. António Costa and Dr. Joaquín Fernández-Rossier for helpful comments.

Additionally, it would be impossible to have performed this work without the help and support from my family, especially my mother and her partner, together with my grandparents, who have always cultivated and supported my passion for physics. I would also like to thank Vitória for her unconditional love, patience and company, and for putting up with my physics related ramblings during the past five years. During all this time, I could not have asked for a better friend and partner. I also thank the friends I made during this journey, especially Marcelo Barreiro and Francisco Lobo.

I finally acknowledge specifically the Department of Physics of the University of Minho for the continued support and the Laboratory of Experimental Particle and Astroparticle Physics (LIP) for the hospitality extended toward me in the final year of my Master's degree, when most of the work presented in this thesis was conducted. Lastly, I acknowledge support and funding from the Portuguese Foundation for Science and Technology (FCT) in the framework of the project CERN/FIS-COM/0004/2021.

Statement of Integrity

I hereby declare having conducted this academic work with integrity.

I confirm that I have not used plagiarism or any form of undue use of information or falsification of results along the process leading to its elaboration.

I further declare that I have fully acknowledged the Code of Ethical Conduct of the University of Minho.

University of Minho, Braga, september 2023

Assinado por: **Tiago Vieira de Castro Martins Antão**
Num. de Identificação: 13964160
Data: 2023.09.07 16:16:09+01'00'

CHAVE MÓVEL

Tiago Vieira de Castro Martins Antão

Abstract

Topological materials have gathered attention since the turn of the century due to the presence of several desirable properties such as chiral edge modes resilient disorder. Additionally, 2D magnetic materials have proven to have several desirable properties for implementation in spintronic devices. In the work presented in this thesis, the band-topological properties of certain 1D and 2D magnetic materials are explored, and the resilience and manipulation of these materials is probed, resorting to three types of real space disorder. Firstly, I present a novel way to manipulate topological properties of photo-induced topological ferromagnets using a strain engineering approach, with potential application in all-strain engineered topological spintronics. Secondly, I present a novel quasidisordered toy model showcasing for the first time the coexistence of 1D and 2D topological invariants in a purely 1D physical system. Such a system may be realizable in the context of spin systems and beyond. Lastly, some numerical and semi-analytical results on the impact of dilution in topological ferromagnets are presented, showcasing the resilience of topology to substitutional effects when a percentage of magnetic atoms is replaced by non-magnetic ones.

Keywords Band topology, Spin systems, Magnons, Haldane model, SSH model, Strain, Quasicrystals, Dilution

Resumo

Os materiais topológicos têm suscitado interesse desde o virar do século devido à presença de várias propriedades desejáveis, tais como modos de fronteira quirais resistentes à desordem. Além disso, materiais magnéticos 2D têm demonstrado ter várias propriedades desejáveis para implementação em dispositivos na área da spintrónica. No trabalho apresentado nesta tese, são exploradas as propriedades topológicas de banda de certos materiais magnéticos 1D e 2D, bem como a resiliência e manipulação desses materiais, recorrendo a três tipos de desordem no espaço real. Em primeiro lugar, apresento uma forma inovadora de manipular as propriedades topológicas de sistemas ferromagnéticos topológicos iluminados por lasers usando uma abordagem de engenharia de deformação ou strain, com potencial aplicação em spintrónica e magnónica topológica controlada inteiramente por deformações. Em segundo lugar, apresento um novo modelo quasi-desordenado simples, mostrando pela primeira vez a coexistência de invariáveis topológicos 1D e 2D num sistema físico puramente 1D. Este é realizável no contexto de sistemas de spin entre outros. Por último, são apresentados alguns resultados numéricos e semi-analíticos sobre o impacto da diluição em sistemas ferromagnéticos topológicos, demonstrando a resiliência da topologia aos efeitos de substituição quando uma percentagem de átomos magnéticos é substituída por átomos não magnéticos.

Palavras-chave Topologia de bandas, Sistemas de Spin, Magnões, Modelo de Haldane, Modelo SSH, Deformação, Quasicristais, Diluição

Published papers in peer-reviewed journals

During the course of this Master's thesis, the following works were published in peer reviewed journals:

1. Laser induced enhanced coupling between photons and squeezed magnons in antiferromagnets, J. C. G. Henriques, **T. V. C. Antão**, N. M. R. Peres Phys.: Condens. Matter **34** 245802 (2022)

2. Strain engineering of photoinduced topological phases in two-dimensional ferromagnets, **T. V. C. Antão**, J. C. G. Henriques, N. M. R. Peres Phys. Rev. B. **107**, 235410 (2023)

Two additional preprints are currently in preparation:

1. Coexistence of 1D and 2D topology and genesis of Dirac cones in the chiral Aubry-André model, **T. V. C. Antão**, Daniel Miranda, N. M. R. Peres (Unpublished)

2. Effects of dilution in a 2D topological magnon insulator, Miguel Oliveira, **T. V. C. Antão**, Eduardo Castro, N. M. R. Peres (Unpublished)

Contents

Part I

Introductory material

Chapter 1

Introduction

1.1 Motivation and outline

Condensed matter physics has changed dramatically since the 1980s and 1990s when it was realized that topology has a significant role to play when analyzing even the some of the simplest models imaginable for matter in the solid state [1, 2, 3, 4, 5, 6]. The community surrounding topological aspects of condensed matter has been growing quickly ever since, and interest in the subject is still rising to this day, as topological properties of materials are of immense interest both from a theoretical perspective and for the sake of the development of new and efficient technologies.

Indeed, the case of topology is perhaps one of the main counterexample to a famous quote attributed to the Nobel laureate condensed matter physicist Philip W. Anderson, which states that "It is only slightly overstating the case to say that physics is the study of symmetry". This quote was written in the 1972 in the seminal paper "More is Different" [7], a decade before several experimental and theoretical discoveries and predictions over the remainder of 20th century, revealed that symmetry does not paint a complete picture of condensed matter physics, and about 5 years before Anderson was awarded the Nobel prize for "his investigations into the electronic structure of magnetic and disordered systems". Among these intriguing discoveries are the first experiments realizing the quantum Hall effect by Von Klitzing, and the theoretical description of this phenomena in terms of a topological invariant by Thouless and colleagues in the famous TKNN paper [1], in what is perhaps the most striking and celebrated example of the application of topological concepts to condensed matter, at least in this nascent period for the field.

In current times, topology has permeated every corner of the realm of quantum materials, spurred by the advent of topological superconductors [8] and insulators [9], and it manifests in many different physical phenomena: ranging from the presence of chiral conducting edge states in topological band insulators, to the integer and fractional quantum hall effects, to the possibility of engineering fault-tolerant quantum computational devices reliant on braiding of excitations of topological origin. Topology has really become a

staple of condensed matter physics, and the ability to generate, manipulate, simulate and apply topological properties of matter to concrete physical and technological applications is now a well established but still fresh and exciting field for those interested in harnessing the amazing quantum properties of materials.

Magnetism, unlike topology, has always been regarded as an important subject within solid state physics, with the growth of the field as it is known today due in part to the effort and development of the statistical mechanics and thermodynamics of magnetic materials. The quantum origin of magnetism has long been understood, but since the dawn of low-dimensional matter, 1D and 2D quantum spin systems have gained traction as a promising area for exploring novel solid state phenomena, essentially making up the theoretical building blocks a wide range of magnetic chains, or one-atom thick materials. Quantum spin models have a particularly captivating property for theorists, in that even the models with the simplest Hamiltonians have extremely rich physics. In particular, low-dimensional spin systems (in one or two dimensions) have proved to be interesting in many regards, since sometimes they are exactly solvable and yet describe complex physical behaviors. From Ising [10] or Heisenberg models [11], to XY or XXZ models, to systems exhibiting magnetic frustration [12], valence bond solids [13, 14], quantum spin liquids [15], Kitaev magnets [16], and many others, some of which host a variety of excitations such as magnons, spinons and visons [17], skyrmions [18], etc. Magnetic materials also host a wide range of applications, ranging from solid state memory, to information transfer and processing in the form of spintronics, to medical applications, such as nuclear magnetic resonance, and beyond [19, 20].

The intersection of magnetic models with topology is made manifest in many seminal works. For instance, the Lieb-Schultz-Mattis theorem [21], and the Haldane conjecture established firm connections between the ground state properties of integer and half-integer spin chains and topology, with important spin chain models such as the AKLT chain models hosting phases of topological nature [22, 23, 24, 25] showcasing prime examples of the theorem. The work of Kitaev and the models attributed to his namesake, both in superconductors [8] and spin systems [16], are also examples of using topologically non-trivial spin systems for the development of platforms for fault-tolerant quantum computation [26, 27, 16]. Quantum spin liquids are also known to realize topologically ordered phases of matter, hosting abelian anyons [17]. Exactly solvable models, such as the XY model, host complex phase transitions defying the traditional symmetry-breaking classifications, having been described with a topological framework by Kosterlitz and Thouless [28]... and the list goes on.

The focus of this thesis lies mostly within the single-particle topology of tight-binding models (TBMs): in particular, I will focus on how to harness the complex behavior of spin systems and their topology using degrees of freedom both intrinsic and external to the underlying magnonic TBM. The title of this thesis

encapsulates all of the approaches I aim to describe under the umbrella of disordered spin systems, but more precisely, I will focus on exploring and creating novel methods for generating and controlling band-topological properties of magnons, or spin-wave excitations, in low-dimensional magnetic materials. The main objective is to address the prospect of manipulating single-particle topology using three new and distinct approaches, namely: straining, modulating and diluting. I aim to give a comprehensive understanding of some aspects of the manipulation of topological properties of spin systems using these methods, while emphasizing the new results stemming from each of the approaches mentioned here.

The mathematical, numerical, and physical methods employed during this thesis cover fairly wide ground, ranging from more traditional numerical and analytical approaches reliant on reciprocal space and Green's functions techniques, to recent advances in real space methods such as topological markers and Floquet theory. For this reason several Appendices are included, covering some of the methods. Using all of these tools, the main focus will always be on describing how the considered effects result in changes for topological invariants, which characterize the distinct topological phases of matter beyond Landau's symmetry breaking paradigm [29].

The thesis is organized in the following manner:

- In the remainder of **Chapter 1**, I will describe the basic concepts of spin systems, and topology. I will focus, at first, on magnetism, and on a particular type of spin excitation occurring in magnetic systems, called magnons, or quantized spin-waves, establishing the role of low-dimensional spin systems in this story as well. I will then move into a description of topology, introducing the concept of the geometric phase in electromagnetism and band topology. In the context of electromagnetism I will introduce the Aharonov-Bohm and Aharonov-Casher effects, the first of which is crucial for understanding the Quantum Hall effect playing a role in Chapter 4, and the second of which will also play a major role in Chapter 3.

- In **Chapter 2** I will introduce the two most relevant topological models for this thesis, namely the one-dimensional SSH chain and the two-dimensional Haldane honeycomb model, which host topological invariants called the winding number, and the Chern number, respectively. I will also describe how these systems can be realized in spin systems, and how in particular for the ferromagnetic SSH model, the spin realization can be qualitatively different from the electronic SSH model.

- In **Chapter 3**, I will consider the effects of coupling of a time-periodic external field to a spin system. Using these ideas, I propose a new method of using mechanical strain to deform atomic

bonds and improve the manipulation of topological phases of 2D photo-induced topological magnon insulators. I will show that straining a two-dimensional honeycomb ferromagnet can lead to changes in the topological invariant, even for small values of an applied electric field, and in turn, for high enough values of electric field, small amounts of strain can lead to switches in topological invariant, enabling the possibility of implementing strain engineered topological magnonic and spintronic devices.

- In **Chapter 4**, I introduce the concept of a quasicrystal and study how incommensurate potentials and quasi-disorder can affect spin systems. I propose a new toy model based on the SSH chain and the celebrated Aubry-André models, reliant on quasiperiodic disorder. The Aubry-André models are a form of quasicrystal based on incommensurate modulation of on-site potentials or hopping strengths, and I show how the proposed toy model hosts, in a physical purely one-dimensional realization, coexistence of one-dimensional winding number invariant and two-dimensional Chern number. I will also show how this chiral Aubry-André model inherits its two-dimensional topology from a superspace model with an additional synthetic dimension, and use this concept to propose the engineering of complex topological insulators based on projecting topological properties of different dimensionalities down to physical space in spin systems and beyond.

- In **Chapter 5**, I will delve more deeply into a kind of substitutional disorder based on the removal or replacement of some percentage of magnetic atoms by non-magnetic ones. This is called dilution, and I will explore how it affects the band topology of 2D ferromagnetic spin systems. The focus will be the comparison of a simple Green's function approach based on the coherent-potential approximation (CPA), with a more complete numerical approach based on topological markers. I will show that the CPA predicts a topological phase transition compatible with that obtained by the more complete numerical treatment, and that key-features of the transition, such as the gapped or gapless nature of the spectrum when it occurs is found to be present in both the numerical simulation and the semi-analytical CPA approach. I will end this section with some remarks on a possible way to improve these results with a Feynman-diagrammatic approach to the CPA which will be explored more deeply in future work.

The richness of the physics of topological models I point to along this work, and the possibility of engineering these properties in diverse platforms such as spin systems is, in my personal opinion, one of the most interesting prospects of the modern conception of condensed matter physics. The fact that new properties of even the simplest non-interacting models in both fronts are today being discovered and put to work in

a technological context only goes to show that topological matter as well as spin systems still hold a huge amount of untapped potential. It is the objective of this thesis to draw from this potential and apply it to the cutting edge field of low-dimensional topological spin systems.

1.2 Introduction to spin systems

1.2.1 Quantum spin systems and the Heisenberg model

Magnetism in solids arises as a collective behavior of spin degrees of freedom of materials, and lattice quantum spin systems often provide a theoretical description of magnetic materials in the solid state [30]. Magnets have properties familiar to most people, generating magnetic fields responsible for an attractive force to other metallic objects. The origin of such magnetic fields lies in the fact that these magnetic solids can themselves be though of as small magnets with a magnetic moment. The word "spin" in spin systems refers to this magnetic moment, which can take into account different underlying microscopic phenomena depending on the nature of each magnetic material. One of the main reasons for the beauty and usefulness of spin systems is that one can often forget these underlying complexities, and treat each individual atom as a location for a quantum spin, with a total integer or half-integer value S. Generically, this spin S originates from the magnetic ground state of a multi-electron atoms. For spin systems with $S = 1/2$, the magnetic moment comes entirely from a single valence electron's actual spin, as derived from the Dirac theory of the electron. Higher values of S, on the other hand, can also occur, according to Hund's rules. Due to the intra-atomic exchange interactions, it may be energetically favorable, for the case of certain atoms, to populate different energy levels with electrons with aligned spins, instead of always pairing up electrons with opposite spins at the lowest available energy level. The total spin S is therefore simply a sum of the spin contribution of the individual electrons. In either case, the atomic spins in a crystalline lattice can interact with each-other via the inter-atomic exchange effect in case distances between atoms are small enough for electron orbitals to overlap in real space. In this case, it is the fermionic statistics of electrons which are responsible for their interaction, leading to a class of exchange-type magnets. On the other hand, for situations where magnetic nanoparticles or composites play the role of "atoms" in a lattice, effects such as the dipole-dipole interaction can become dominant, leading to a different class of magnetic models. In this latter class, the electron's angular momentum can also have a role to play in the value of S.

I will focus on the exchange–type magnets in this work, but more often than not the distinction is dropped under the guise of "spin systems". The exchange, dipole-dipole, as well as other types of inter-

actions can have different effects depending on the structure and properties of a given host material. In fact, they can favor the alignment, anti-alignment, or more complex behaviors, such as canting or twisting of spins. The aligned ordering of spins produces ferromagnets, and the magnetic moment generated by their alignment is responsible for the aforementioned fields which attract metals to conventional magnets. On the other hand, anti-ferromagnetic materials exhibit different ground state properties, with anti-aligned spins. Both of these behaviors form the basis for other, more exotic magnetic orders. They can be neatly summarized, by assuming a simple form for the interaction between two spins, often derivable in practice. One of the simplest interactions which captures ferromagnetism and anti-ferromagnetism can fairly generically be written as

$$H_{\text{2-Spin}} = -J_x S_1^x S_2^x - J_y S_1^y S_2^y - J_z S_1^z S_2^z, \tag{1.1}$$

called the Heisenberg interaction. Here $S_i^{x,y,z}$ represent the so-called spin operators (see Appendix A to which I relegate a description of spin operators and some of their useful properties). $J_{x,y,z}$ are called the exchange integrals between individual atomic spins, and are determined by the underlying inter-atomic exchange interaction. In terms of the spin operator representation, the value of S, called the total atomic spin, is determined by the eigenvalue of $S_i^2 = (S_i^x)^2 + (S_i^y)^2 + (S_i^z)^2$, which is $S(S+1)$. Another relevant quantum number is the eigenvalue of S_i^z, measuring the spin projection along the z axis, often labeled by m. Indeed, the quantum state of an individual atomic spin is defined by these two quantum numbers, and written as $|S, m\rangle$, or simply $|m\rangle$ if S is understood to be fixed. The spin operators act on the Hilbert space generated by such states, and thus encode information about the microscopic parameters of each spin. The exchange integrals, on the other hand, determine the most important macroscopic properties of magnets, such as the Curie temperature, or the response to external fields. In experiments, the exchange integrals are determined by fitting inelastic neutron scattering data to the Heisenberg interaction [31].

From such a simple form of the interaction, rich behavior already emerges: If, for example J_z dominates over the remaining energies and is positive, then the smallest energy $E = \sum_i \langle S, m_i | H_{\text{2-Spin}} | S, m_i \rangle$ is achieved if the spins attain maximum value and are aligned in the z direction with $m_i = S$. On the other hand, if J_z is negative, then the smallest energy is achieved if the spin projection along z attains a maximum value but the spins are aligned in opposing directions $m_1 = S$ and $m_2 = -S$ or vice-versa.

If all values of $J_{x,y,z}$ are the same, the ground state must incur a spontaneous symmetry breaking of the rotational $O(3)$ symmetry of the Hamiltonian, as the spins become aligned (or anti-aligned) in a particular direction picked out from the sphere, often identified with the z axis. In practice, this direction is randomly dictated by fluctuations in experimental realizations of the spin model, but for this to be

recovered naturally by theory, one often includes in spin models what is called an easy axis anisotropy term $H_{\text{EA}} = -K\left(S_i^z\right)^2$, breaking the symmetry of the model and favoring alignment along z. With this in mind, Heisenberg-type interactions are capable of explaining both ferromagnetic (FM) and anti-ferromagnetic (AFM) behavior. In the form written above the interaction between spins is fully anisotropic, but one often particularizes to the case of isotropic interactions. If a series of spin-S atoms are put on the lattice, and if isotropy is assumed, then a generic Heisenberg Spin Model (HSM) Hamiltonian reads

$$H_{\text{HSM}} = -\sum_{i,j} J_{ij} \boldsymbol{S}_i \cdot \boldsymbol{S}_j, \tag{1.2}$$

Where i and j index lattice sites, and where the bold symbol $\boldsymbol{S}_i$ represent the spin-vector operators (S_i^x, S_i^y, S_i^z) at site i. If the full isotropy of the Heisenberg model is broken several different models with quantitatively different physical properties emerge. For instance, if $J_z = 0$ one finds a so-called XY model, and if both J_x and J_y vanish, while J_z remains finite then an Ising model is present. Another possibility is that $J_x = J_y \neq J_z$ are all finite, in which case the model is said to be an XXZ model.

Due to its generality and descriptive power, the HSM is the central object of this thesis, providing the basis for most of the discussion of magnetic materials which will follow. Additional interactions between atomic spins with diverse physical effects can emerge either naturally or synthetically. These include spin-orbit-coupling terms, such as the Dzyaloshinskii-Moriya interaction (described in Chapter 2) as well as the Zeeman term, stemming from coupling of spins to an external magnetic field. Competition between such effects and the exchange interaction results in a very diverse landscape for the theory of magnetism in all dimensions.

1.2.2 Magnons and the Holstein-Primakoff representation

I mentioned in the previous section that the ground state of the isotropic HSM spontaneously breaks the $O(3)$ symmetry of the model, both in the case of FM and AFM systems. This spontaneous symmetry breaking has important consequences due to the famous theorem of Nambu and Goldstone [32, 33]. This result establishes that when a ground state breaks a continuous symmetry of its parent Hamiltonian, a gapless excitation accompanies the broken symmetry. The symmetry breaking of $O(3)$ symmetry in the FM ground state of the HSM induces the presence of low-energy spin-waves. These were first proposed by Felix Bloch in 1930 [34] to account for the temperature dependence of magnetization . The quantization of these spin-waves results in quasiparticles which are called magnons. These correspond to collective wave-like disturbances in the projection of the atoms' spin along the easy axis z. This can be visually understood in terms of the semi-classical spin-vector representation (see Fig. 1).

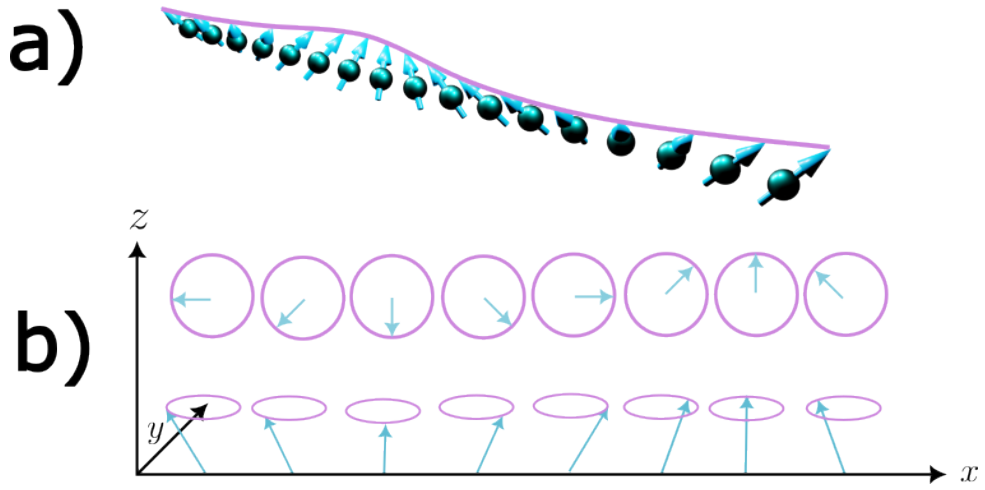

Figure 1: (a) Artistic rendering of a spin-wave. (b) Schematic representation using a semi-classical spin vector representation.

In this section, I provide a brief description of the theory of magnons, by starting from the algebra of spin operators, and showcasing how these can be represented in terms of bosonic operators. This procedure is called the Holstein-Primakoff (HP) bosonization [35].

The first step in understanding the theory of magnons is writing spin model Hamiltonians in a convenient form. Often, it is useful to represent these models not in term of the $S_i^{x,y,z}$ operators, but rather in terms of S_i^z and $S_i^{\pm} = S_i^x \pm iS_i^z$. It is simple to show that these operators act by lowering (-) or raising (+) the spin projection along z by one integer (see Appendix A). A HSM, for instance, can be represented as

$$H_{\text{HSM}} = -\sum_{i,j} J_{ij} \left[\frac{1}{2} \left(S_i^+ S_j^- + S_j^+ S_i^- \right) + S_i^z S_j^z \right]. \tag{1.3}$$

The fact that the work presented in this thesis is restricted to a ferromagnetic ground state $|\text{FM}\rangle$ is crucial for the discussion here, and even though spin-wave theory can be extended via generalized Bogoliubov transformations to AFM ground states [36, 37, 38, 39, 40], I shall describe only the ferromagnetic case. In such a state the spin projection is uniformly $\langle S_i^z \rangle = m_i = S$, that is, all spins are aligned along z. This allows us consider the effect of lowering, for a single site, the projection along the z axis of the spin by one unit by acting with $S_i^- |\text{FM}\rangle$. This results in a quantized excitation above the ground state. A spin-wave with momentum $\boldsymbol{k}$ can then be thought of as a state $|\boldsymbol{k}\rangle = \sum_i e^{-i\boldsymbol{k}\cdot\boldsymbol{R}_i} S_i^- |\text{FM}\rangle$. Several notes about spin operators and this ferromagnetic ground state are included in Appendix A in order to complement this discussion. For now, it is intuitive that $S_i^- |\text{FM}\rangle$ should act as a quasi-particle, and indeed, the formal

procedure for the quantization of spin-waves proceeds by noting that the algebra of the $S_i^{\pm}$ operators is very similar, to the canonical bosonic commutation relations. In particular, it is simple to show that $\left[S_j^-, S_i^+\right] = 2\hbar S^z \delta_{ij}$. To construct bosonic creation and annihilation operators $a_i^\dagger$ and a_i from $S_i^{\pm}$, one performs the so-called Holstein-Primakoff transformation

$$S_i^z = S - a_i^\dagger a_i, \tag{1.4}$$

$$S_i^+ = \sqrt{2S}\sqrt{1 - \frac{a_i^\dagger a_i}{2S}}a_i, \tag{1.5}$$

$$S_i^- = \sqrt{2S}a_i^\dagger\sqrt{1 - \frac{a_i^\dagger a_i}{2S}}. \tag{1.6}$$

In the HP boson picture, the projection along z of an atomic spin is found by subtracting from S the number of bosons occupying the atom's site, i.e. $S - \left\langle a_i^\dagger a_i \right\rangle = m_i$. The somewhat more complicated form of the $S_i^{\pm}$ operators simply ensures that the canonical commutation relations $\left[a_i^\dagger, a_j\right] = \delta_{ij}$ hold. This exact transformation, however, is cumbersome due to the presence of a formal square root of creation and annihilation operators. For this reason, in all the remainder of the thesis, I will work always within the linear HP boson limit. In this regime, the formal square root present in equations (1.5) and (1.6) is expanded, and only up to quadratic terms in HP operators are kept in any expression involving such operators. The expansion of the square root requires a low-density regime of HP bosons, i.e. that the number of HP bosons is on average much smaller than S. This also ensures that interactions between these bosons can be neglected. In this regime, the linear HP boson transformations read

$$S_i^z = S - a_i^\dagger a_i, \tag{1.7}$$

$$S_i^+ \approx \sqrt{2S}a_i, \tag{1.8}$$

$$S_i^- \approx \sqrt{2S}a_i^\dagger \tag{1.9}$$

Performing a Fourier transformation of the HP boson operators leads to creation and annihilation operators in reciprocal space, indexed by a momentum $\boldsymbol{k}$.

$$a_{\boldsymbol{k}} = \sum_i e^{i\boldsymbol{k}\cdot\boldsymbol{R}_i}a_i, \tag{1.10}$$

$$a_{\boldsymbol{k}}^\dagger = \sum_i e^{-i\boldsymbol{k}\cdot\boldsymbol{R}_i}a_i^\dagger. \tag{1.11}$$

In the linear spin-wave approximation, when acting on the ground state $|\mathrm{FM}\rangle$ with $a_{\boldsymbol{k}}^\dagger$, it is clear that one can exactly reproduce the spin-wave states $|\boldsymbol{k}\rangle$, and thus, the effect of the HP bosonic operators is to

create or destroy magnons, the quantized version of spin-waves. The description of the HSM in terms of spin-waves makes clear an analogy between crystallographic and magnetic order, where the exchange integrals play the role of "bonds" or "hoppings" between the atomic sites, and spin-waves propagate from site to site with a certain momentum. This is a crucial analogy when discussing any topological magnon model, since more often then not, these realize already understood and well characterized TBMs. Unlike chemical bonds, however, it is worth noting that while electronic bonds between atoms are fairly common and importantly are responsible for all of chemistry, the exchange interaction is much rarer, occurring only for a small amount of crystalline structures made up of elements in the 3d, 4f, 4d and 5d blocks of the periodic table [41].

1.2.3 The case of two-dimensional magnets

When discussing magnetism, one must be extra careful in the case of low-dimensional systems, since additional features come into play. Namely, a long-established result, called the Mermin-Wagner theorem [42, 43], prevents long-range magnetic order in dimensions two or lower, as a result of divergent spin-wave dynamics caused by thermal fluctuations. This result holds for both FM and AFM order, and seemingly prevents the existence of magnetism in 1D and 2D for any finite temperature $T > 0$, as stemming from isotropic Heisenberg models. Thus, from a theoretical perspective it was historically never clear that such systems can exist in the first place. The Mermin-Wagner theorem was established some decades after some of the most celebrated works in magnetism by physicists and mathematicians alike, among which perhaps the most seminal work in the field of 2D magnetism, namely, the analytical solution of the 2D Ising model by Onsager [44]. For this reason, magnetism in 2D faced some challenges in part caused by the fact that a fairly critical loophole in this theorem was not appreciated at first, which turns out to be key in allowing magnetism in 2D.

This loophole consists of the fact that the Mermin-Wagner theorem applies only in the case of fully isotropic Heisenberg models. It does not apply to Ising, XY, XXZ models, and the presence of anisotropy, whether induced by a physical easy-axis anisotropy term, a skewed exchange integral with $J_z > J_{x,y}$ or any other physical effect in a HSM also enables the possibility of magnetism in two dimensions. It was only in 2016/2017, that the isolation of several one atom thick van der Waals (vdW) magnetic materials (more than a decade after the discovery of graphene in 2004) generated a paradigm shift in magnetism research. This is despite the fact that there already existed examples of effectively 2D magnets: In the 1960s quasi-2D magnets in bulk crystals were first discovered [45, 46], and through the 70s, 80s, and 90s, the development of thin-film growth technologies also resulted in atomic thickness thin film magnets

[47], enabling the experimental verification of several seminal theoretical works, including Onsager's.

Thus, even though the field 2D magnetism is not particularly new, it was in the setting of vdW materials that the field found exponential growth. In this novel context, the dipolar interaction also plays a crucial role in the breaking of the conditions for the Mermin-Wagner theorem, and even though the magnetocrystalline anisotropy and dipolar interactions do not dominate the physical description of experimentally observed 2D vdW magnets, being only of the order of 1meV, this energy scale is enough to ensure stability of magnetism in two dimensions. Today, in the realm of vdW 2D magnets, several examples have been experimentally verified, including $FePS_3$ [48, 49], $MnSe_2$[50], Fe_3GeTe_2[51, 52], $CrGe_2Te_6$[53] and CrI_3 [54].

The search for intrinsic magnetic order in 2D vdW materials lead first to the discovery of an AFM Ising phase in $FePS_3$ in 2016, showcasing for the first time that 2D vdW magnetic materials were possible. The desire to produce FM ordered 2D vdW materials later resulted in the study of $CrGe_2Te_6$ and CrI_3 monolayers, which are indeed FM-ordered. Interestingly, CrI_3 bilayers are non-magnetic, and hence it is understood that stacked layers of this material align their spins in opposite directions, in a balancing act which results in a non-ferromagnetic vdW structure [52]. Moreover, CrI_3 has a honeycomb structure with a robust magnetic order, which has, since its discovery been implemented in functionalized devices. Some works also propose that its magnetic properties are sensitive to electric fields, and that different kinds of magnetic interactions leading to topological properties are predicted to exist in the model [55], which are all very relevant for the discussions presented throughout the thesis.

Besides these strongly intrinsic ferromagnets, its also worth noting that materials such as graphene can be made magnetic by a series of different methods, some of which are also relevant for the work presented here. For instance, it has been pointed out that graphene can be turned into a 2D magnetic material via introducing point defects [56], via straining [57] and via hydrogenation [58].

Of course, several difficulties exist in handling, producing and manipulating 2D magnets. Most notably, both CrI_3 and $CrGe_2Te_6$ have a very low phase transition temperatures at $T_c < 40$K and $T_c < 45$K respectively. Additionally, materials such as Fe_3GeTe_2 have higher transition temperatures but weaker forms of magnetism. Thus, even though several notable progresses have been achieved, such as all-electrical control of magnetism in CrI_3 [54], spin-charge [59] and spin-torque [49] conversion in graphene or MoS_2 based heterostructures, critical for implementations such as magnonic processors, transistors, and spin-torque junctions, it is still the case that strongly intrinsic and stable 2D ferromagnets with high transition temperatures are desired for increasing the versatility of devices.

One of the possible routes for increasing the viability and stability of magnonic and spintronic devices using vdW 2D magnets is the presence of topological features in these magnets, and this will be the main

content of the thesis.

1.3 Introduction to topology

1.3.1 Geometric phases in electromagnetism and condensed matter

At the heart of band topology is the concept of geometric phases, which are intimately related to the differential geometric concept of holonomy. Holonomy is a familiar notion to many physicists, for which intuition can easily be gained: Consider the case of a vector placed at the north pole of the earth, and pointing in a direction which is tangent to the earth's crust. If one translates the vector to the equator along a meridian, then along the equator for some distance, and back to the north pole, the vector's orientation will have changed relative to how it started by some angle. This angle is called the holonomy. The origin of non-trivial band topological properties is not so different from this example, with the crucial replacement of the vector by a Hamiltonian $H(\boldsymbol{R})$ with a set of bands, which depends on a set of parameters $\boldsymbol{R} = (R_1, \ldots, R_m)$. The earth then corresponds to the manifold spanned by these parameters. In the context of Hamiltonians, holonomy manifests as the acquisition of additional geometric phases by the eigenstate of $H(\boldsymbol{R})$ as the parameter space manifold is traversed.

The idea is that if the parameters $\boldsymbol{R}$ are varied adiabatically, then at each subsequent value of $\boldsymbol{R}$, eigenstates of one set of parameters are smoothly deformed into another set. This is the content of the adiabatic theorem, which states that in the case of adiabatic evolution of the parameters along a curve $\boldsymbol{R}(t)$, the Schrodinger equation

$$-i\hbar\frac{\partial}{\partial t}\left|\psi_n(\boldsymbol{R}(t))\right\rangle = \varepsilon_n(\boldsymbol{R}(t))\left|\psi_n(\boldsymbol{R}(t))\right\rangle, \tag{1.12}$$

is obeyed instantaneously. Here $|\psi_n(\boldsymbol{R}(t))\rangle$ represents the eigenstate of the Hamiltonian in the nth band, with energy $\varepsilon_n(\boldsymbol{R}(t))$. Now, generically, due to the structure of the Schrodinger equation, and the normalization of states, a single degree of freedom exists, which can change the eigenstate as it is moved along the curve $\boldsymbol{R}(t)$. This corresponds to a phase denoted by $\theta(t)$, such that the state can be decomposed as $|\psi(\boldsymbol{R}(t))\rangle = e^{i\theta(t)/\hbar}\left|\phi(\boldsymbol{R}(t))\right\rangle$. A short calculation performed by plugging this form of the state into the Schrodinger equation on both sides, and acting with $\langle\psi_n(\boldsymbol{R}(t))|$ on the left is enough to solve for the phase $\theta(t)$.

$$\theta(t) = \int_0^t dt' \left[\varepsilon(\boldsymbol{R}(t')) + \frac{i}{\hbar}\left\langle\phi(\boldsymbol{R}(t'))\right|\frac{\partial}{\partial t'}\left|\phi(\boldsymbol{R}(t'))\right\rangle\right]. \tag{1.13}$$

There are two contributions to the phase acquired by the eigenstate under adiabatic evolution. The first is the dynamical phase $\theta_D(t) = i/\hbar \int_0^t dt' \varepsilon(\boldsymbol{R}(t'))$, familiar from the usual quantum mechanical theory, which is acquired from evolving in time in the Hilbert space. However, a second term appears, which is called the geometrical phase or Berry phase [60, 61]. This phase can be calculated via the aforementioned time integral, or equivalently by integrating over the curve C spanned in the parameter space manifold during the adiabatic evolution

$$\gamma_C = \int_C d\boldsymbol{R} \cdot \frac{i}{\hbar} \langle \phi(\boldsymbol{R}) | \nabla_{\boldsymbol{R}} | \phi(\boldsymbol{R}) \rangle \, . \tag{1.14}$$

Mathematically, several notions are at play here. By associating the space of possible phases $U(1)$ to each point in the parameter space manifold, one actually constructs a mathematical object called a principal-$U(1)$ fiber bundle, where a copy of the group $U(1)$ is associated to each point $\boldsymbol{R}$ of the manifold [62]. The Schrodinger equation provides a way to relate different fibers (copies of $U(1)$), and induces what is called a connection on the fiber bundle . In this context, this is called the Berry connection, and simply corresponds to the integrand appearing in the geometric phase $A(\boldsymbol{R}) = \frac{i}{\hbar} \langle \phi(\boldsymbol{R}) | \nabla_{\boldsymbol{R}} | \phi(\boldsymbol{R}) \rangle$. The Berry connection plays the same role in adiabatic evolution as the magnetic vector potential in electromagnetism, and indeed, much like in the latter theory, this connection can be used to construct a curvature tensor. In the context of electromagnetism, the curvature tensor is nothing but the electromagnetic tensor $F_{\mu\nu}$, while in the context of the adiabatic evolution of quantum systems, it is given the special name of Berry curvature. Explicitly, this Berry curvature reads

$$\Omega_{\mu\nu}(\boldsymbol{R}) = \frac{\partial}{\partial R^\mu} A_\nu(\boldsymbol{R}) - \frac{\partial}{\partial R^\nu} A_\mu(\boldsymbol{R}). \tag{1.15}$$

One often considers the dual pseudo-vector to this tensor, and calls that the Berry curvature instead. This latter quantity defined as the pseudo-vector $\boldsymbol{\Omega}^\xi(\boldsymbol{R})$ related to the Berry curvature tensor as $\Omega_{\mu\nu}(\boldsymbol{R}) = \varepsilon_{\mu\nu\xi} \boldsymbol{\Omega}^\xi(\boldsymbol{R})$, where $\varepsilon_{\mu\nu\xi}$ is the Levi-Civita completely anti-symmetric symbol and the Einstein summation convention is assumed. In the analogy with electromagnetism, this quantity is analogous to the magnetic field. Another similarity between electromagnetism and these concepts is that the Berry connection, like the magnetic vector potential, is defined only up to a gauge choice. This makes it so the Berry phase is only well defined if closed curves C in the parameter space are considered.

Let me introduce two examples from electromagnetism which will appear in later chapters of this thesis as a starting point to understanding the Berry phase, connection and curvature in more detail. The first is the Aharonov-Bohm (A-B) effect [63], and to understand it, consider an electron restricted to the xy-plane

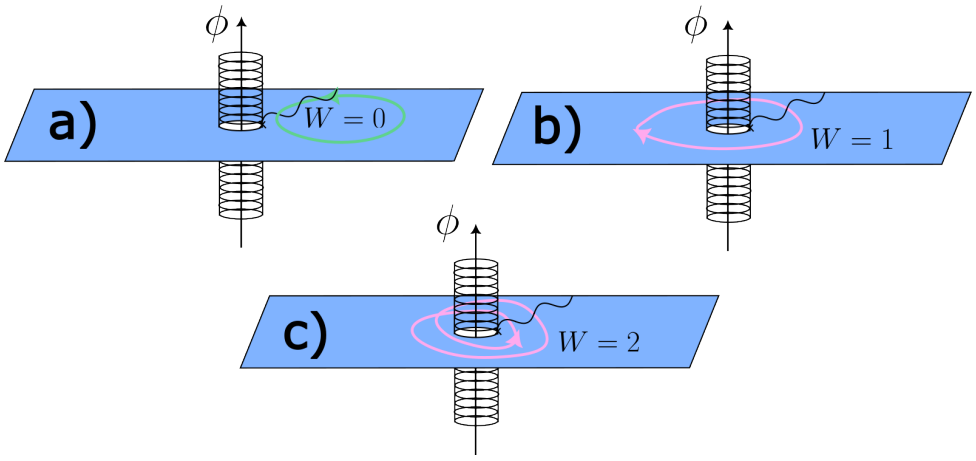

Figure 2: (a) Trajectory of an electron in to the xy-plane which does not wind around a solenoid pierced by a magnetic flux ϕ. No resulting A-B phase is observed. Even though it crosses the branch cut, it does so twice in opposite directions, resulting in a null A-B phase. (b) Trajectory of an electron with winding number $W = 1$, and which acquires an A-B phase of $e/\hbar$, by crossing the branch cut once. (c) Trajectory of an electron with winding number $W = 2$, and which acquires an A-B phase of $2e/\hbar$, crossing the branch cut twice in the same direction.

which is pierced by an infinitely thin and long solenoid, through which a magnetic field flows, generating a flux thread. Inside the solenoid, a magnetic field $\boldsymbol{B} = B\hat{\boldsymbol{z}}$ is present and induces a flux ϕ. Outside the solenoid, no field or flux exists. Nevertheless, a magnetic vector potential $\boldsymbol{A}$ permeates all space. Now, note that the electron wandering the plane will actually be affected by the vector potential, in that the Hamiltonian describing it will have the form $H = \left(\hat{p} - e\hat{\boldsymbol{p}} \cdot \boldsymbol{A}(\boldsymbol{R})\right)^2 / 2m$, where $\hat{\boldsymbol{p}}$ is the momentum operator, e is the electron charge and m its mass. In this case, the parameters $\boldsymbol{R}$ can be identified with the actual position of the electron in the xy plane. Since the electron cannot enter the solenoid, which is assumed to be placed at $\boldsymbol{R} = 0$, its movement is restricted to $\boldsymbol{R} \in \mathbb{R}^2 \backslash 0$. Furthermore, by moving the electron along a curve C it will acquire a Berry phase

$$\gamma^{AB} = \frac{e}{\hbar} \oint d\boldsymbol{R} \cdot \boldsymbol{A}(\boldsymbol{R}), \tag{1.16}$$

which is in this context called the A-B phase. The A-B phase, in some sense, measures the inability of making a continuous gauge choice for the magnetic vector potential in a punctured plane. The presence of the hole makes it so a discontinuity along a branch cut is a mathematical necessity, and as a result, if an electron loops around the hole, it will acquire a non-trivial phase, dependent only on the number of times it goes around the hole (see Fig. 2). For this reason, it is said that the A-B phase is a topological quantity, depending only on the topology of the electron's trajectory, namely on a quantity called the "winding number". Alternatively, through the usage of Stoke's theorem, it is simple enough to compute the A-B

phase as being proportional to the magnetic flux $\gamma^{AB} = e/\hbar \int d\boldsymbol{S} \cdot \boldsymbol{B} = W\phi e/\hbar$ enclosed by the trajectory, where W counts the number of loops the electron makes around the solenoid. This quantity $W \in \mathbb{Z}$ corresponds precisely to the winding number.

Another topological phase which crops up in electromagnetism is the dual phenomena to the A-B effect, called the Aharonov-Casher (A-C) effect [64]. Here a neutral particle confined to the $xy-$plane carries some magnetic moment $\boldsymbol{\mu}$ and is subject to an external magnetic field $\boldsymbol{E}(\boldsymbol{R})$ caused by a line of charges piercing the plane. The magnetic vector potential $\boldsymbol{A} = \boldsymbol{\mu} \times \boldsymbol{E}/\hbar c^2$ can be defined, and it is clear that the role of electric and magnetic fields is switched. The resulting Berry phase is

$$\gamma^{AC} = \frac{1}{\hbar c^2} \oint d\boldsymbol{R} \cdot \boldsymbol{\mu} \times \boldsymbol{E}(\boldsymbol{R}). \tag{1.17}$$

Finally, as opposed to the example of electromagnetism, band topology becomes relevant when, for a TBM in some $d-$dimensional lattice (in this thesis $d = 1, 2$), the parameter space manifold is simply the Brillouin zone possibly augmented by tunable parameters of the model [65, 66]. Thus $\boldsymbol{R}$ is taken to be the momenta $\boldsymbol{k} = (k_1, \ldots, k_d)$, together with a set of additional parameters such as the (relative) strengths of TBM hoppings. In this context, the restriction that evolution is adiabatic simply means that the system must remain in a situation where energy bands do not cross, i.e. the system must be gapped. The Hamiltonian $H(\boldsymbol{k})$: BZ $\rightarrow T$ is interpreted as a mapping from the Brillouin Zone onto some target space T of possible gapped and Hermitian Hamiltonians. Depending on the symmetries of the Hamiltonian, the target space can have a variety of different topological characteristics. Here, by topological characteristics I mean something akin to the "number of holes" or the genus of a surface. Mathematically, these topological characteristics are encapsulated in the notion of the fundamental groups of the target spaces, but the analogy with the genus suffices for the purposes of this thesis. In the case of surfaces, the genus can be counted by integrating the surface's curvature, according to the Gauss-Bonnet theorem [67, 68, 69]. In the same manner, information about the topology of the target space of $H(\boldsymbol{k})$ can also be gained by integrating the Berry connection or curvature over the entire Brillouin zone, or in other words, the holonomy of the Hamiltonian as the Brillouin zone is traversed is sensitive to the band-topology. The integration of this Berry curvature yields quantities called topological invariants which are analogous to the genus or the Winding number of the A-B or A-C effects. In Chapter 2 these ideas are explored more deeply for two topological models I will use again and again throughout this thesis. The reason for being interested in topological properties of TBMs is dependent on the type of system one considers, but for the purposes treated in this thesis, one uses topological invariants to characterize phases hosting gapless edge states while remaining insulating in the bulk. This so-called bulk-boundary correspondence is the hallmark of

topological insulators, and I shall go into it more deeply in the next chapter.

Chapter 2

Topological models and their realization in Spin Systems

2.1 Topological models

2.1.1 The SSH model, the Winding number and Zak's phase

One of the simplest 1D models one can consider, in order to apply the ideas of band topology introduced in Chapter 1, and one which I will describe many times in different contexts along this thesis is the Su-Schrieffer-Heeger (SSH) [70, 65, 71] model. It is a 1D model of a diatomic chain where excitations (Fermions or Bosons) can hop between nearest neighbor atoms. Due to its simplicity is often used as a first introduction to band topology. The SSH model is composed of a bipartite lattice with two atom types per unit cell labeled by A and B, and staggered or alternating hopping strengths between these atoms: Within the same unit cell, excitations hop from the A to the B atom with probability amplitude t_1, whereas an excitation in a B atom in the ith unit cell can hop into an A atom in the $i+1$th cell with probability t_2. The SSH model is schematically illustrated in Fig. 3 (a).

Such a system is described in second quantization, by a Hamiltonian of the form

$$H = -\sum_i t_1 a_i^\dagger b_i + t_2 b_i^\dagger a_{i+1} + \text{h.c.}, \tag{2.1}$$

where $a_i^\dagger(a_i)$ create (annihilate) excitations in the A atom of unit cell i, and equivalently $b_i^\dagger(b_i)$ create (annihilate) excitations in the B atom of unit cell i. Due to the presence of translation symmetry (a luxury which will not always be present, along this thesis) one can consider Fourier transform the creation/annihilation operators, and treat the system in terms of its crystal momentum k, restricted to the first Brillouin zone (BZ). In 1D, this BZ is isomorphic to the circle S^1. If the vector $\Psi_k^\dagger = \left(a_k^\dagger, b_k^\dagger\right)$ is defined, the Hamiltonian operator can be written as a bilinear form

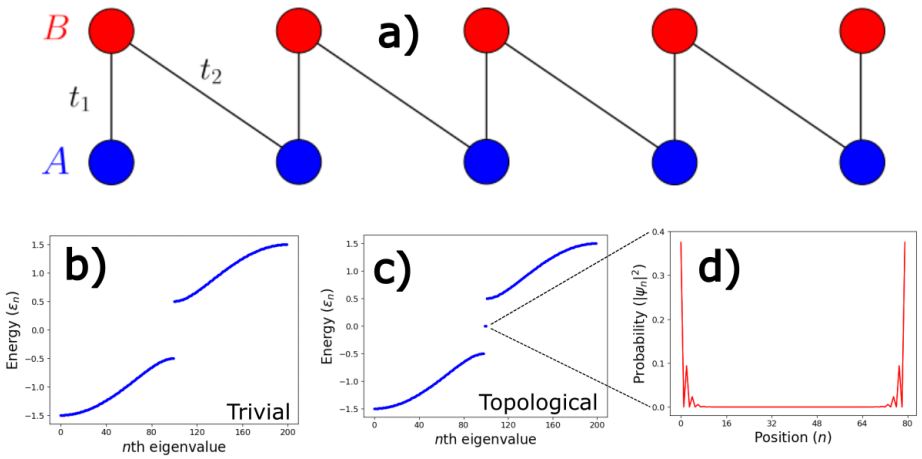

Figure 3: (a) Schematic representation of the SSH model. A-sublattice atoms are represented in blue, and B-sublattice atoms in red. The hoppings t_1 connect A and B atoms within the same unit cell (represented vertically), whereas t_2 hoppings connect B and A atoms in different unit cells. (b) Spectrum of an SSH model chain with 200 atoms in a trivial phase. (c) Spectrum of an SSH model chain with 200 atoms in a topological phase. (d) Topological zero-energy edge modes for an SSH chain with 80 atoms.

$$H = \sum_k \Psi_k^\dagger \begin{bmatrix} 0 & -t_1 - t_2 e^{ika} \\ -t_1 - t_2 e^{-ika} & 0 \end{bmatrix} \Psi_k. \tag{2.2}$$

This is a simple two-band model with Hamiltonian matrix corresponding to the 2×2 Hermitian matrix written explicitly in equation (2.2). The Hamiltonian matrix, $H(k)$, works as a map from the circle to a subset of the space of hermitian 2×2 matrices. The eigenstates of this matrix are dependent on a single momentum parameter: the crystal momentum k, and as such, these states are denoted by $|n, k\rangle$ where $n = 1, 2$ is a band index.

The spectrum of energy bands emerging from the Hamiltonian is fairly interesting, and two clearly distinct cases are illustrated in its eigen-energies in Figs. 3 (b) and (c). Namely, in panel (c) two degenerate modes appear with zero energy. The probability distributions of such states are located at the edges, and for this reason these are called zero-energy edge modes. The existence of these edge modes can be explained fairly intuitively. Let us consider a scenario where a finite chain of N unit cells is characterized by hopping strengths $|t_1| > |t_2|$. In this case, intra-cell hoppings are favored and the chain starts with the strongest bond, which means that excitations present at the edge can propagate towards the bulk. On the other hand, if $|t_1| < |t_2|$, what is favored energetically instead, is that excitations present at the edge of the chains remain there, leading to localized modes. This can be explained succinctly in terms of an analysis based on topology.

To perform this analysis, a nice way to write this Hamiltonian matrix is at the cost of the Pauli matrices: One can define a 3-vector $\boldsymbol{h}(k) = (-t_1 - t_2\cos(ka), -t_2\sin(ka), 0)$, such that the Hamiltonian matrix is written as $H(k) = \boldsymbol{h}(k)\cdot\boldsymbol{\sigma}$,where $\boldsymbol{\sigma} = (\sigma_x, \sigma_y, \sigma_z)$ is the vector containing the x, y and z Pauli matrices. At this point, one can begin to note several things about the target space of $H(k)$. In particular, the fact that this model holds a special kind of symmetry called chiral symmetry restricts the space greatly. A system is said to be chirally symmetric if there exists an operator Γ, with $\Gamma^2 = \mathbb{1}$ such that conjugating the Hamiltonian matrix reverses its sign, i.e. $\Gamma H(k)\Gamma^\dagger = -H(k)$. If a certain system is chirally symmetric, the operator Γ is said to realize the chiral symmetry. It can easily be checked that the operator which realizes the chiral symmetry in the case of the SSH model is the σ_z Pauli matrix. Together with the chiral symmetry, the SSH model also exhibits time-reversal $TH^*(k)T^\dagger = H(-k)$ and charge conjugation or particle-hole $CH^*(k)C^\dagger = -H(-k)$ symmetries, with $T = \sigma_x$ and $C = \sigma_y$. This behavior puts the SSH model in the so-called BDI class of the Altland-Zirnbauer classification [72, 66].

One then can also explore in which ways the Hamiltonian can be deformed without breaking the chiral symmetry. It turns out that adding terms proportional to σ_x or σ_y does nothing to change this symmetry, but if a term which is proportional to σ_z is added, then chiral symmetry is broken. This restricts the $\boldsymbol{h}(k)$ vector to live in the xy plane. Furthermore, as previously stated, the adiabatic condition implies that the Hamiltonians can be deformed at will with the exception of closing the band-gap which separates a set of upper bands, from a set of lower bands. Since the SSH model is a two-band model, the situation where the bands touch is excluded, corresponding to the $\boldsymbol{h}(k) = (0,0,0)$ point. Hence, what is left is a situation where the $\boldsymbol{h}(k)$ vector can live in a space isomorphic to two-dimensional vectors except for the zero vector $\mathbb{R}^2\backslash 0$, or, equivalently, to complex numbers without zero $\mathbb{C}\backslash 0$. This latter case works by defining an equivalent mapping $h(k) = h_x + ih_y = -t_1 - t_2 e^{-ika}$. In general, this is precisely the case described in the context of the A-B effect. The topology of the model should, therefore, be characterized by the amount $\boldsymbol{h}(k)$ vector winds around this hole. To see that this winding number can be extracted from the Hamiltonian, start by noting that the pair of hopping strengths can be thought of as a two-dimensional vector $(t_1, t_2) \in \mathbb{R}^2$. Hence, the parameter space for the Hamiltonian matrix is $S^1 \times \mathbb{R}^2$. The $\boldsymbol{h}(k)$ vector works as a mapping $\boldsymbol{h} : S^1 \times \mathbb{R}^2 \to \mathbb{C}\backslash 0$, and thus one can use the tools of complex analysis to compute the winding number as [73]

$$W = \frac{1}{2\pi i}\int_0^{2\pi} dk \frac{d\log(h)}{dk} \in \mathbb{Z}. \tag{2.3}$$

Given an SSH type model, or indeed any chirally symmetric 2×2 Hermitian Hamiltonian matrix, the corresponding Winding number can computed. It might be zero corresponding to a topologically trivial

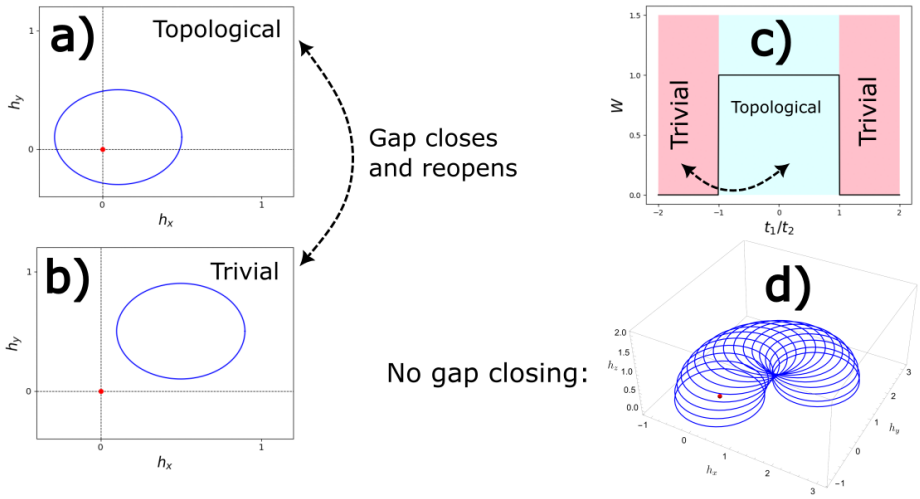

Figure 4: (a) Image of the Dirac vector $\boldsymbol{h}(k)$ in the presence of chiral symmetry, with a winding number $W = 1$. (b) Similar plot to (a) in a topologically trivial phase, with $W = 0$. (c) Calculation of the Winding number as a function of t_1 and t_2. (d) Going from a situation with a winding number $W = 1$ to $W = 0$ without closing the gap. This is possible by extending the target space of $\boldsymbol{h}(k)$ by breaking chiral symmetry and including a σ_z term in the Dirac Hamiltonian.

phase, or a non-zero integer if the phase is topological. Considering the free parameters of the SSH $(t_1, t_2) \in \mathbb{R}^2$, one can easily find that $W = 1$ if $|t_1| < |t_2|$, since the image of the circle under the h-map $h(S^1)$ contains the origin. On the other hand, if $|t_1| > |t_2|$ then $W = 0$. Note that these situations are topologically distinct, since to get from one to the other continuously, at least one point in the image of $h(S^1)$ would have to pass through the origin, which is not in the space $\mathbb{C}\backslash 0$. Passing through this point implies closing the gap.

Finally, comparing the regimes of present and absent edge states and the value of W, it becomes clear that W signals precisely the presence of edge states in the system. If $W = 1$ two zero energy edge modes are present and the system is said to be in a topological insulating phase. If $W = 0$ no edge modes are present, and the system is in a trivial phase. This is a very clear example of the bulk-boundary correspondence of topological insulators.

The phases with $W = 0, 1$ for the SSH model are illustrated in Fig. 4. Note that the presence of chiral symmetry is essential here. In particular, if chiral symmetry were not present, the $\boldsymbol{h}(k)$ vector, would be a map $\boldsymbol{h} : S^1 \to \mathbb{R}^3\backslash 0$. The additional freedom to manipulate $\boldsymbol{h}(k)$ in 3D space would mean that one could deform the Hamiltonian into the h_z direction, moving between the two situations illustrated in Fig. 4 (a) and (b) without ever going through the origin. This is depicted in Fig. 4 (d). Note that the two possibilities of $W = 0, 1$ are the only two distinct topological phases accessible to the SSH

model. These are not the only accessible phases possible in general, for chiral symmetric systems in 1D, since the Winding number is a $\mathbb{Z}$-invariant, and it has in fact been shown that the inclusion of bonds over more distant neighbors allows for transitions to phases with different winding numbers [74]. The picture painted so far is the quintessential marking of band topology where the presence of a symmetry allows for topological properties to manifest, and smooth deformations of the Hamiltonian matrix achieved by moving in the parameter space preserve the values of certain topological invariants. The topological invariant which is relevant in the case of the SSH model is, of course, the winding number. To see how this picture connects to the picture of the Berry phase, discussed in Chapter 1, one merely has to compute the Berry connection in the parameter space corresponding to the first Brillouin zone, which is isomorphic to S^1. For the nth band

$$A_n(k) = \frac{i}{\hbar} \langle n, k | \, \partial_k \, | n, k \rangle = -\frac{1}{2} \frac{\partial \log(h)}{\partial k}. \tag{2.4}$$

This explicit computation makes use of the eigenvectors of the Hamiltonian matrix, given by $|n, k\rangle = \left(e^{i\phi(k)}, 1\right)^\dagger / \sqrt{2}$, with $\phi(k) = \log(h)$, or in terms of t_1 and t_2

$$|n, k\rangle = \begin{pmatrix} \frac{|t_1 + t_2 e^{-ika}|}{t_1 + t_2 e^{-ika}} \\ 1 \end{pmatrix}. \tag{2.5}$$

The second equality of equation (2.4) shows that the integrand in equation (2.3) is recovered. Thus, an integration of $A_n(k)$ over the Brillouin zone yields πW. Note that in 1D systems, since the Brillouin zone is S^1, the only gauge invariant Berry's phase which can be defined amounts to going around the circle an integer number of times and returning to the starting point. This means that the Brillouin zone must be traversed an integer number of times, hence the quantization of the winding number. The phase πW in the context of 1D models is often called Zak's phase, and although the true definition of Zak's phase is a bit more subtle [62, 75], this is enough for the purposes of this thesis.

2.1.2 The Haldane model and the Chern number

Like the SSH model, the Haldane model is a topological band insulator, but it exists in 2D. It is often prototypical model for so-called anomalous hall insulators, and the most common example of a system exhibiting an integer topological invariant called the (first) Chern number. This section serves as a swift introduction to the structure of honeycomb lattices, and the Haldane model, which will be of central importance in Chapters 3 and 5. Being such a prototypical topological insulator, the Haldane model is also covered in many introductory texts [71, 65, 76]. As I mentioned in the motivation section for this work, the first discovery of topological matter occurred in the form of the IQHE [77]. This effect arises

when a metallic material in 2D is subject to an external magnetic field, and results quantized plateaus of conductivity visible when a metal is subject to a magnetic field. The conductivity plateaus are indexed by the Chern number, a connection to topology which was established by Thouless, Kohmoto, Nightingale and den-Nijs [1], who used linear response theory and arrived at the Chern number using considerations seemingly unrelated to the ones I have described here. As was first discovered by Haldane, however, it is possible to develop a TBM hosting a Chern number without an applied magnetic field [5]. The key ingredient, is that a topological invariant can exist in a 2D insulating material only if time-reversal symmetry is broken. Haldane's model exists in the form of a honeycomb lattice, much like the first, and most celebrated 2D material: graphene. The structure of the honeycomb lattice is illustrated in panel (b) of Fig. 5.

The hexagonal lattice is a Bravais lattice with two atoms per unit cell and thus can be thought of as being composed of two distinct triangular sublattices, which are labeled by A and B. An $A-$sublattice atom is connected to its nearest neighbors (NN) via the vectors

$$\boldsymbol{\delta}_1 = (\sqrt{3}/2, -1/2)a, \tag{2.6}$$

$$\boldsymbol{\delta}_2 = (0, 1)a, \tag{2.7}$$

$$\boldsymbol{\delta}_3 = (-\sqrt{3}/2, -1/2)a, \tag{2.8}$$

where a is the inter-atomic distance. Next-nearest neighbor (NNN) vectors are $\boldsymbol{a}_1 = \boldsymbol{\delta}_1 - \boldsymbol{\delta}_2$ and $\boldsymbol{a}_2 = \boldsymbol{\delta}_2 - \boldsymbol{\delta}_3$. For the $B-$sublattice, the NN vectors are simply the negative of these. Note that at the level of NN hoppings, all bonds occur from $A-$sublattice sites to $B-$sublattice sites and vice-versa. This can be understood as a practical definition of chiral symmetry (sometimes also called sublattice symmetry). For this reason, together with the presence of inversion symmetry, it is a well know fact that TBMs with hoppings along NN bonds in the honeycomb lattice hosts a pair of gapless points in the Brillouin zone called Dirac points. Near these points, the electronic dispersion is linear, and the low-energy excitations of the system are massless quasiparticles, called Dirac Fermions. These excitations have been realized in 2D materials including, most famously, graphene [78]. The theoretical description and experimental observation of Dirac Fermions sparked a revolution in its own right, resulting in a surge of interest in low-dimensional materials and heterostructures as platforms which allow for a tabletop realization of ultra-relativistic phenomena [79]. However, as previously mentioned, topologically non-trivial properties necessitate gapped phases, and thus, a reduction of the model's symmetry. One of the key ingredients in the Haldane model is therefore presence of a mass term which gaps out the Dirac cones (see Fig. 5 (a)). Important to the story of the Haldane model is also the presence of NNN bonds. These bonds break inversion symmetry, and crucially, they realize the Haldane model when they also break time-reversal symmetry. Indeed, the absence of

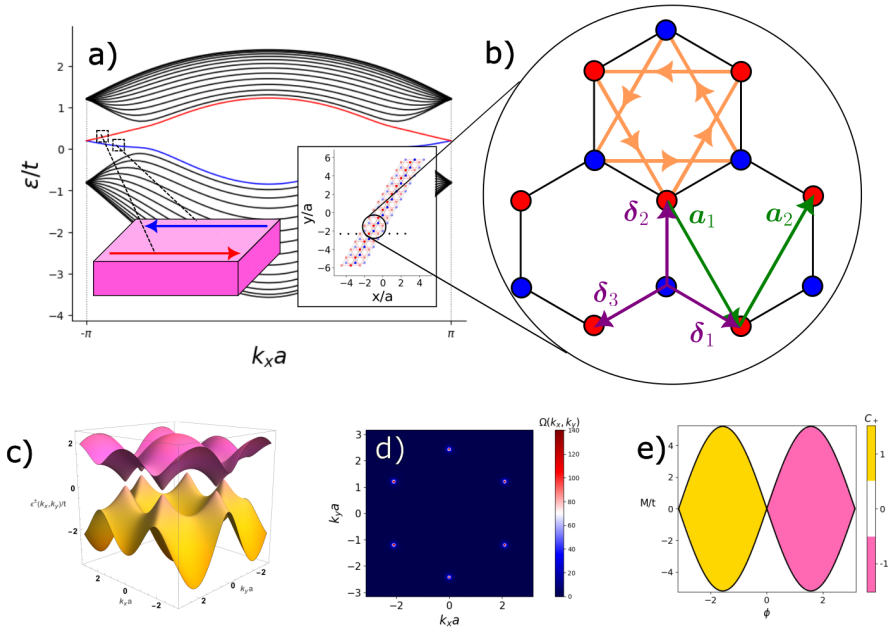

Figure 5: (a) Energy bands for a Haldane model strip in a Zigzag configuration with parameters $t_2 = t/10, t_2' = t/20, M/t = 0$. Bulk bands are represented in black, and two gapless edge modes are visible, marked in red and blue. (b) Zoom in to the structure of the honeycomb lattice, with $A(B)$ sublattice atoms marked in blue(red), nearest neighbor vectors $\boldsymbol{\delta}_i$ represented in purple, next-nearest neighbor vectors $\boldsymbol{a}_i$ in green and the orientation of Haldane model second-nearest neighbor hoppings giving the sign of the imaginary part of these hoppings in orange. (c) Energy bands of the Haldane model in an infinite system $\varepsilon^{\pm}(k_x, k_y)$. The symmetry between the bands is broken by the finite t_2. (d) Berry curvature computed analytically for the infinite system. The Berry curvature is localized near the location of the Dirac cones, justifying the linear approximation employed in the main text. (e) Phase diagram of the Chern number as a function of the Haldane flux ϕ and Haldane mass M. The envelope of the colored regions can be analytically calculated, yielding $M/t = \pm 3\sqrt{3}\sin\phi$.

time-reversal, charge-conjugation, and chiral symmetry in the Haldane model ensure it is present in the A class of the Altland-Zirnbauer classification [72, 66]. The breaking of time-reversal symmetry is achieved by making sure that an imaginary part is added to the NNN hoppings. Let $a_i^\dagger(b_i^\dagger)$ create an excitation in the $A(B)$ sublattice at site i, then the Haldane is explicitly given by the Hamiltonian

$$\begin{aligned} H_{\text{HM}} = &\sum_i M\left(a_i^\dagger a_i - b_i^\dagger b_i\right) - \sum_{\langle i,j\rangle} t_{ij} a_i^\dagger b_j + \text{h.c.} \\ &- \sum_{\langle\langle i,j\rangle\rangle} t_{2,ij}\left(a_i^\dagger a_j + b_i^\dagger b_j\right) + \text{h.c.} \\ &- i\sum_{\langle\langle i,j\rangle\rangle} t'_{2,ij}\left(a_i^\dagger a_j - b_i^\dagger b_j\right) + \text{h.c.} \end{aligned} \tag{2.9}$$

M is called the Haldane mass. The brackets $\langle\cdot,\cdot\rangle$ restrict the summation to NN bonds, and $\langle\langle\cdot,\cdot\rangle\rangle$ restrict it to NNN bonds. Note the presence of a real NNN hopping $t_{2,ij}$ and a purely imaginary hopping $it'_{2,ij}$. One can bring the two NNN hopping terms together by writing $t_{2,ij} + it'_{2,ij} = t''_{2,ij}e^{i\nu_{ij}\phi_{ij}}$,where $\phi_{ij} = \arctan\left(t'_{2,ij}/t_{2,ij}\right)$, and where $t''_{2,ij} = \sqrt{t_{2,ij}^2 + t_{2,ij}'^2}$. The factor $\nu_{ij} = \pm 1$ is then chosen according to the direction of the NNN hoppings (see Fig. 5 (b)). Summarily, the Haldane model Hamiltonian can be written as

$$\begin{aligned} H_{\text{HM}} = &\sum_i M\left(a_i^\dagger a_i - b_i^\dagger b_i\right) - \sum_{\langle i,j\rangle} t_{ij} a_i^\dagger b_i + \text{h.c.} \\ &- \sum_{\langle\langle i,j\rangle\rangle} t''_{2,ij} e^{i\nu_{ij}\phi_{ij}}\left(a_i^\dagger a_j - b_i^\dagger b_j\right). \end{aligned} \tag{2.10}$$

Following the approach described for the SSH model, a Fourier transform of the creation operators is performed, and a reciprocal space representation is employed using $a_{\boldsymbol{k}}^\dagger$ and $b_{\boldsymbol{k}}^\dagger$. The crystal momentum $\boldsymbol{k}$ is restricted to a BZ, and can be parameterized by the two components, along x and y, namely $\boldsymbol{k} = (k_x, k_y)$. The creation operators are grouped into a vector $\Psi_{\boldsymbol{k}}^\dagger = \left(a_{\boldsymbol{k}}^\dagger, b_{\boldsymbol{k}}^\dagger\right)$, such that the Hamiltonian in momentum space can be written as a bilinear form

$$H_{\text{HM}} = \sum_{\boldsymbol{k}} \Psi_{\boldsymbol{k}}^\dagger \left(h_0(\boldsymbol{k})\mathbb{1} + \boldsymbol{h}(\boldsymbol{k})\cdot\boldsymbol{\sigma}\right)\Psi_{\boldsymbol{k}}. \tag{2.11}$$

One says that this Hamiltonian is in Dirac form, since the 2×2 Hamiltonian matrix $H(\boldsymbol{k})$ is written at the cost of the Pauli matrices, which obey the Clifford algebra, and are thus the 2×2 representation of the Dirac matrices. Note that the SSH model as described in the previous section is also in Dirac form. Also, similarly to the case of the SSH model, the Haldane model is a two-band system. Explicitly, the components of the vector are $\boldsymbol{h}(\boldsymbol{k})$ and the scalar quantity $h_0(\boldsymbol{k})$ are given by

$$h_0(\boldsymbol{k}) = -\sum_j t''_{2,j} \cos\phi_j \cos\left(\boldsymbol{k}\cdot\boldsymbol{a}_j\right), \tag{2.12}$$

$$h_x(\boldsymbol{k}) = -\sum_j t_j \cos\left(\boldsymbol{k}\cdot\boldsymbol{\delta}_j\right), \tag{2.13}$$

$$h_y(\boldsymbol{k}) = \sum_j t_j \sin\left(\boldsymbol{k}\cdot\boldsymbol{\delta}_j\right), \tag{2.14}$$

$$h_z(\boldsymbol{k}) = M - 2\sum_j t''_{2,j} \sin\phi_j \sin\left(\boldsymbol{k}\cdot\boldsymbol{a}_j\right). \tag{2.15}$$

Breaking of time-reversal symmetry and chiral symmetry results in a reduced 2D target space for $\boldsymbol{h}(\boldsymbol{k})$, such that the previously described recipe for constructing a topological invariant for the system can be utilized. With some short calculations, it is possible to write the Berry curvature for $\Omega_\eta(\boldsymbol{k}) = \frac{\eta}{2}\hat{\boldsymbol{h}}(\boldsymbol{k}) \cdot \left(\partial_{k_x}\hat{\boldsymbol{h}}(\boldsymbol{k}) \times \partial_{k_y}\hat{\boldsymbol{h}}(\boldsymbol{k})\right)$, where $\eta = -1(+1)$ is utilized depending on if the Berry curvature is calculated using the valence (conduction) band, and where $\hat{\boldsymbol{h}}(\boldsymbol{k}) = \boldsymbol{h}(\boldsymbol{k})/|\boldsymbol{h}(\boldsymbol{k})|$. Now, the analogy to the Gauss-Bonnet theorem of surfaces becomes manifest. By integrating this Berry curvature over the Brillouin zone, one finds a quantized $\mathbb{Z}$ invariant

$$C_\eta = \frac{1}{2\pi}\int_{\mathrm{BZ}} d^2\boldsymbol{k}\Omega_\eta(\boldsymbol{k}). \tag{2.16}$$

This invariant is called the Chern number. One can, then, explore the parameter range of the Haldane model, and find that sharp boundaries exist between phases with $C_\eta = 0, \pm 1$ which occur precisely at points where the gap closes, leading to the breaking of the "adiabatic" condition. In particular, since the Berry curvature for the Haldane model is localized at the Dirac points (see Fig. 5 (d)), one can actually linearize the spectrum near these points and computing the integral over a linearized dispersion one finds $C_\eta = \pm 1$ depending on the model's parameters. A phase diagram is given in Fig. 5 (e). Much like the SSH model, the Haldane model hosts edge modes in a finite system when the infinite system with the same parameters is in a topologically non-trivial phase, with a non-zero Chern number. The gapless edge modes are illustrated in Fig. 5 (b). Unlike the SSH model, however, these states have a dispersion, and are degenerate only at the edges of the BZ. Furthermore, they are chiral, and one has positive and the other negative velocity when moving along the edges of a finite sample. This is yet another example of the bulk-boundary correspondence, and makes the computation of topological invariants very relevant for the phase characterization of the model.

2.2 Topology in Spin systems

2.2.1 Dirac magnon Chern insulators

Consider a HSM in a FM phase. I showed, in Chapter 1 how it can be mapped to a bosonic TBM via the Holstein-Primakoff transformations. These allow for a treatment of the low energy excitations of the HSM, namely spin-wave Goldstone modes which stem from the broken $O(3)$ symmetry of the Heisenberg model, as quantized quasiparticle excitation called magnons. Let us focus on the case of a 2D FM system in the honeycomb lattice. By itself, the corresponding HSM is far from topological, as exchange-type interactions by themselves are not enough to provide structure for the breaking of time-reversal and chiral symmetry. There is, however, one type of interaction which does provide the breeding ground for topology in 2D FM systems, which is called the Dzyaloshinskii-Moriya interaction (DMI) [80, 81]. This interaction often appears in a leading order correction to the HSM in spin-orbit coupling, and thus is a very relevant model for magnetism in the honeycomb lattice [82], and magnets with a strong intrinsic DMI can exist naturally [55]. The Hamiltonian for a HSM with second nearest neighbor interactions and a DMI reads

$$\begin{aligned} H = &-J \sum_{\langle i,j \rangle} \boldsymbol{S}_i \cdot \boldsymbol{S}_j - J_2 \sum_{\langle\langle i,j \rangle\rangle} \boldsymbol{S}_i \cdot \boldsymbol{S}_j \\ &- J_{\mathrm{DM}} \sum_{\langle\langle i,j \rangle\rangle} \hat{\boldsymbol{z}} \cdot (\boldsymbol{S}_i \times \boldsymbol{S}_j) \,. \end{aligned} \tag{2.17}$$

It is well known that the FM ground state is stable to the presence of a small value of J_{DM}. Representing this Hamiltonian at the cost of spin raising and lowering operators $S_i^{\pm}$, and performing Holstein-Primakoff bosonization, one finds that the model is mapped directly to a bosonic Haldane model. As expected the NN hoppings as well as the real part of the NNN hoppings are mapped to the corresponding exchange integrals, multiplied by the spin and the coordination number of the honeycomb lattice, which is $z = 3$. What is perhaps more surprising is that the strength of the DMI interaction J_{DM} ends up playing the role of imaginary NNN hoppings. This arises naturally from expanding the cross product in terms of spin ladder operators $S_i^{\pm}$, and is illustrated in the Appendix C in the context of synthetically engineering the DMI. By considering that there also can exist some imbalance in the $z-$component of the exchange integral between the A and B sublattice, a Haldane mass term can be recovered, which further gaps out the model. The comparisons are summarized in Table 1

Haldane	DMCI
t	JSz
t_2	J_2Sz
t_2'	$2J_{\text{DM}}Sz$
M	$(J_{z,A} - J_{z,B})S/2$

Table 1: Correspondence between the parameters of a Haldane model and the Heisenberg Spin model with the Dirac magnon Chern insulator (DMCI).

Thus, it is clear to see that this model corresponds to a magnon Chern insulator, and in the same manner described in Section 2.1.2, this model can be mapped to a Dirac Hamiltonian in reciprocal space. For this reason, low energy excitations of a magnon Chern insulator showcase a linear dispersion and are called Dirac magnons. For the sake of keeping the notation clear, I shall call such a system a Dirac Magnon Chern insulator (DMCI). A vanishing Haldane mass and DMI, of course, result in a fully linear dispersion of Dirac Magnons. In case the system is gapped, a Chern number is well defined, and thus, this construction realizes a 2D topologically non-trivial model in a spin system. The DMI is not the only type of interaction which leads to magnon bands with non-trivial Chern number, as a Kitaev-type exchange, for instance, also supports magnon bands with a non-zero Chern number. The key aspect, as before is that the interactions break time-reversal symmetry.

The DMI, however, is possibly the most common and natural type of interaction to render magnon systems topological. In fact, It has been predicted that one of the first 2D ferromagnets to be discovered, CrI_3, hosts topological magnons at the $\boldsymbol{K}$-point of the hexagonal Brillouin zone [83]. This approach, starting from a description based on itinerant electrons points to the possibly that CrI_3 may realize such a DMCI.

Similarly to electronic Chern insulators, which are able to conduct electrons along their edges and yet remain insulators in their bulk, magnonic Chern insulator samples host gapless bands for spin wave excitations along their edges while remaining gapped in the bulk. This behavior results in a measurable thermal Hall response [84, 85, 86, 87, 88, 89], and thus their technological applicability is wide in the field of spintronics and magnonics.

Even though the DMI is naturally present in some 2D magnets, it is not the case that all possible ferromagnetic materials in the honeycomb lattice host this interaction, as spin-orbit coupling may not be an important feature for their description. The desirability of topological magnon excitation has therefore lead to the theoretical study of alternative approaches to engineering a synthetic DMI. Among these is the

use lasers to exploit the Aharonov-Casher effect and photo-induce DMCIs [90, 91]. This is the content of the first sections of Chapter 3, where I will explore a Floquet theory approach to engineering topological spin systems.

2.2.2 Topological magnons in ferromagnetic SSH chains

The previous section points to a direct correspondence between a Heisenberg-type ferromagnet in a 2D hexagonal lattice with the addition of a spin-orbit induced DMI term with a bosonic Haldane model of topological magnons. In 1D, the idea of the SSH model can quite trivially be extended to a spin-based ferromagnetic SSH (FMSSH) by considering

$$H_{\text{FMSSH}} = \sum_i J_1 \boldsymbol{S}_{i,A} \cdot \boldsymbol{S}_{i,B} + J_2 \boldsymbol{S}_{i,B} \cdot \boldsymbol{S}_{i+1,A}, \tag{2.18}$$

where $\boldsymbol{S}_i^A (\boldsymbol{S}_i^B)$ are the spin-vector operators acting on the $A(B)-$sublattice, and J_1 and J_2 are distinct intra-cell and inter-cell exchange-type couplings. If an easy-axis anisotropy term $H_{EA} = K \sum_i (S_i^z)^2$, discussed in Chapter 1, is also present, the Holstein-Primakoff bosonization leads to a TBM Hamiltonian of the form

$$\begin{aligned} H_{\text{FMSSH}} = &(J_1 + J_2 + K)\, S \sum_i \left(a_i^\dagger a_i + b_i^\dagger b_i \right) \\ &- J_1 S \sum_i a_i^\dagger b_i - J_2 S \sum_i b_i^\dagger a_{i+1} + \text{h.c.}. \end{aligned} \tag{2.19}$$

Much like in 2D, the richness of topological spin systems stems from the fact that additional interactions which are in principle very unconventional in electronic systems can be natural in 1D spin systems, leading to a rich landscape of topological magnon models in ferromagnetic chains. One example is a 1D analogue of the DMI [92], which contributes with a Hamiltonian of the form

$$\begin{aligned} H_{\text{DMI}} = &J_{1,\text{DM}} \hat{\boldsymbol{z}} \cdot \sum_i \boldsymbol{S}_{i,A} \times \boldsymbol{S}_{i,B} \\ &+ J_{2,\text{DM}} \hat{\boldsymbol{z}} \cdot \sum_i \boldsymbol{S}_{i,B} \times \boldsymbol{S}_{i+1,A}. \end{aligned} \tag{2.20}$$

This analogue of the DMI interaction can also contribute to the topological properties of standard FM models as well as the FMSSH model. Another example of such an interaction is the pseudo-dipolar interaction (PDI) [92], which contributes with a Hamiltonian of the form

$$H_{\text{PDI}} = - J_{1,\text{PD}} \sum_i \left(\boldsymbol{S}_{i,A} \cdot \boldsymbol{e}_{i,i,AB}\right)\left(\boldsymbol{S}_{i,B} \cdot \boldsymbol{e}_{i,i,AB}\right) - J_{2,\text{PD}} \sum_i \left(\boldsymbol{S}_{i,B} \cdot \boldsymbol{e}_{i,i+1,BA}\right)\left(\boldsymbol{S}_{i+1,A} \cdot \boldsymbol{e}_{i,i+1,BA}\right), \tag{2.21}$$

where $\boldsymbol{e}_{i,j,AB}$ is a vector connecting the A atom of site i and the B atom of site j. The possibility of engineering these interactions enriches the topological models accessible to spin systems beyond those found in electronic systems. Indeed, the presence of the PDI can even change the ground-state properties of the FMSSH, depending on its strength, leading to an alignment along the $x-$axis, instead of the easy axis along z. Furthermore, it is clear that the FMSSH actually breaks the usual classification of topological invariant systems, since, for instance, chiral symmetry is broken by the presence of the on-site energy term in the H_{FMSSH} Hamiltonian. Indeed, in the event the Zak phase is non-zero, edge states appear at the middle of the energy spectrum, and not at zero energy as in the electronic SSH model. The topology of the FMSSH chain is therefore protected only by time-reversal and inversion symmetry, and if both the DMI and PDI are present even inversion symmetry is lost, leaving only time-reversal symmetry. Thus, despite its similarities, the FMSSH model is not in direct correspondence with other types SSH model as described in Chapter 1. Regardless, the FMSSH model can always be written in momentum space at the cost of HP bosons as $H = \sum \Psi_k^\dagger H(k) \Psi_k$, where $\Psi_k^\dagger = \left(a_k^\dagger, a_{-k}, b_k^\dagger, b_{-k}\right)$ and with $H(k) = H_{\text{FMSSH}}(k) + H_{\text{DMI}}(k) + H_{\text{PDI}}(k)$ corresponding to a 4×4 Hamiltonian matrix. $H(k)$ obeys the generalized eigenvalue problem [40]

$$U^\dagger(k) \eta H(k) U(k) = \eta \varepsilon_k, \tag{2.22}$$

where $U(k)$ diagonalizes the Hamiltonian matrix and $\eta = \mathbb{1} \otimes \sigma_z$ is a metric matrix accounting for the possibility of the system being in the $x-$FM ground state with terms in the PDI Hamiltonian involving products of the form $a_i b_j$ or $a_i^\dagger b_j^\dagger$. Despite this richness of phases for the FMSSH model, I will keep the following discussion restricted to the case of a $z-$FM ground-state, and ignore both DMI and PDI from now on. Indeed, I will also stick to XY-type SSH models, thus ignoring the contribution from S_i^z to H_{FMSSH} and restoring chiral symmetry. The FMSSH model discussed throughout this thesis is therefore, a restricted version of the rich FMSSH landscape, in order to remain compatible with the standard topological protection of the BDI class of the Altland-Zirnbauer periodic table [72]. As such, it can be described in terms of a 2×2 Dirac Hamiltonian, and and the analysis of its topological properties can proceed through the calculation of Winding numbers. Nevertheless, it is worth noting that richer behavior could be studied by considering these additional interactions using alternative methods such as real space topological markers [93, 92].

Part II

Core of the Dissertation

Chapter 3

Strain Engineering Photo-induced Dirac Magnon Chern Insulators

With the experimental observation of magnetic order in two-dimensional (2D) materials in 2017 [94, 95], as described in Chapter 1 and the simultaneous growth in interest in topological aspects of condensed matter systems over the past decade, the ability to generate, study, and manipulate topological phases of magnetic materials has become a rapidly growing research direction. Systems such as Magnon Chern Insulators, presented in Chapter 2 have been theoretically studied [96] and experimentally verified in the past few years [97, 98]. The reason for this interest is that topology describes effects which stem from global properties of the band structure robust to small local perturbations, such as impurities, and can have a profound effect on a the material physical properties. As discussed in Chapter 2, topological insulating phases are characterized, for instance, by the presence of chiral edge states with high mobility. Their robustness is desirable for a variety of applications such as spintronics, and ensuing technological implementations [99]. It is evident that for such applications, the ability to manipulate topological phases, whether by switching topological properties on or off, or alternating between distinct topological phases, are desirable goals.

Additionally, magnon based approaches to spintronic technologies have also gained traction for a variety of reasons [100]: From their ability to propagate without generating electrical current and therefore reducing losses, to the possibility of making use of their internal degrees of freedom to implement logic gates [101, 102], and to their large diffusion lengths in comparison to electrons [103, 104, 105], magnons have garnered attention as a convenient excitation for processing and transporting information. For this reason, magnon spintronics relies on the use of magnons as intermediate agents, being that information initially coded in charge or spin of electrons can be converted to magnon currents, subsequently dispatched to and handled at potentially different devices, and finally converted back. In combination with the attractiveness of topology, the use of magnons renders the study of topological spin systems a

worthwhile endeavor for the development of spintronic devices [106, 107].

One possibility for engineering topology in spin systems relies on the fact that a DMCI with a strong intrinsic DMI can have the magnitude of this interaction renormalized when irradiated by a circularly polarized laser field [90, 91]. A field-dependent renormalization of the DMI can result in the possibility of the topological properties of spin systems being manipulated, such as the direction of edge state conduction being reversed or entirely switched off, by changing the magnitude of the applied electric field. In addition, a DMI resulting entirely from the interaction of laser fields with spins [90] can also be generated. In this manner, if a material does not naturally host such an interaction, it can be synthesized by a laser beam, yielding a so-called Floquet Magnon Chern insulator (FMCI). In case the material's intrinsic DMI is weak compared to such a synthetic term, the control of topological properties is limited: Increasing the intensity of the laser field can turn the interaction on or off, but doesn't provide a way to reverse edge spin states or additional desirable features. Besides, this limited tuning occurs only for very precise (and large) values of the intensity of the applied fields. Thus, if it were possible to induce this interaction in a fully tunable manner to a larger class of materials, one expects that new technological developments based on topological spintronics could arise. This chapter addresses the manipulation of these topological states by proposing a method based on elastically deforming, i.e. straining, a 2D magnetic material. Strain can be applied in a variety of ways, including the deposition of a 2D material onto, and subsequent deformation of an elastic substrate [108]. It has proven to be an extremely powerful tool in semiconductors, as well as in 2D materials such as graphene, where band structure properties can be manipulated [109, 110], and other electronic properties can be locally changed using patterned substrates. These patterns, such as bends or folds, wells, bubbles, and troughs can induce mechanical strain on an overlaid mono-layer of material, and may be used to design all-graphene integrated circuits [111]. In Cr_2Te_3, strain engineered magnetism has been observed [112] and when it comes to topology, strain in the Haldane model has also been theoretically considered in the past [113], where it has been shown to be able to induce topological phase transitions to a trivial state. The DMI can also be subject to changes due to strain [114], and this conjugation of factors is a good indicator that strain is a useful tool when considering topological properties of magnetic materials. I show here that this is indeed the case, as straining a 2D ferromagnet irradiated by a laser field can invert the sign of its topological invariant, as well as induce a transition from a topologically insulating phase to the trivial phase.

These calculations, lying at the interface between Strain Engineering and Floquet Engineering may pave the way for a new class of Strain Engineered Topological Spintronic (SETS) devices, based on local applications of strain to ferromagnetic 2D materials. They provide mechanism for the realization of tunable

photo-induced topology in a large class of 2D ferromagnetic materials based on strain. I will draw phase diagrams based on the computation of the Floquet Chern number for a FMCI in the honeycomb lattice, as a function of tensile strain and the magnitude of an applied laser field which clearly exhibit strain-driven transitions. Two main cases are considered: First, a next-nearest neighbor (NNN) interaction is given by a DMI alone; and second, an extension of this model where one also considers an additional NNN Heisenberg coupling. I show that strain-induced topological phase transitions occur in both systems. However, due to the mapping between the latter model and an anisotropic Haldane model with the key property of tunable fluxes, phase transitions can occur for smaller electric field intensities, and small amounts of strain. Such a model could provide the breeding ground for new developments based on SETS. The discussion presented in this chapter can also be found in [115].

3.1 Introduction to Floquet magnon Chern insulators

3.1.1 The Floquet magnon Chern Insulator

The driving of materials by time-periodic fields, as detailed in the previous section has potential for the engineering of novel, out of equilibrium topological phases, and tools from Floquet theory help in deriving effective time-independent Hamiltonians in the limit of high driving frequency. A detailed account of Floquet theory and the key approximation for this section is given in Appendix B. Magnetic systems are no exception to the applicability of this type of driving protocol, and here I will describe the basics of the magnetic model that serves as the basis for this proposal by considering what is called a Floquet Magnon Chern insulator in a honeycomb lattice of spin S atoms.

The starting point for this model is an HSM which couples spins at NN and NNN sites via in-plane exchange integrals $J_\perp$ and $J_{2,\perp}$, respectively, as well as their J_z and $J_{z,2}$ counterparts. A distinction is made between the in-plane and out of plane components explicitly, since as I will show, the effects of periodic driving affect these components differently. The Hamiltonian for the undriven HSM reads

$$\begin{aligned} H_{\text{HSM}} = &\sum_{\langle i,j\rangle} \frac{J_\perp}{2} S^+(\boldsymbol{r}_i) S^-(\boldsymbol{r}_j) + \text{h.c.} \\ &+ \sum_{\langle\langle i,j\rangle\rangle} \frac{J_{2,\perp}}{2} S^+(\boldsymbol{r}_i) S^-(\boldsymbol{r}_j) + \text{h.c} \\ &+ \sum_{\langle i,j\rangle} J_z S^z(\boldsymbol{r}_i) S^z(\boldsymbol{r}_j) + \sum_{\langle\langle i,j\rangle\rangle} J_{2,z} S^z(\boldsymbol{r}_i) S^z(\boldsymbol{r}_j), \end{aligned} \tag{3.1}$$

This HSM actually corresponds to a Dirac magnon insulator, and as previously discussed, hosts ultra-relativistic magnonic excitations near the $\boldsymbol{K}$ and $\boldsymbol{K}'$ points of the Brillouin zone. An FMCI is built from the HSM quite subtly, as the fact that an electric field alone can couple to magnons, is, in principle, not so obvious. The key effect that comes into play, which allows for the direct coupling of an electric field to neutral bosons which carry a magnetic moment, such as Dirac magnons, is the Aharonov-Casher (A-C) effect [64], mentioned in Chapter 1. For a ferromagnet irradiated by a circularly polarized laser field $\boldsymbol{E}(t) = E_0\,(\tau\cos\omega t, \sin\omega t, 0)$, with handedness given by $\tau = \pm 1$, and with frequency ω, the A-C phase manifests itself as a time-dependent Peierls phase acquired by the Dirac magnons when hopping between different lattice sites.

$$\gamma_{ij}^{AC}(t) = -\frac{\mu_B E_0}{\hbar c^2}\int_{\boldsymbol{r}_i}^{\boldsymbol{r}_j} d\boldsymbol{R}\cdot(\sin\omega t, \tau\cos\omega t, 0)\,. \tag{3.2}$$

The amplitude of the A-C phase is determined by that of the electric field as well as the reduced Planck's constant $\hbar$, the speed of light in vacuum c and the Bohr magneton μ_B. For the sake of simplicity, I define an inverse length scale $\alpha \equiv \mu_B E_0/\hbar c^2$ used throughout the following discussion. The Hamiltonian resulting from the driving is

$$\begin{aligned} H =& \sum_{\langle i,j\rangle}\frac{J_\perp e^{i\gamma_{ij}^{AC}(t)}}{2}S^+(\boldsymbol{r}_i)S^-(\boldsymbol{r}_j) + \text{h.c.} \\ &+ \sum_{\langle\langle i,j\rangle\rangle}\frac{J_{2,\perp} e^{i\gamma_{ij}^{AC}(t)}}{2}S^+(\boldsymbol{r}_i)S^-(\boldsymbol{r}_j) + \text{h.c} \\ &+ \sum_{\langle i,j\rangle} J_z S^z(\boldsymbol{r}_i)S^z(\boldsymbol{r}_j) + \sum_{\langle\langle i,j\rangle\rangle} J_{2,z}S^z(\boldsymbol{r}_i)S^z(\boldsymbol{r}_j), \end{aligned} \tag{3.3}$$

The time dependence of the resulting Hamiltonian may appear initially cumbersome, but using the Floquet theory framework, and specifically the previously explored high-frequency approximation [116], the resulting synthetic Hamiltonian has a clear qualitative and physical interpretation up to $\mathcal{O}(\omega^{-1})$. The correction of lowest order $\mathcal{O}\,(\omega^0)$ in high-frequency provides an averaging of the Hamiltonian over a period of the driving laser, yielding a renormalization of the NN and NNN in-plane exchange integrals as $J_\perp \to J_\perp\mathcal{J}_0(\tau\alpha a_0), J_{\perp,2} \to J_{\perp,2}\mathcal{J}_0(\tau\alpha\sqrt{3}a_0)$, (equation (3.4)) where $\mathcal{J}_n(x)$ are the nth order Bessel functions. The functional form of the renormalization of the NN in-plane hoppings is already interesting despite not providing topological properties by itself, as it depends on a Bessel function of order 0 for the case of the NN hoppings. This allows for tuning between Heisenberg type-couplings and Ising type couplings, for instance, since all $J_\perp$ can be turned off. In the literature one often defines the dimensionless

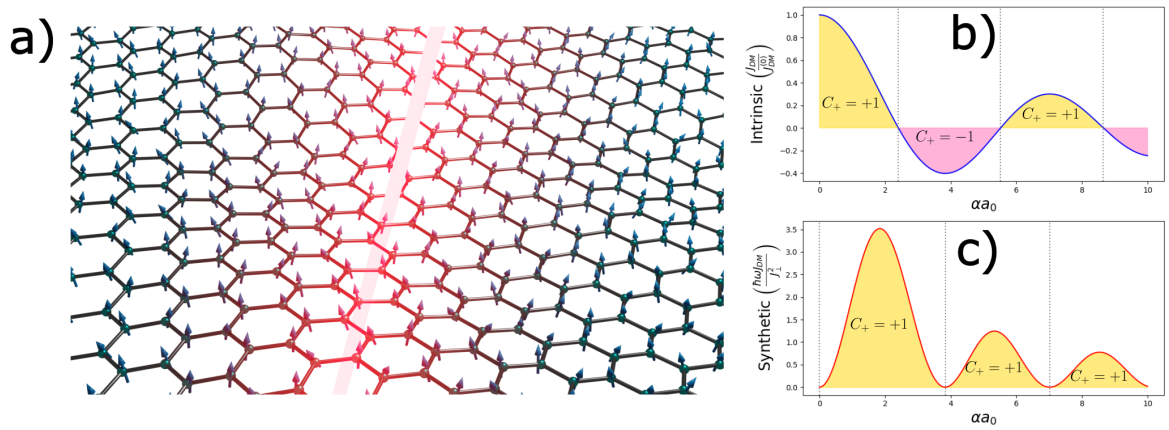

Figure 6: (a) Artistic rendition of the experimental setup for the realization of the Floquet magnon Chern insulator (FMCI). (b) Renormalization of the DMI in a DMCI via the Floquet theory to first order in the high-frequency expansion a function of the applied electric field. (c) DMI strength as generated solely by the laser field in the second order high-frequency expansion. The dashed vertical lines in (c) and (d) showcase the field values for which the DMI can be tuned to zero, yielding a trivial magnon insulator.

parameter $\lambda = \alpha a_0$, and this notation is employed in the Appendix C. Here, however, I make here explicit the additional knob for this model, which is the key ingredient to the results showcased in this work. This is the inter-atomic distance a_0.

Besides this first order correction, corresponding to the renormalization of $J_\perp$ and $J_{\perp,2}$, the second-order high-frequency correction can be seen to yield an additional term in the effective Hamiltonian, in the form of a spin-chirality (equation (3.5)). The Hamiltonian will read $H_F = \hat{H}_F^{(1)} + \hat{H}_F^{(2)} + \mathcal{O}\left(1/\omega^2\right)$, and the two first terms in the high-frequency expansion explicitly read

$$\begin{aligned}\hat{H}_F^{(1)} = &- \sum_{\langle i,j\rangle} J_\perp \mathcal{J}_0(\tau\alpha a_0) S^+(\boldsymbol{r}_i) S^-(\boldsymbol{r}_j) + \text{h.c.}, \\ &- \sum_{\langle i,j\rangle} J_z S^z(\boldsymbol{r}_i) S^z(\boldsymbol{r}_j) - \sum_{\langle\langle i,j\rangle\rangle} J_{2,z} S^z(\boldsymbol{r}_i) S^z(\boldsymbol{r}_j) \\ &- \sum_{\langle\langle i,j\rangle\rangle} J_{2,\perp} \mathcal{J}_0(\tau\alpha\sqrt{3}a_0) S^+(\boldsymbol{r}_i) S^-(\boldsymbol{r}_j) + \text{h.c.}, \end{aligned} \tag{3.4}$$

$$\hat{H}_F^{(2)} = \sum_{\langle i,\langle j\rangle,k\rangle} \chi_{ijk} \boldsymbol{S}(\boldsymbol{r}_i) \cdot \left(\boldsymbol{S}(\boldsymbol{r}_j) \times \boldsymbol{S}(\boldsymbol{r}_k)\right), \tag{3.5}$$

where I have introduced interlinked braces $\langle\cdot, \langle\cdot\rangle, \cdot\rangle$ to indicate that the summation is performed over NNN atoms at positions i and k, which are connected by position j. In equation (3.5), the spin-chirality

is given in magnitude by

$$\chi_{ijk} = \tau\sqrt{3}J^2\mathcal{J}_1(\tau\alpha\delta_{ji})\mathcal{J}_1(\tau\alpha\delta_{ik})\nu_{ik}^{A/B}/\hbar\omega, \tag{3.6}$$

where $\nu_{ik}^{A} = -\nu_{ik}^{B} = -\nu_{ki}^{A}$ is a flux-like term, dependent on the orientation of the NNN bonds which connect sites i and k according to the orange arrows in Fig. 8, panel (a). Note that the intensity of the spin-chirality depends on the successive hoppings between an intermediate site via the first order Bessel functions. The derivation of both of these terms is provided in some detail in the Appendix C. At this stage, all the distances $\delta_{ji} \equiv |\boldsymbol{\delta}_i|a_0 = a_0$ are the same, and equal the inter-atomic distance. As such, it is possible to write $\mathcal{J}_1(\tau\alpha\delta_{ji})\mathcal{J}_1(\tau\alpha\delta_{ik}) = \mathcal{J}_1^2(\tau\alpha a_0)$. This makes it so sign $(\chi) = \tau$ for any possible value of $\alpha \propto E_0$. Such a spin chirality term is known to originate frustration in the ground state of the ferromagnetic system, leading to the possibility of originating spin-liquid states, but considering $J_z > J_\perp$ the FM ground state is stabilized. In this regime, while the DMI provides the grounds for a topologically non-trivial phase, a FM ground state is kept.

For pursuing this discussion, a second quantization formalism for magnons can be employed using the Holstein-Primakoff (HP) bosonization. Within linear spin-wave theory, the spin-chirality is indistinguishable from a DMI (see Section 2.2.1 for a brief explanation of the DMI's effects on topology). Indeed, when writing this term using HP operators, and retaining only terms up to second order in such operators, this equivalence becomes clear. As discussed in Chapter 2, writing the Hamiltonian for a HSM with a DMI in momentum space can be achieved in terms of the Pauli matrices, yielding a familiar Dirac Hamiltonian matrix $H(\boldsymbol{k}) = h_0(\boldsymbol{k})\mathbb{1} + \boldsymbol{h}(\boldsymbol{k}) \cdot \boldsymbol{\sigma}$.

This model is mapped directly to a bosonic Haldane model, and in particular, to a DMCI. The topological invariant is now called the Floquet Chern number C_η^F as a reminder of the synthetic nature of the model's topological properties. To summarize the relationship of the FMCI to the previously discussed Haldane model (HM), Dirac magnon Chern Insulator (DMCI), I compile the identifications between the models parameters in Table 2.

HM	DMCI	FMCI
t	JSz	$J_{\perp}Sz\mathcal{J}_0(\alpha a_0)$
t_2	J_2Sz	$J_{2,\perp}Sz\mathcal{J}_0(\alpha\sqrt{3}a_0)$
t_2'	$2J_{\mathsf{DM}}Sz$	$2\sqrt{3}J_{\perp}^2S^2\tau\mathcal{J}_1(\alpha\delta_{ij})\mathcal{J}_1(\alpha\delta_{jk})z/\hbar\omega$
M	$(J_{z,A}-J_{z,B})S/2$	$(J_{z,A}-J_{z,B})S/2$

Table 2: Identifications between Haldane model (HM), Dirac magnon Chern Insulator (DMCI) and Floquet Magnon Chern insulator (FMCI).

It is especially worth noting that if one writes the NNN interaction for the FMCI as $\sqrt{t_2^2+t_2'^2}e^{i\phi_{ij}}$, the Haldane flux ϕ_{ij} becomes dependent on the intermediary site k between i and j, and reads $\phi_{ijk}=\arctan\left(\frac{J_{\perp}^2\tau}{J_{2,\perp}\hbar\omega}\frac{\mathcal{J}_1(\alpha\delta_{ik})\mathcal{J}_1(\alpha\delta_{kj})}{\mathcal{J}_0(\alpha\sqrt{3}a_0)}\right)$. From a simple analytical result for C_{η}^F given by expanding the energy spectrum near the Dirac points, and for a fixed polarization of light τ, one finds, so long as $J_{2,\perp}=0$, a result $C_{\eta}^F=\eta\tau$ can be obtained following the approximations detailed in Chapter 2, regardless of the intensity of the laser field. With the exception of very special values of electric field, only $C_{\eta}=\pm1$ phases are obtained under driving. At the points for which $\mathcal{J}_1^2(\tau\alpha a_0)=0$, however, the system becomes trivial with $C_{\eta}^F=0$. Thus, it is clear, for a HSM in the honeycomb lattice, that the Floquet engineering approach can lead to topologically non-trivial properties. Regardless, it is the case that the manipulation of this topology is somewhat limited, with transitions to a trivial phase occurring at very specific points. Also taking into account the fact that topological transitions occur for very high values of electric field $E_0\approx1\times10^{13}$V/cm, I propose here a way to increase the tuneability of the FMCI, by using a strain engineering approach, while also lowering this critical value. This proposal is explored in the remaining section of this chapter.

3.2 Straining Floquet Magnon Chern Insulators

3.2.1 Strained FMCI with NN hoppings

As previously described, for a magnetic material with a strong intrinsic DMI, sign (χ) can be manipulated by changing the intensity of the laser field, due to the first order correction of the high frequency approximation, which reads $\chi\rightarrow\mathcal{J}_0(\alpha a_0)\chi$ as illustrated in Fig. 6 (b). For systems where the DMI is fully synthetic and results only from second order Floquet theory, this does not appear possible due to the dependence

in $\mathcal{J}_1^2(\tau\alpha a_0) > 0$, as in Fig. 6 (c). Guided by the fact that a sign change can be achieved by making the system anisotropic and transforming $\mathcal{J}_1^2(\tau\alpha a_0) \rightarrow \mathcal{J}_1(\tau\alpha\delta_{ji})\mathcal{J}_1(\tau\alpha\delta_{ik})$, where δ_{ij} are inter-atomic distances in a deformed hexagonal lattice, I will now explore the uniaxial straining of an FMCI, and show that even small amounts of strain can provide a pathway for topological manipulations of the model. Note that studies on the exchange parameters in CrI_3 as function of strain have been considered theoretically analyzed in the past, considering strain values up to 10% [117].

In the honeycomb lattice, the strain tensor is described by two parameters alone, namely the tensile strain ε and the Poisson ratio ν [118]. When inducing stress onto the 2D magnetic material, the tensile strain ε is proportional to this stress, and therefore one can treat ε as the tunable parameter in the system. It measures the amount of deformation in the direction of the applied stress, while the Poisson ratio measures the deformation of the lattice in the transverse direction. A positive Poisson ratio $\nu > 0$ indicates that when a material is stretched in a particular direction, it compresses in the transverse direction, and vice-versa. As such, the lattice vectors acquire a functional dependence on the parameters ε and ν, as strain applied in a particular direction. The deformed vectors read $\boldsymbol{\delta}_i(\varepsilon,\nu,\theta) = \left(1+\bar{\bar{\varepsilon}}\right)\boldsymbol{\delta}_i^{(0)}$,where the strain tensor is

$$\bar{\bar{\varepsilon}} = \varepsilon \begin{bmatrix} \cos^2\theta - \nu\sin^2\theta & (1+\nu)\cos\theta\sin\theta \\ (1+\nu)\cos\theta\sin\theta & \sin^2\theta - \nu\cos^2\theta \end{bmatrix}. \tag{3.7}$$

In the simplest TBM approach, strain can be included in a given Hamiltonian via modifying hopping amplitudes anisotropically. In previous works in the honeycomb lattice, it is considered that electronic hoppings are exponentially suppressed when the bond length is increased [119]. This is the simplest possible model, which can be intuited phenomenologically from the overlap of atomic orbitals. One has

$$\text{(NN): } t_{ij} = t^{(0)} e^{-\beta(\delta_{ij}(\varepsilon,\nu,\theta)-1)}, \tag{3.8}$$

$$\text{(NNN): } t_{2,ij} = t_2^{(0)} e^{-\beta\left(a_{ij}(\varepsilon,\nu,\theta)-\sqrt{3}\right)}, \tag{3.9}$$

where β is a phenomenological parameter of the order of unity. Since it is expected that the strength of the exchange interaction is $J \propto t^2/U$ for U representing the strength of on-site Coulomb repulsion in some underlying electronic model, it is natural to consider that a similar exponential decay occurs for J with the rate of 2β. The inclusion of such a phenomenological correction in a standard Haldane model is enough to produce topological phase transitions, when a system is strained in the Zig-zag direction with values of, for instance, $\varepsilon \sim 15\%$ for a Haldane flux of $\phi = 4\pi/5$, due to a fusion of the magnonic Dirac cones. This is presented in Fig. 7.

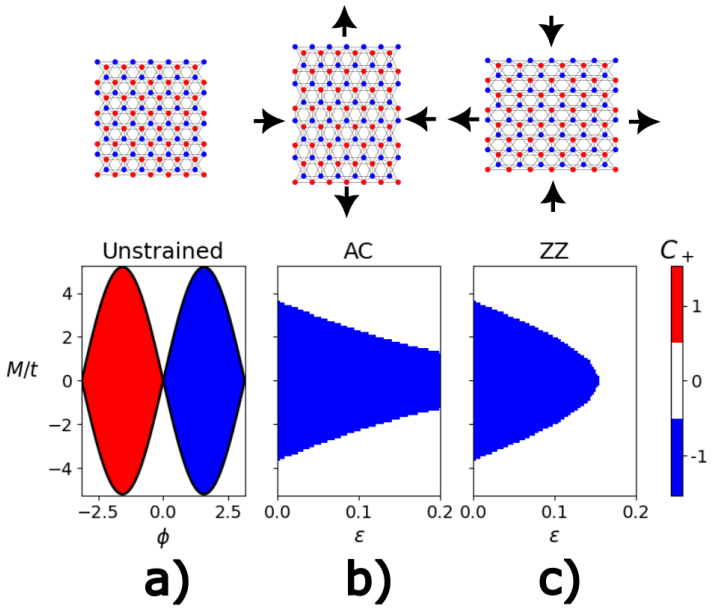

Figure 7: (a) Phase diagram for a bosonic Haldane model as a function of the Haldane mass M and the phase ϕ. Black lines in this panel indicate $M = \pm 3\sqrt{3}\sin\phi$, which are the analytical results for the phase transitions in this model. (b) Phase diagram for the strained bosonic Haldane model in the Zig-zag (ZZ) direction as a function of M and the strain magnitude ε. (c) Phase diagram for the strained bosonic Haldane model in the Armchair (AC) direction as a function of M and ε. For all diagrams, the parameters $\beta = 3.37$, $\nu = 0.165$ and a phase of $\phi = 4\pi/5$ are picked, such that for strain applied in the ZZ direction, for any value of M and a strain above $\sim 15\%$, the model is in a trivial phase. Generically, for strain in the AC direction, no phase transitions are observed for $M = 0$.

For a standard DMI system, if $J_{2,z/\perp} = 0$, i.e. an Haldane flux is present corresponding to $\phi = \pi/2$, the critical strain necessary for a topological phase transition can be much higher, making it unfeasible for realistic applications. On the other hand, rich phase diagrams emerging from uniaxially straining a FMCI can appear. This is due to the intricate dependence of NN and NNN hoppings on Bessel functions, as presented in Table 3. The simplest case is analyzed first, with $J_{2,z} = J_{2,\perp} = 0$.

HM	Strained FMCI
t	$J_{\perp} S z \mathcal{J}_0(\alpha\delta_{ij}) e^{-2\beta(\delta_{ij}-1)}$
t_2	$J_{2,\perp} S z \mathcal{J}_0(\alpha a_{ij}) e^{-2\beta\left(a_{ij}-\sqrt{3}\right)}$
t_2'	$2J_{\perp}^2 S^2 \tau \mathcal{J}_1(\alpha\delta_{ik}) \mathcal{J}_1(\alpha\delta_{kj}) e^{-2\beta\left(\delta_{ik}+\delta_{kj}-2\right)} z/\hbar\omega$
M	$(J_{z,A} - J_{z,B})S/2$

Table 3: Identifications between Haldane model and Strained Floquet Magnon Chern insulator.

The functional dependence on Bessel functions can result in the closing of the gap of the system well below strain values of 15%, and break the symmetry of the lattice in such a way that the system becomes topologically trivial, or even switch the relative sign of NN and DMI. Indeed, this NN sign-switch plays a more relevant role at a lower value of the intensity of the electric field, for any reasonable value of strain. Thus, from an experimental point of view, such a transition may be more easily accessed. Fig. 8 shows that both if stress is applied in either the Zig-zag as well as Armchair directions of the honeycomb lattice, there exist several points, near the zero of $\mathcal{J}_0(\alpha|\delta_1(\varepsilon,\nu,\theta)|a_0) = \mathcal{J}_0(\alpha|\delta_3(\varepsilon,\nu,\theta)|a_0)$, at which a transition between a Floquet Chern number $C_-^F = -1$ to $C_-^F = 1$ can occur, even for very small values of strain. For strain applied in the Armchair (AC) direction, a large region of Chern number $C_-^F = +1$ occurs for strain above 12.5% and αa_0 above the first zero of $\mathcal{J}_0$, whereas for strain applied in the ZZ direction, transitions to a trivial phase can occur for a much smaller field intensity.

The generic behavior of the transitions, is that several dips in critical strain occur within the phase diagram, close to zeros of the Bessel functions $\mathcal{J}_0$ and $\mathcal{J}_1$. As described in the section on realistic parameter values, $\alpha a_0 = 2.3$, which corresponds to the location of the first dip for which transitions occur for low values of strain, is still quite a large field intensity. This leads to the question of whether there exist any mechanism which can lower this critical value further.

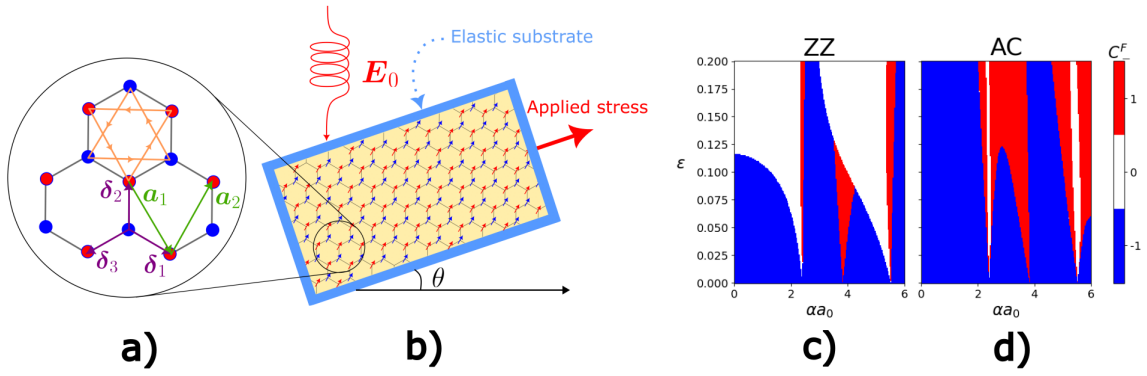

Figure 8: (a) Honeycomb lattice structure: A (B) sub-lattice atoms are marked in blue (red). NN vectors $\boldsymbol{\delta}_i$ are displayed in purple and NNN vectors $\boldsymbol{a}_i$ are displayed in green. Orange arrows in the topmost honeycomb shape showcase the flux factor of the Dzyaloshinskii-Moriya interaction. (b) Schematic for the setup for straining a ferromagnetic 2D material at an angle θ if stress is applied along the large blue arrow. An external electric circularly polarized electric field is applied with magnitude E_0 leading to the tunable topological properties described in the main text. Throughout the text I will consider $\theta = 0$ corresponding to zig-zag (ZZ) strain, and $\theta = \pi/2$, corresponding to armchair (AC) strain. (c)-(d) Phase diagrams showcasing the Chern number as a function of the electric field through αa_0 as well as the strain magnitude ε in the ZZ and AC directions for a FMCI with $J_2 = 0$ and $\hbar\omega = 50J$. (c) Strain in the ZZ direction: A series of dips is observable for which at certain values of electric field, small amounts of strain are necessary to induce a topological phase transition. The first white dip corresponds to a situation where $\mathcal{J}_0(\alpha|\delta_1|a_0)$ and $\mathcal{J}_0(\alpha|\delta_3|a_0)$ go to zero. The subsequent transitions in each dip occur either because of this or due to changes in the DMI sign due to $\mathcal{J}_1$. (d) Strain in the AC direction: A similar situation occurs, with the first dip being related to the position of the zero of the NN exchange integrals, and the second dips occur due to the DMI sign change.

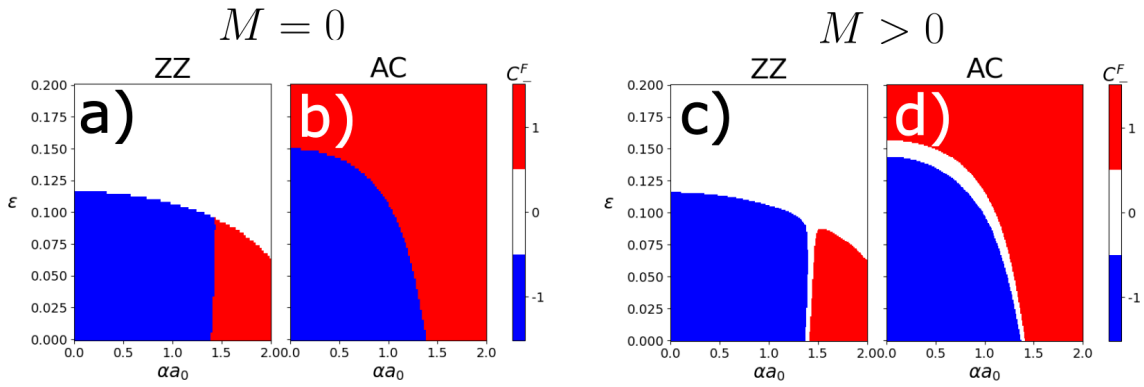

Figure 9: Phase diagrams showcasing the Chern number as a function of the electric field through αa_0 as well as the strain magnitude ε in the Zig-zag and Armchair directions, with $J_2 = 0.1J$ and $\hbar\omega = 50J$. (a) and (c): Strain in the Zig-zag direction. (b) and (d): Strain in the Armchair direction. There exist critical strain values for field arbitrarily close to zero, as well as critical field values for arbitrarily small strain near $\alpha a_0 \approx 1.38$, for which topological transitions can occur between phases with inverse Chern numbers. (a)-(b) showcase the $M = 0$ limit, while (c)-(d) showcase the effect of a finite mass $M = 3.3 \times 10^{-3} JS$ on the phase diagram, opening a trivial phase between the topological phases with opposite Chern number.

3.2.2 Strained FMCI with NNN hoppings

I now show that by turning on the NNN exchange integral $J_2 > 0$, which is renormalized by the laser field, the mapping to the Haldane model must also include a flux $\phi_{ijk} = \arctan\left(\chi_{ijk}/J_{2,ik}\right)$. The quantities χ_{ijk} and $J_{2,ik}$ depend on αa_i in distinct manners. This phase becomes tunable with the electric field intensity, leading to another mechanism for tuning the topological phase. In this case, the phase diagram acquires two interesting features showcased in Fig. 9, especially evident for strain applied in the AC direction. A critical value of electric field exists which provides a transition for vanishing values of strain for a much lower value of electric field $\alpha a_0 \approx 1.38$. The value for the critical electric field is also decreased until it vanishes, at a strain of about 15%. Tuning the strain with high precision near this value can allow for an inversion of the sign of the Floquet Chern number for an arbitrarily small electric field. In the ZZ direction, a similar situation occurs for topological to trivial transition, near 11% strain, and this value can be reduced to about 9.5% strain while remaining in the $C_-^F = -1$ phase by increasing α. I consider these to be the most important results of this chapter, as small values of strain can be achieved by overlaying a 2D magnetic material in a patterned substrate, and thus precise control of topological phases can be obtained in integrated devices.

Another aspect which is also worth mentioning is that in the limit where $M \to 0$, the transitions

between phases with opposed Chern number occur directly, as can be seen in Fig. 9. On the other hand, for $M > 0$, finite regions of trivial phases crop up in between those characterized by Floquet Chern number $C_-^F = -1$ and $C_-^F = +1$, as seen in Fig. 9. This results in an intermediate phase with $C_-^F = 0$, which may be useful in an experimental context, as it provides a clear barrier between distinct topological phases.

3.2.3 Parameter values and realistic realization

It is now worthwhile to review and justify the choice of parameters used for these calculations, since some are yet undetermined experimentally at the present time. Parameters such as the Poisson ratio ν for monolayer ferromagnetic materials, for instance, have not yet been subject to thorough experimental analysis, and hence for a rough estimate of the effects of the strain, I have used $\nu = 0.165$ corresponding to the case of graphene, the most well known 2D material with a honeycomb structure [110]. I also pick $\beta = 3.37$, corresponding to the value obtained experimentally for graphene [120]. The electric field at which the first transition occurs for small strain lies around $\alpha a_0 \approx 2.3$, but is lowered for increased values of strain in the AC direction in the case of$J_2 = 0$. Using the distance between magnetic atoms in CrI_3 as a rough estimate, a critical electric field of the order of $E_0 \approx 1 \times 10^{13}$V/cm is necessary to induce a transition. Lasers of up to 10^{23}W/cm^2 have been reported [121], which allow for laser fields of up to roughly $E_0 \approx 9 \times 10^{12}$V/cm. Although this value is of the order of magnitude of the field necessary to induce topological phase transitions in the system, the authors recognize that it still is quite a high value of electric field, which may result in damage to the material or otherwise undesirable out-of equilibrium phenomena to take place. This renders the topological phase transitions in a $J_2 = 0$ model, likely out of reach. However, as these calculations show, for $J_2 > 0$, the critical electric fields are much smaller, and the topological gap is stabilized, facilitating an experimental implementation in essentially every regard. For increasing values of strain in the AC direction up to a critical value of 15% a transition occurs for vanishing field intensity (see Fig. 9). In the ZZ direction, a trivial phase can be reached for values of up to 11% strain. Furthermore, I use $\hbar\omega = 50J$, which leads to a frequency of $\omega/2\pi \approx 1.2 \times 10^{13}$Hz, lying in the 10s of THz, achievable using ultra-fast terahertz spectroscopy [90]. It should also be noted that, for 2D ferromagnetic materials, the choice of parameters is a conservative estimate. Since graphene is known to have very strong carbon-carbon bonds, it is expected that realistic values of β may be much larger for other relevant materials, compatible with a quicker decay of electronic bond strengths. This actually reduces critical strain values. For instance, if β is doubled, strain in the ZZ direction can cause a topological phase transition at magnitudes as low as 5%. On the other hand, it may be the case that ν is

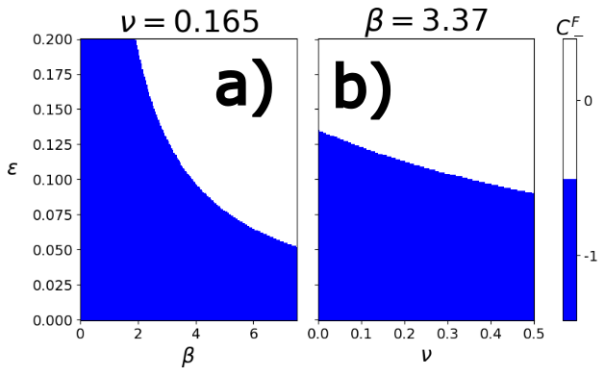

Figure 10: Phase diagrams for the Floquet Magnon Chern insulator with a small applied electric field $\alpha a_0 = 0.01$, varying strain in the ZZ direction as well as parameters β (a) and ν (b). When one such parameter is varied the other is kept constant at the values highlighted above the plots. Increasing either β or ν results in the lowering of the critical strain which induces a topological phase transition.

actually smaller, and this would, in turn, result in an increased critical strain magnitude. This points to a necessity of further exploring elastic properties of 2D magnetic materials. The variation of the critical strain magnitude in the ZZ direction with both β and ν is given in Fig. 10. It is also worth noting that increasing the strength of J_2 relative to J does not alter the phase diagrams presented in any way, although it does increase the magnitude of the topological gap. Hence, if a material actually exhibits a greater value of J_2, this can ameliorate the conditions for a physical implementation of SETS.

Finally, and in order to discuss an alternative system in which these ideas could be tested, it is worth mentioning that the coupling between electrons and electric fields is much stronger. A number of papers have proposed the realization and study of photo-induced spin-liquid ground states starting from a Fermi-Hubbard model, realizable in cold atom lattices or some van der Waals materials[122, 123, 124, 125]. Such a system would be described by a Hamiltonian of the form

$$H = -t \sum_{\langle i,j \rangle} e^{i\theta_{ij}(t)} c^\dagger_{i\sigma} c_{j\sigma} + U \sum_i \hat{n}_{i\uparrow} \hat{n}_{i\downarrow}, \tag{3.10}$$

where the time-dependent Peierls phases $\theta_{ij}(t)$ now couple to electronic creation and annihilation operators $c^\dagger_{i\sigma}/c_{i\sigma}$. Here U is the Hubbard on-site coulomb interaction which is proportional to the number of electrons $\hat{n}_{i\sigma} = c^\dagger_{i\sigma} c_{i\sigma}$ with opposite spins $\sigma = \uparrow, \downarrow$ occupying any given lattice site. A similar approach to the high-frequency approximation can be considered, in the spirit of the Schrieffer-Wolff transformation, where U is treated at the same level as the frequency $\hbar\omega$. The resulting effective Hamiltonian also exhibits a spin chirality with similar dependencies on Bessel functions [122]. Thus, an effective Heisenberg model with topological properties can be obtained, and the manipulation of its topological properties

would proceed in exactly the same manner as I have described along this work. The advantage in this model is that the direct coupling to the spin system provides a much simpler and essentially physically equivalent treatment of the topological spin system, with the main difference being that directly coupling to electrons yields a number of advantages which may prove relevant for physical implementations: Firstly, the coupling factors for magnons α_m and for electronsα_e are related by$\alpha_m/\alpha_e = 10^{-5}$ for a frequency of $\hbar\omega = 1$eV, enabling the ability to obtain similar phenomenology for electric fields 10^5 times smaller. Additionally, the driving frequency can be chosen to be sub-gap, i.e. $\hbar\omega < U$, as well as off-resonant with U/n, where $n \in \mathbb{Z}$. This means the electronic bands will remain at half-filling when driven by the laser field, thus avoiding material damage. A HSM plus a spin chirality term can thus remain a valid description of the model under driving. Finally, electric fields of $E_0 \approx 1 \times 10^7$V/cm can be utilized, which are well within reach of experiments, and allow for $\alpha a_0 > 1$, reaching most of the relevant parameter space for this proposal. It is to be expected that by manipulating the intensity of laser traps, deformed lattices could be realized in this setting, providing a possible mechanism to test the ideas presented in this chapter in a more controlled environment.

Chapter 4

Coexistence of 1D and 2D topology in quasicrystalline spin systems

In Chapter 3, I have described the effect of deformation on 2D lattices, resulting in homogeneous but anisotropic variations of bond lengths across a sample of materials. It may be stretching the definition of disorder to incorporate strain under its umbrella. In this chapter, another step is taken towards examples of "real" disorder by considering the effect of so-called quasi-disorder in topological 1D spin systems. Quasi-disorder amounts to perturbing a periodic crystal lattice also in a periodic fashion, with the key ingredient being that this perturbation is incommensurate with the lattice. The resulting object, with hybrid features of translational order, and disorder, is often called a quasicrystal.

Quasicrystals were once the subject of controversy, but have now been firmly established as intriguing materials that defy the classification of traditional crystals. Indeed, their mathematical description [126] was proposed more than half a century before their actual observation in 1982 and subsequent publication in 1984 [127]. Since then, many forms and realizations of quasicrystals have been reported [128]. One reason for interest is that they evade the classification of usual crystals based on symmetries of their underlying discrete translation groups, but nonetheless are "ordered" in a translational sense [129, 130]. In the present day, it has long been realized that quasicrystals in d-dimensional space can be thought of as crystalline structures living in a higher $d + d'$ dimensional superspace, which are projected down to a physical dimension, and this feature has been utilized to explore the properties of topological quasicrystals.

The method used for the projection can be picked from a variety of approaches, the most common of which may be the so-called "cut and project" method [131, 132] which is at the heart of the most famous quasicrystalline structures, such as the Fibonacci quasicrystal, which can be realized as a projection from a 2D superspace lattice into a 1D chain [133], or the Penrose tiling, which is a two-dimensional slice of a five-dimensional hypercubic superspace lattice [134]. Many different such possibilities include a relevant "twisting" approach, based on coupling and twisting of monolayers of certain materials into vdW

heterostructures, such as twisted-bilayer graphene [135], for which incommensurability has been studied and is argued to be an important feature [136, 137].

As previously discussed, the approach of quasi-disorder is to start with a crystalline structure in the physical space, upon which some periodic potential incommensurate with the lattice is added, allowing the unfolding of the model into a higher superspace description. This "incommensurate potential" method is at the heart of the so-called Aubry-André (AA) models [138, 139].

The fact that quasicrystalline structures, such as AA models, can host non-trivial single-particle as well as many-body topology is one of their most captivating aspects, from both technological and theoretical perspectives. On the theory side, it has been pointed out that the existence of phasonic excitations or degrees of freedom corresponding, for instance, to momenta along synthetic dimensions in superspace can be used to physically realize $d + d'$-dimensional topological invariants in d-dimensional systems [140, 141, 142, 143].

The standard example of this feature is the presence of the two-dimensional (2D) Chern number in a one-dimensional (1D) AA model. Much like the "cut and project" approach, where deformations of the cutting window induce additional mechanical degrees of freedom, shifting an AA potential relative to the lattice also corresponds to a so-called phasonic degree of freedom, and a 2D superspace crystal can be built by interpreting this phason as a momentum coordinate. This occurs because a periodic potential of this kind can be though of as unfolding the model into a series of replicas and generating fictitious hoppings between them. The resulting lattice exists in one dimension higher, and the additional dimension is said to be "synthetic". The periodicity of the potential is mapped to the magnitude of a "magnetic field" applied to the higher dimensional lattice, which induces Peierls phases via the A-B effect when hopping along the synthetic dimension. Thus, the superspace model of the AA model maps to a square lattice hosting integer quantum hall effect (IQHE) physics [144, 145], where transverse conductance is well known to be topologically characterized by the Chern number [146, 147]. Beyond these simple models, the superspace picture and phasonic degrees of freedom have also been used to characterize the many-body topology of quasicrystals [148].

The remarkable feature of quasicrystals worth describing in this work, is that the physical model retains the topological properties of the superspace model. This can be readily verified by analyzing the spectrum and eigenstates of the AA model, which can be seen to clearly exhibit finite energy states localized at the edges. Furthermore, these states are robust to disorder, and are a direct consequence of the topological properties of the presence of a Chern invariant. Despite seeming fairly counter-intuitive, this point has actually been studied experimentally in the context of photonic crystals using waveguide arrays within

dielectric media [140].

Photonic crystals have historically been the most common platform for realizing AA models, however, realizations within spin systems have been proposed using adsorbed hydrogen or deuterium atoms to a twisted bilayer graphene heterostructure, or in the context of cold atom platforms [149]. In the twisted bilayer model, the adsorbed hydrogen atoms couple to a single graphene sheet, resulting in an induced magnetization. The exchange interaction felt between atoms then leads to a spin $S = 1/2$ ferromagnetic HSM in 1D. Coupling a second graphene monolayer to the system and rotating it by a small angle, leads to a long-wavelength Moiré pattern, which can modulate the exchange interaction. Such a setup has been considered by [149], and using a Jordan-Wigner fermions representation for the ferromagnetic excitations, it is proposed to realize an off-diagonal Aubry-André model sometimes called a Harper-Heisenberg chain.

In this chapter a new toy model called the chiral Aubry-André model is proposed, which relies on quasi-disorder and the ensuing superspace to simultaneously host both 1D and 2D topology in a purely 1D physical chain.

4.1 The chiral Aubry-André model

4.1.1 Building blocks of the cAA model

As discussed in Chapter 2, chiral symmetric models such as the SSH model have been shown to host extremely rich topology. What is also interesting is that these also have a propensity for generalization into different topological models via a process of stacking. Chern numbers characteristic of 2D matter can exist in certain chiral quasi-1D models subject to magnetic fields, such as the Creutz-Su-Schrieffer-Heeger (CSSH) models [150], constructed by stacking two SSH chains in a square configuration, and connecting them with diagonal, second nearest neighbor, as well as vertical, nearest neighbor bonds.

Additionally, stacking multiple copies of these SSH chains, repeating the Creutz-ladder pattern in the 2D plane or 3D space has been shown to be an effective method to construct Weyl-semimetals in 2D and 3D [151], and when certain types of interactions are turned on, these systems have even been shown to host topological superconducting properties [152].

This idea of stacking topological models of low dimension into a higher dimensional model is not so dissimilar from the aforementioned superspace description of quasicrystals, and thus the presence of 2D Chern numbers in quasi-1D systems together with the rich landscape of SSH-type chiral symmetric models are suggestive of a question: Is it possible to construct a topological crystalline existing physically in 1D, and via modulating using an AA approach, render it doubly topological? Or in other words, can the AA

modulation of a chiral symmetric model lead to the coexistence of 1D and 2D topology in a model in 1D physical space?

I will show, in the remainder of this chapter, that topological invariants characteristic to different dimensionalities can coexist in a physically and experimentally meaningful in a model I call the chiral Aubry-André model (cAA). This is perhaps the simplest setting for the coexistence of 1D and 2D topology, as it is built from two building blocks: The first is the SSH model [70], described in Chapter 2, which exhibits chiral symmetry and a quantized topological invariant corresponding to the winding number W. To this SSH model, a second building block is added: an off-diagonal Aubry-André (odAA) term

$$\begin{aligned} H_{\text{odAA}}(\delta) = &- \Delta_1 \sum_n \cos\left(2\pi b n - \delta\right) a_n^\dagger b_n + \text{h.c.} \\ &- \Delta_2 \sum_n \cos\left(2\pi b n - \delta\right) b_n^\dagger a_{n+1} + \text{h.c.}, \end{aligned} \tag{4.1}$$

where the parameters Δ_1 and Δ_2 denote the strengths of the modulation in intra-cell and inter-cell hoppings, respectively. The modulation occurs periodically with a period $L = 1/b$. In the 2D superspace TBM, the model is subjected to an external magnetic field inducing Peirels phases via the A-B effect as discussed in Chapter 1, and b plays the role of the magnetic flux threading each unit cell. This structure is illustrated in Fig. 11 (a) and (d).

In any case, both intra-cell and inter-cell hoppings are varied by the cosine term equivalently within each unit cell. In other words, within each unit cell, the hopping modulation is assumed to occur only due to the difference in the strength parameters Δ_1 and Δ_2. The parameter δ represents an overall shift in the hopping modulation, constituting a phasonic degree of freedom. The chiral Aubry-André (cAA) model is defined as $H_{\text{cAA}}(\delta) \equiv H_{\text{SSH}} + H_{\text{odAA}}(\delta)$.

In the simplest cases where the unperturbed model has no special symmetry, the odAA model has been shown to be topologically equivalent to the AA model by using a superspace prescription. Its topology is entirely characterized by the same Chern number C, in the same manner as the traditional AA model, and indeed, equivalence to the Fibonacci quasicrystal has also been established [153]. In the cAA model, however, the presence of chiral symmetry in the original model actually breaks the topological equivalence between AA and odAA models, since the cAA model as a whole is described by a pair (C, W), and an on-site disorder term such as present in the AA model would break this chiral symmetry, rendering W an ill-defined quantity.

The spectral properties of the cAA model exhibit the remarkable complexity expected from a quasicrystal: In the case where the hopping modulation is commensurate with the lattice spacing, with

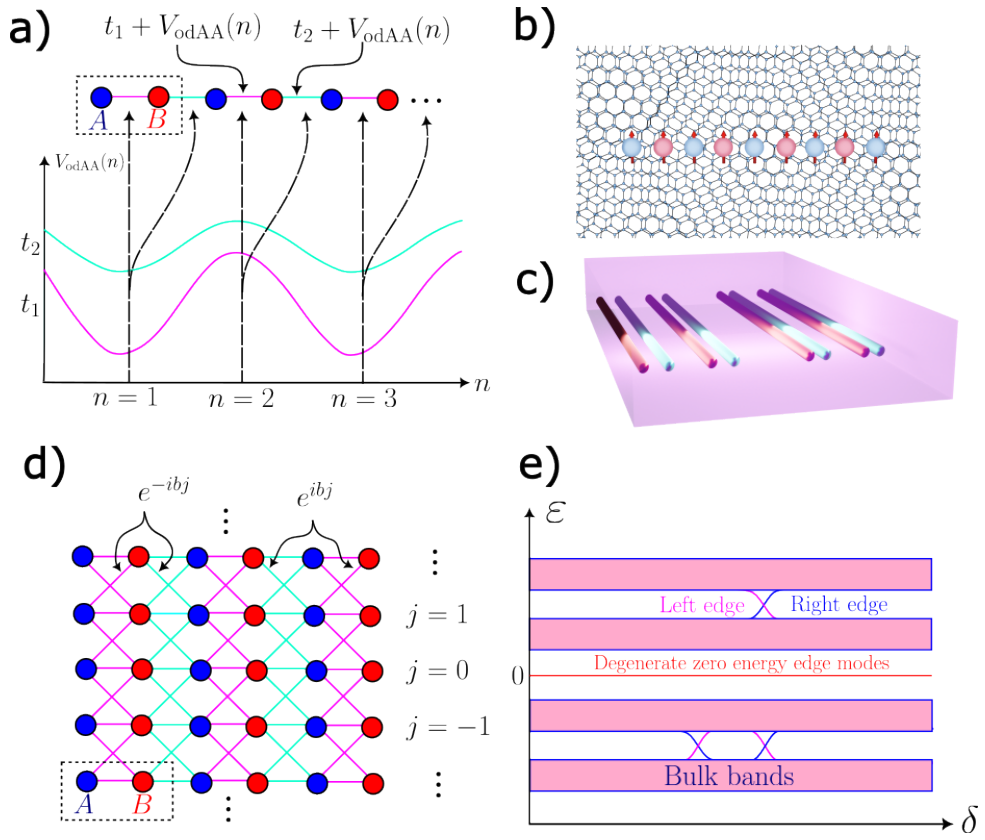

Figure 11: (a) Schematic of the cAA model accompanied by an example plot of the co-sinusoidal hopping amplitude modulation of the underlying SSH model $V_{\text{odAA}}(n)$ as a function of the lattice site. (b) Realization of the cAA model in a solid state platform: Magnetic atoms are adsorbed to a twisted bilayer graphene heterostructure. Each atom becomes magnetized and a $S = 1/2$ Heisenberg model can be used to describe an effective ferromagnetic interaction. The twist induces a modulation of exchange integral strengths. (c) Realization of the cAA model in a photonic crystal platform. The physical spacing between adjacent waveguides is tuned to take into account both the SSH and odAA modulations. (d) Illustration of the corresponding model using a synthetic dimension, capturing all possible phasonic shifts of the Aubry-André potential. In (d), the hoppings connecting replicas of the 1D chain are accompanied by Peierls phases $e^{\pm ibj}$, and the inverse periodicity of the modulation b plays the role of an applied magnetic field. (e) Typical example plot for the spectrum of the superspace cAA model with an incommensurate potential. The presence of doubly degenerate zero energy edge modes along with edge states at finite energies point to the main results of this work: the coexistence of 1D and 2D topology in a purely 1D model.

$L = p/q \in \mathbb{Q}$, the spectrum comprises q well-defined bands, and the Brillouin zone becomes, itself, $q-$periodic. However, in the quasicrystalline limit where $L \notin \mathbb{Q}$, the spectrum transforms into a Cantor set, lacking a well-defined band structure, but nevertheless a series of densely arranged states often form so-called quasibands. Fig. 12 depicts both scenarios for a chain with $N = 300$ lattice sites, showcasing the effect of commensurate and incommensurate hopping modulations. The figure also illustrates the presence and location of edge states within the cAA model. These edge states connect between different bands or quasibands as the phasonic degree of freedom is varied. Furthermore, panels (a) and (e) of the figure clearly demonstrates the ability to maintain, activate, or deactivate zero-energy edge states by manipulating the phasonic degree of freedom δ, both when the periodicity of the modulation is commensurate and incommensurate with that of the lattice. One important feature to consider, is that a physical realization of the cAA model comprises a single value of δ.

One should not interpret these figures as physical ribbons of material. Rather, only from the superspace interpretation of the phasonic degree of freedom δ as a momentum along a synthetic direction can one map the 1D chain into a ribbon-like structure with periodic boundary conditions along the synthetic direction. The physically accessible spectrum is, in reality, simply a slice of the ribbon spectrum at a fixed value of δ, such as the one observed in panels (b) and (f) of Fig. 12. This way, a realization of the 2D superspace model actually corresponds to many possible physical realizations of the cAA model, each related to one another by translations in the phason δ.

4.1.2 Vanishing field limit

The relative simplicity of the cAA model results in the possibility of obtaining analytical solutions in the limit of vanishing field (large periodicity for the AA modulation) for the spectrum, and by constructing the superspace description, I will show that a series of interesting features are present, such as the genesis of a variable and tunable number of anisotropic massless Dirac cones, showcasing the fact that the cAA model's superspace description is actually in a topological semimetal phase. The Dirac cones can be fused together by changing the model's parameters, allowing for changes between topological semimetal, topological insulator and trivial insulator phases. The phenomenology and physics of Dirac cones is interesting in its own right, being responsible for the spur of research in many quantum materials such as graphene, which naturally host Dirac Fermions [154], but more interestingly, when it comes to the behavior of Dirac cones in the presence of a magnetic field, it is well known that they induce an unconventional version of the IQHE, resulting in changes to the energy distribution of the Landau levels localized at the edges of the system. In graphene, the presence of two Dirac cones leads to a quantization of conduction at half-integer

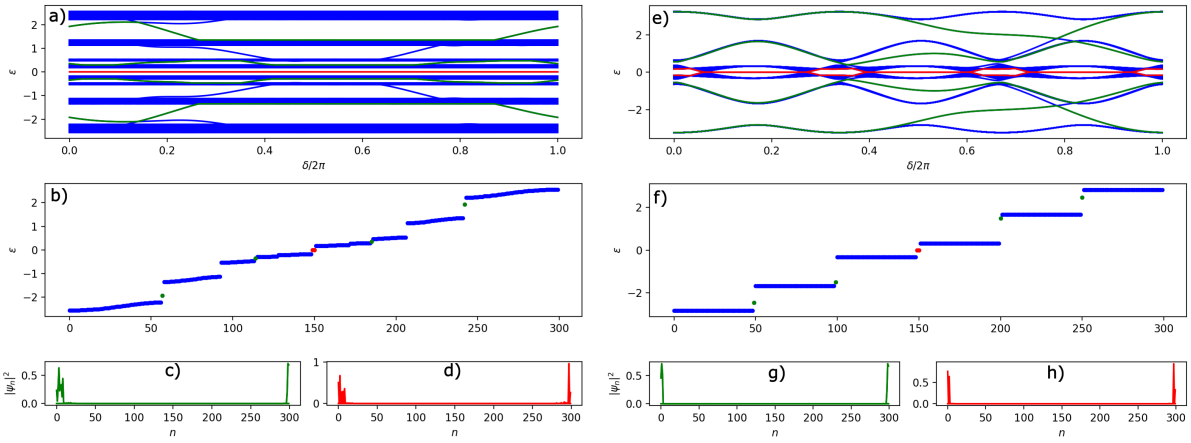

Figure 12: (a) Spectra of the cAA model as a function of the phasonic degree of freedom or modulation shift δ with parameters $t_1 = t_2 = \Delta_1 = 1$ and $\Delta_2 = 0.5$ and a periodicity of $\tau \equiv \left(1+\sqrt{5}\right)/2$. Bulk bands are clearly observed with their position remaining relatively unchanged as δ is varied. A topological insulator phase is verified with persistent topological zero-energy mode across all δ values, as well as in-gap localized edge-states. (b) Spectrum of a physical realization of the cAA model, corresponding to the phasonic parameter $\delta = 0$. The doubly degenerate zero-energy modes are highlighted in red, while the additional visible edge states are marked in green. Not all finite energy edge states are visible for a particular δ. (c)-(d): Wave-functions for the modes highlighted in red and green. (e)- (h) are the same as (a)-(d) for the different choice of parameters $t_1 = t_2 = \Delta_1 = 1$ and $\Delta_2 = 1.5$, and a periodicity of 3 atoms, that is commensurate with the lattice. These parameters are chosen to illustrate the possibility of generating a finite amount of band touching points. Six well-defined bulk bands in this case and six band touching points at zero energy, again, with in-gap finite energy edge states, and similarly, zero energy edge modes, which appear and disappear when band touching nodes are crossed.

values, and for this reason, the effect is often called the half-integer quantum hall effect (HIQHE), and several features of this HIQHE are also observable in the cAA model.

To shed some light on the topological origin of the edge state structure and further spectral properties of the cAA model, as well as set up the necessary tools for the topological analysis of the model, it is worthwhile to analyze the vanishing field limit, which corresponds in the 1D language, to a large periodicity limit. To order $\mathcal{O}(b)$, the field dependence drops out from the Hamiltonian, however, one can nevertheless consider its extension to a superspace model.

It is worth noting that this approximation must be performed carefully, but it is valid so long as the magnetic field, or periodicity is much larger than the total length of the system L, i.e. this approximation can be preformed, for $b = p/q$, only in the limit $pL \ll q$. The case of an incommensurate periodicity can be recovered trivially by considering successive approximants p/q to the desired value of b. The advantage of this vanishing field treatment is that many of the model's properties can be analytically recovered in this limit, and intuition can be gained and later utilized for the generic case of finite and possibly large fields. For vanishing fields, the Hamiltonian reads, in a real space description

$$\begin{aligned} H_{\text{2D}} = &- \sum_{i,j} t_1 a^\dagger_{i,j} b_{i,j} + \frac{\Delta_1}{2} a^\dagger_{i,j} b_{i,j+1} + \text{h.c.} \\ &- \sum_{i,j} t_1 b^\dagger_{i,j} a_{i+1,j} + \frac{\Delta_2}{2} b^\dagger_{i,j} a_{i+1,j+1} + \text{h.c.}, \end{aligned} \tag{4.2}$$

where I have slightly changed the notation from the variable n indexing physical state sites to the pair (i, j), where j represents the lattice index along the synthetic dimension. Some additional details on this rewriting is provided in Appendix D. The change from n to i is merely a notation convention to place both directions in the same footing. One of the advantages of this limit is that it becomes possible to analyze the case where an infinitely long chain with periodic boundary conditions is present. It becomes possible to construct Brillouin zone parameterized by momenta along the synthetic direction $\delta \in [0, 2\pi[$ and the physical direction $k \in [0, 2\pi[$. Denoting $\boldsymbol{k} = (k, \delta)$ also allows for a representation of the superspace Hamiltonian in the form of a matrix $H_{2D}(\boldsymbol{k})$ as $H_{\text{2D}} = \sum_{\boldsymbol{k}} \Psi^\dagger_{\boldsymbol{k}} H_{2D}(\boldsymbol{k}) \Psi_{\boldsymbol{k}}$, where $\Psi^\dagger_{\boldsymbol{k}} = \left(a^\dagger_{\boldsymbol{k}}, b^\dagger_{\boldsymbol{k}}\right)$, and with $H_{2D}(\boldsymbol{k})$ explicitly given by

$$\begin{aligned} H_{2D}(\boldsymbol{k}) = &- \left[t_1 + \Delta_1 \cos\delta + (t_2 + \Delta_2 \cos\delta) \cos k\right] \sigma_x \\ &- \left[(t_2 + \Delta_2 \cos\delta) \sin k\right] \sigma_y. \end{aligned} \tag{4.3}$$

This shows that the vanishing field Hamiltonian can be realized in the form of a Dirac model, at the cost

of the σ_x and σ_y Pauli matrices, but does not include a σ_z, much like the SSH model discussed in Chapter 2. This is to be expected, once again, due to the presence of chiral symmetry. Indeed, coupling between replicas of the model along j preserves the fact that hopping can occur only between A and B sublattices or vice-versa. If one were to consider an AA type on-site modulation, this would induce couplings among different sites of the A sublattice and of the B sublattice, thus breaking the chiral symmetry of the 1D model. Now, for all quasicrystalline systems, a treatment using synthetic dimensions is possible, however, chiral symmetry makes this model extremely interesting, since the superspace model becomes a semimetal with topological properties.

It is a semimetal since the cAA model can host at most 4 distinct massless Dirac cones in this vanishing field limit, the positions of which are not restricted to any high-symmetry points of the Brillouin zone, but rather can wander around it depending on the parameter space spanned by t_1, t_2, Δ_1 and Δ_2. To show that this is the case, given equation (4.3), it is simple to diagonalize it and find the energy spectrum $\varepsilon(k, \delta)$. Finding the points at which massless Dirac cones occur, then becomes a matter of analytically solving $\varepsilon(k, \delta) = 0$, which yields the solutions

$$\begin{aligned}\delta_D(k) = \pm \arccos\left(\frac{e^{ik}t_1 + t_2}{e^{ik}\Delta_1 + \Delta_2}\right) \cap \mathbb{R} \\ \vee \pm \arccos\left(\frac{t_1 + e^{ik}t_2}{\Delta_1 + e^{ik}\Delta_2}\right) \cap \mathbb{R}.\end{aligned} \tag{4.4}$$

An intersection with the real numbers is made explicit to recall the fact that the $\arccos(z)$ function may have solutions corresponding to complex numbers, however only real solutions are retained, corresponding to real momenta δ. Additionally, near the location of these Dirac cones, the energy dispersion can be extracted analytically. If the momentum variables are expanded radially near $\boldsymbol{K}_D = (k, \delta_D(k))$ as $\boldsymbol{q} = \boldsymbol{K}_D + q\,(\cos\theta, \sin\theta)$ with $q = \sqrt{k^2 + \delta^2}$, then a linearized form of the dispersion can be written. In particular, if one considers the variables

$$\eta_1 = (t_2\Delta_1 - t_1\Delta_2)^2 / (\Delta_1 - \Delta_2)^2, \tag{4.5}$$

$$\eta_2 = (t_2\Delta_1 - t_1\Delta_2)^2 / (\Delta_1 + \Delta_2)^2, \tag{4.6}$$

$$\xi_1 = (t_1 - t_2 + \Delta_1 - \Delta_2)(t_2 - t_1 + \Delta_1 - \Delta_2), \tag{4.7}$$

$$\xi_2 = (\Delta_1 + \Delta_2 - t_1 - t_2)(t_1 + t_2 + \Delta_1 + \Delta_2), \tag{4.8}$$

then the linearized dispersion around the Dirac cones reads

$$\varepsilon_1 = \pm q\sqrt{\eta_1 \cos^2\theta + \xi_1 \sin^2\theta}, \tag{4.9}$$

$$\varepsilon_2 = \pm q\sqrt{\eta_2 \cos^2\theta + \xi_2 \sin^2\theta}. \tag{4.10}$$

Evidently, these expressions hold only when the massless Dirac cones exist, i.e. when there exists a solution to equation (4.4). As can be seen from the previous equations (4.9) and (4.10), these Dirac cones are generically anisotropic since $\eta_i \neq \xi_i$. By probing the parameter space of the model, five possible phases can be identified: Phase (i) corresponds to a semimetal phase with two massless Dirac cones at $k = 0$; Phase (ii) corresponds to a similar semimetal phase with two massless Dirac cones at $k = \pi$; Phase (iii) is an insulating phase, with no massless Dirac cones; Phase (iv) is a semimetallic phase, this time with four massless Dirac cones, two of which are located at $k = 0$ and another two at $k = \pi$. For all phases where Dirac cones are visible, they are arranged symmetrically around $\delta = 0$. Phase transitions between these four phases occur due to merging and subsequent lifting of the Dirac cones as the parameters of the model are tuned. These mergings can occur either at the edge ($\delta = \pm\pi$) or the center $(\delta = 0)$ of the Brillouin zone along δ. The final phase (v) occurs only for very specific choices of the parameters, where at the critical point of a simultaneous fusion of Dirac cones at $k = 0$ and $k = \pi$ a nodal line semimetal phase is observed, with the two bands touching along all values of k and $\delta = 0$.

The wandering, merging and subsequent appearance or and disappearance of massless Dirac cones is illustrated in Fig. 13(f) for a specific choice of parameters. Different phase diagrams can also be drawn by picking three parameters with varying strength relative to a fourth one. For instance, Δ_2/t_1 and t_2/t_1 can be varied independently while choosing a few different fixed values of Δ_1/t_1. For values of $\Delta_1/t_1 = 0, 0.5, 1, 2$, the diagrams in Fig. 13 (a)-(d) are obtained.

Remarkably, the number of pairs of Dirac cones in this model can be shown to be related to the topological properties of the 1D model. To see why this is the case, think of the momentum δ as a tunable parameter, which is likely to be the case for a realistic implementation of the cAA model. If this is so, a massless Dirac cone occurring in the model corresponds to the band gap closing when $\boldsymbol{K}_D = (k, \delta_D(k))$ is approached. For this reason, it becomes very useful to consider a winding number as a function of δ, such that each particular physical implementation of the cAA model has its own $W(\delta)$. Due to the presence of chiral symmetry, the Hamiltonian matrix can be brought into the form

$$H(\boldsymbol{k}) = \begin{bmatrix} 0 & q(\boldsymbol{k}) \\ q^*(\boldsymbol{k}) & 0 \end{bmatrix}, \tag{4.11}$$

and the winding number can be defined as

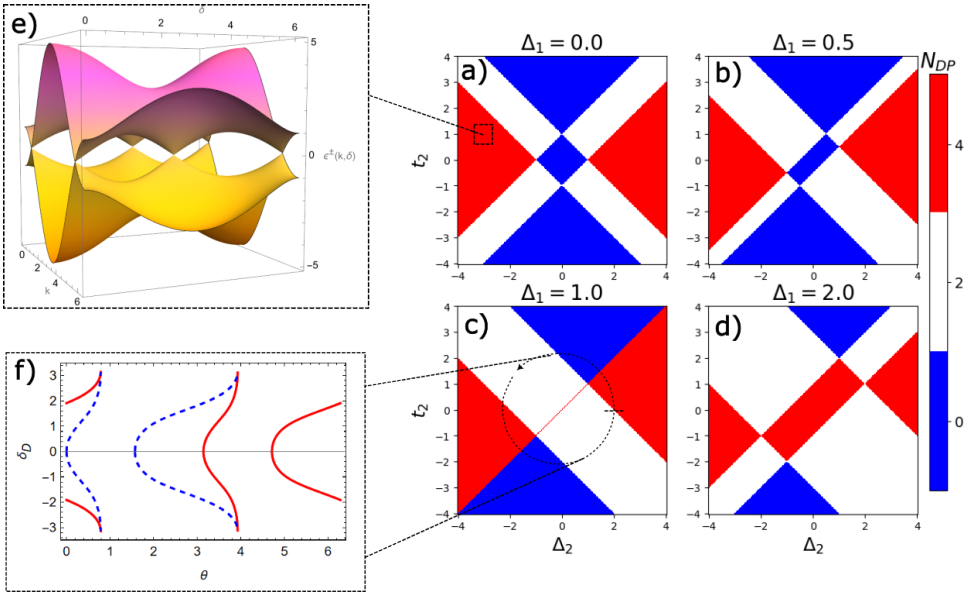

Figure 13: (a)-(d): Phase diagrams for the number of Dirac cones N_{DC} as a function of the models parameters measured relative to t_1. In (c), the line $\Delta_2 = t_2$ corresponds to a situation where the bands touch not only at specific points, but rather along a full line, at $\delta = 0$ and for any value of k, such that the model actually is in a topological nodal line semimetal phase. (e) Band structure of the cAA model showcasing the existence of 4 Dirac cones occurring for the parameters $t_1 = t_2 = 1, \Delta_1 = 0, \Delta_2 = -3$. (f) Trajectories of the Dirac cones for $k = 0$ (continuous line) and $k = \pi$ (dashed line), as a circle is traversed in the parameter space as indicated in (c). Note that each line represents the trajectory of two distinct Dirac cones, one above and one below $\delta_D = 0$ in the plot. The hopping amplitudes are parameterized with $\Delta_2 = 2\cos\theta$ and $t_2 = 2\sin\theta$, and θ is varied from 0 to 2π. Several Dirac cone mergers are observed as θ is varied both at $k = 0$ and $k = \pi$.

$$W(\delta) = \int_0^{2\pi} dk \frac{\partial}{\partial k} \log q(k, \delta). \tag{4.12}$$

The reason one may be interested in such a quantity, besides the fact that it signals the presence or absence of a zero-energy edge mode at each δ is the fact that points at which a transition from $W(\delta) = 1$ to $W(\delta) = 0$ or vice-versa are precisely the points at which massless Dirac cones occur. An analytical computation of the winding number from Equation (4.12), yields

$$W(\delta) = \Theta\left(|t_1 + \Delta_1 \cos\delta| - |t_2 + \Delta_2 \cos\delta|\right), \tag{4.13}$$

as could be anticipated from the topological properties of a standard SSH model as described in Chapter 2. Now, the parity number of pairs of Dirac points, N_{2DP}mod 2, can be counted by looking at whether the Winding number is the same when $\delta = 0$ and when $\delta = \pi$. One considers, in particular, the Winding number at $\delta = 0$, since the Dirac cones always come in pairs, due to the Fermion doubling theorem [155, 156, 157], and furthermore are always located symmetrically around this point. Hence, if the Winding number is the same at $\delta = 0$ and $\delta = \pi$ then it must have changed an even number of times between these two values of δ, leading to an even number of pairs of Dirac points. Otherwise, if it is not the same, it must have changed an odd amount of times, leading to an odd number of pairs of Dirac points. The result is the simple formula

$$N_{2DP} \text{ mod } 2 = |W(\pi) - W(0)|. \tag{4.14}$$

Furthermore, the total number of of Dirac cones N_{DP} in the Brillouin zone can be counted by summing over changes along the entire range of δ. In particular, since the winding number varies as a series of step-functions, taking the derivative along δ will yield a series of Dirac-delta functions. If these delta functions are integrated over, each one contributes with unity, and it becomes possible to count the number of times such changes occur. The result is

$$N_{DP} = \int_0^{2\pi} d\delta \left| \frac{\partial}{\partial \delta} W(\delta) \right|. \tag{4.15}$$

These considerations can also be applied to ribbons of familiar 2D materials such as graphene, and some analogies between the cAA model and Zigzag ribbons of graphene are given in Appendix D, providing an alternative topological description of the emergence of zero energy edge states in these configurations.

For now, in order to demonstrate the practical application of the aforementioned formula (4.15), phase diagrams have been computed for the model, as depicted in Figure 13 (a)-(d). The diagrams clearly indicate

that the count of Dirac cones consistently falls into one of three possibilities: 0, 2, or 4, regardless of the parameter values. Indeed, these diagrams, along with Fig. 13 (f) make it clear that it becomes possible to induce a transition from a state characterized by the presence of an energy band gap to one featuring a gapless state with Dirac cones. The genesis of Dirac cones will have observable effects, even when the system is projected down to physical space, particularly concerning edge states in the 1D physical model when the AA hopping modulation is increased. A detailed exploration of this phenomena is presented in the following section.

4.2 Coexistence of 1D and 2D topology at finite fields in the cAA model

4.2.1 Topological marker approach to quasi-disorder

To study the effects of a magnetic field on the superspace 2D model in more detail, i.e. if one moves away from the limit of slowly varying hopping modulations for the 1D physical system and the quasi-disordered structure becomes relevant, a number of possible approaches present themselves, but none is as clean as the analytic treatment provided in the previous section. The added difficulty stems from the explicit breaking of translational symmetry of the 1D model. The standard toolkit for the IQHE could be applied by analyzing the $L \in \mathbb{Q}$ case and the notion of the magnetic translation group [158], however, a simple analysis of an incommensurate modulation remains, nonetheless analytically out of reach. For this reason, a numerical method is implemented based on recently proposed topological markers for Dirac models and quasicrystals which is capable of handling the problem in full. Two topological markers become relevant for this discussion: The first is a winding number marker and the second is a quasicrystal Chern marker. Since the cAA is a Dirac model, both topological numbers are "different dimensional shadows" of the same invariant known as the wrapping number as pointed out by von Gersdorff and Chen [159], the calculation of which can be performed using a real space approach based on the idea of universal topological markers [93]. Despite this unification, I will make use of this method only to compute the winding number marker. I will rely the method of Chen [93] only for the winding number marker. This approach is based on the construction of a 1D universal topological operator of the form

$$\hat{C}_{1D}(\delta) = N_D \mathcal{W} \left[Q(\delta) \hat{x} P(\delta) + P(\delta) \hat{x} Q(\delta) \right], \tag{4.16}$$

where generically N_D is a normalization factor, here simply unity, and $\mathcal{W}$ is a Pauli matrix which remains unused in the Dirac model Hamiltonian: the σ_z Pauli matrix. P and Q are projectors into occupied and unoccupied states.

$$P = \sum_{E<E_F} |n_E\rangle \langle n_E| , \tag{4.17}$$

$$Q = \mathbb{1} - P. \tag{4.18}$$

For clarity, it is worth making the assumption that the cAA model is fermionic, which on the one hand makes the concept of occupation of bands well defined, and on the other hand, sets the IQHE interpretation of the superspace description on firmer ground, since this effect is often considered to be reserved for fermionic models. Although this is not really the case, with Hofstadter models having been obtained for bosonic systems as well [160], I nevertheless stick to the analysis of fermionic systems for clarity. Furthermore, expected implementations in cold-atom systems or spin-systems rely on Fermions (electrons and Jordan-Wigner fermions respectively). The use of fermions allows for a simple notion of occupation of states, as these will always occupy the lowest energy available states up to the Fermi energy E_F. Finally, in Equation (4.16), $\hat{x}$ is the position operator, which, as stated in Section 4.1, is assumed to have the same eigenvalue for states localized within each of the two sites within the unit cell of the cAA model. The local winding number marker at a given unit cell x of the model is then generically computed as the diagonal matrix element of the topological operator

$$W(x,\delta) = \langle x| \hat{C}_{1D}(\delta) |x\rangle \equiv \sum_{\sigma} \langle x,\sigma| \hat{C}_{1D}(\delta) |x,\sigma\rangle , \tag{4.19}$$

where σ indicates, generically, all internal degrees of freedom of the model. In the BDI case, $\sigma = A, B$ are simply the two sublattice types. The states $|x,\sigma\rangle$ therefore contain the real position of each atom within the unit cell, while $|x\rangle$ states treat both sites as existing in the same position, by summing over $\sigma = A, B$. The use of states $|x\rangle$ and identification of the positions of both sites within each unit cell is crucial here for the computation of the Winding number from the method of Chen. The Hamiltonian $H_{\text{odAA}}(\delta)$ of equation (4.1) is here interpreted merely as a disorder term, and even in the case where the unit cell becomes effectively larger due to the periodicity of modulation, I always retain the summation to be over the two sites corresponding to the unit cells of the unperturbed model. When a finite cAA chain is considered, this winding number marker is expected to coincide with the winding number topological invariant deep in the bulk, and decay near its boundaries. For this reason, due to the presence of spatial disorder and for numerical stability, an averaging over a finite region $\mathcal{R}$ of size $N_{\mathcal{R}}$ deep in the bulk is

performed. Avoiding the edges in the average is crucial due to the decaying behavior of the topological marker. In summary, the winding number invariant can be computed as

$$W(\delta) = \frac{1}{N_{\mathcal{R}}} \mathrm{tr}_{\mathcal{R}} \left(\hat{C}_{1D}(\delta) \right) = \frac{1}{N_{\mathcal{R}}} \sum_{x \in \mathcal{R}} W(x, \delta). \tag{4.20}$$

Note that, in the cAA model, this topological invariant is computed purely from a single slice of the superspace model at a fixed δ corresponding to one particular physical realization of the model. On the other hand, to access the Chern number, the phasonic degree of freedom must come into play, and all slices of fixed δ become relevant. The use of a 2D universal topological marker as proposed by Chen, however, would be unwise, because the cAA model is actually only disordered in the physical 1D space. A 2D universal topological marker is much better suited to the analysis of disordered 2D lattices such as the ones described in Chapter 5. Thus, as an alternative, a recently proposed method originally due to Sykes and Barnett [161] is employed.

This method is particularly suited for handling models like the AA models or other 1D quasicrystals. It's underlying insight is to interpret the phasonic degree of freedom δ as a function of time, $\delta(t) = 2\pi t/T$, which allows one to think of the 1D chain as undergoing an adiabatic and $T-$periodic evolution. This interpretation is made physical in the so-called Thouless pump, which is a quantized pump of charge from one edge of a 1D chain to the other over the course of a period T [162]. The topological pump can be directly observed when a 1D crystal is periodically driven by an external field, and it is topologically protected by the 2D Chern number. By interpreting the phasonic degree of freedom as a quantity which varies in time, regardless of whether it physically is, one can compute the topological pump due to an effective adiabatic Hamiltonian [161], which can be calculated as

$$h(t) = i \left[\frac{\partial P(t)}{\partial t}, P(t) \right], \tag{4.21}$$

This effective Hamiltonian induces an effective adiabatic evolution operator $U(t) = \exp(iht)$, and $P(t) = U^{\dagger}(t) P U(t)$ can be defined as the projector onto occupied states at time t. The local topological quasicrystal marker [161] can, in turn, be defined as the expectation value of a topological operator $\hat{M}_{1Q}(\delta)$, reading

$$\begin{aligned} M_{1Q}(x, \delta) &= \langle x | \, \hat{M}_{1Q}(\delta) \, | x \rangle \\ &\equiv \langle x | \, P(t) U^{\dagger}(t) \hat{x} U(t) P(t) \, | x \rangle \, . \end{aligned} \tag{4.22}$$

Much like in the case of the winding number marker, averaging over a region $\mathcal{R}$ deep in the bulk of the

quasicrystal is necessary, and the trace reads $M_{1Q}(t) = \mathrm{tr}_{\mathcal{R}}\left(\hat{M}_{1Q}(t)\right)/L_{\mathcal{R}}$. This quantity measures the location of the Wannier center at time t. This Wannier center can be thought of as measuring the average location of the eigenstate within each unit cell, and is related to Zak's phase discussed in Chapter 2. It is a central quantity to the modern theory of polarization [61, 163]. The difference in position of the Wannier center at time t_0 and $t_0 + T$ gives the polarization change or charge transfer over the course of a period. This difference is nothing but the 2D Chern number, and hence, setting $t_0 = 0$ for simplicity, at which time $U(0) = \mathbb{1}$, the invariant is defined as [161]

$$C = M_{1Q}(T) - M_{1Q}(0) \tag{4.23}$$

Armed with these two topological invariants, C and $W(\delta)$, and the respective methods of computation in real space, all tools are primed to characterized the topology of the cAA model. Some additional discussion on the topological markers utilized in this and following sections is provided in Appendix E.

4.2.2 Topological invariants C and W

A simple way to illustrate the power of the quasicrystal topological marker is to compute the Chern number for the cAA model as a function of the periodicity and Fermi energy of the model. For each value of b and E_F, $M_{1Q}(0) = \mathrm{tr}_{\mathcal{R}}\left(P(0)\hat{x}P(0)\right)/N_{\mathcal{R}}$ can be immediately computed, and afterwards the time evolved projection operator $P(t)$ can be obtained by slicing the period T into slices of size Δt. Approximating $U(t + \Delta t) \approx \exp\left(-ih(t)\Delta t\right) U(t)$ at each successive interval, one can calculate the Wannier center $M_{1Q}(t) = \mathrm{tr}_{\mathcal{R}}\left(P(t)U^{\dagger}(t)\hat{x}U(t)P(0)\right)/N_{\mathcal{R}}$, and iterating this procedure over one period, C can be calculated using equation (4.23). Computing C for each b and E_F reveals a striking illustration of a colored Hofstadter butterfly [144].

Two examples of these colored Hofstadter butterflies, for topological insulating and topological semimetal phases are provided in Fig. 14. When the 2D superspace model is in a semimetal phase, at charge neutrality $E_F = 0$, there is no trivial topological phase, and the Chern number jumps from $C = 1$ to $C = -1$. This is analogous to the case of the half-integer quantum hall effect (HIQHE) in graphene. On the other hand, when the superspace model is in an insulating phase, at neutrality, there exists a trivial topological phase with $C = 0$. This is analogous to the integer quantum hall effect (IQHE) observed, for instance a square lattice material, where only for a finite Fermi energy does the Chern number become nonzero.

Furthermore, the winding number topological marker clearly counts, for each value δ, the presence or absence of the zero-energy edge mode even when b is a finite quantity. In particular, this allows counting the number of Dirac cones using equation (4.15), in exactly the same manner as utilized for the vanishing

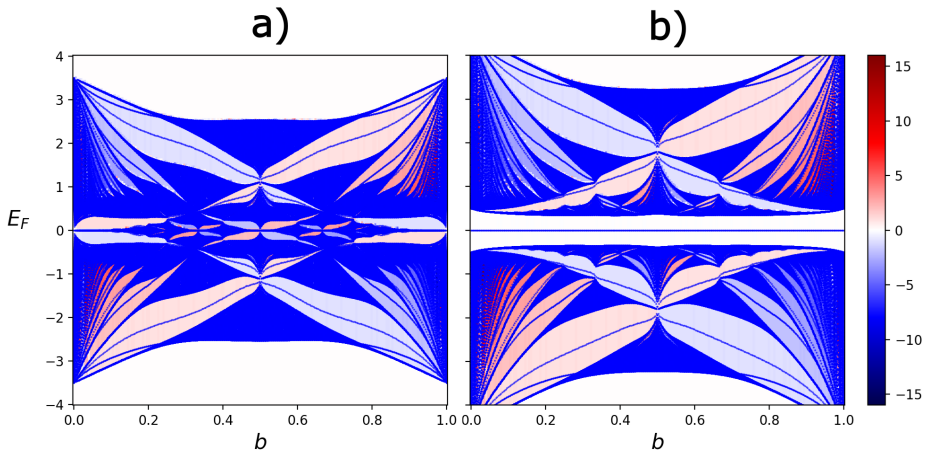

Figure 14: Chern number calculated from the topological marker as a function of the periodicity b and the Fermi Energy E_F. The resulting plots produce a fractal image corresponding to a colored Hofstadter butterfly, where the coloring indicates the value of the Chern number, and the blue lines indicate the energy levels. (a) Semimetal phase, with parameters $t_1 = t_2 = \Delta_1 = 1$ and $\Delta_2 = 1.5$. (b) Insulating phase with $t_1 = t_2 = \Delta_1 = 1$ and $\Delta_2 = 0.5$. The presence of the zero-energy modes in panel (b) is indicative of the presence of non-trivial 1D topology, described by a winding number $W(\delta) = 1$. Although this is not visible in panel (a), these states can also exist at zero energy for the semimetal phase, but they are not present for all values of modulation shift.

field limit.

The limit of incommensurate perturbations, found, for instance, in the case when b approaches the inverse golden ratio $b \to 1/\tau$, can be understood by considering the behavior of successive rational approximants to the incommensurate periodicity. As $b \to 1/\tau$, for example, the number of massless Dirac cones is generically increased, and these nodes become denser in the Brillouin zone. At first, for $1/b = p/q$ the number of Dirac nodes increases as $2q$. As $1/\tau$ is approached, the numerical method for counting these nodes becomes more costly due to a larger sampling of points along δ being necessary to correctly find all transitions of winding number. For finite and rational values $1/b = p/q$ of the field appears to always be given by $0, 2q$ or $4q$ if q is small compared to the chain's size, and this can be observed in Fig. 15 (a)-(d).

For infinite chains, this behavior could continue *ad infininitum*, with the bands turning into perfectly flat and gapless quasibands in the limit of infinite unit cell and system size. However, for a chain of finite size, as q become large, the system's edges also become relevant, leading to a departure from the seemingly observed behavior of the number of $2q$ Dirac nodes, instead stabilizing at some finite value. This is clearly observed in Fig. 15 (e). Let Fib(i) denote the ith Fibonacci number. Comparing the curves which give the number of Dirac cones with the $2q = 2\text{Fib}(i)$, it is clearly seen that this number saturates near the size of the system, i.e. when $2q \sim N$. It begins deviating from the expected behavior slightly earlier, when finite size effects come into play and a few unit cells become comparable with the chain's size.

The topological markers can now be used to explicitly showcase the coexistence of 1D and 2D topology in the cAA model, by computing both invariants for some parameter values. An example calculation is performed in Fig. 16, where phases of type $(C, W) = (0, 1), (\pm 1, 1), (\pm 2, 1), (\pm 3, 1)$ and $(\pm 1, 0)$ are found. As can be clearly seen in this figure, the Chern number counts the number of in-gap edge states for all possible values of δ. Note that even though a Chern number exists and this bulk-boundary correspondence is verified in the superspace model, the number of 1D edge modes which occur within a particular energy gap of a physical realization of the cAA model is not in direct correspondence with this Chern number. The 2D topological invariant merely points to how many edge states can occur at the edge of the chain when the odAA modulation is shifted relative to the lattice.

Finally, intuition about this model can be gained by drawing an analogy to an extremely well understood model, namely as the graphene lattice. By picking a small modulation, for instance $1/b = 1/2001$, and computing the wave-function of edge states for certain values of δ, much like in the case of graphene ribbons with Zigzag edges. The spectrum is immediately reminiscent of the HIQHE, with Dirac cones flattening out at a finite energy. In both settings, the zero-energy edge mode transform into Landau-level

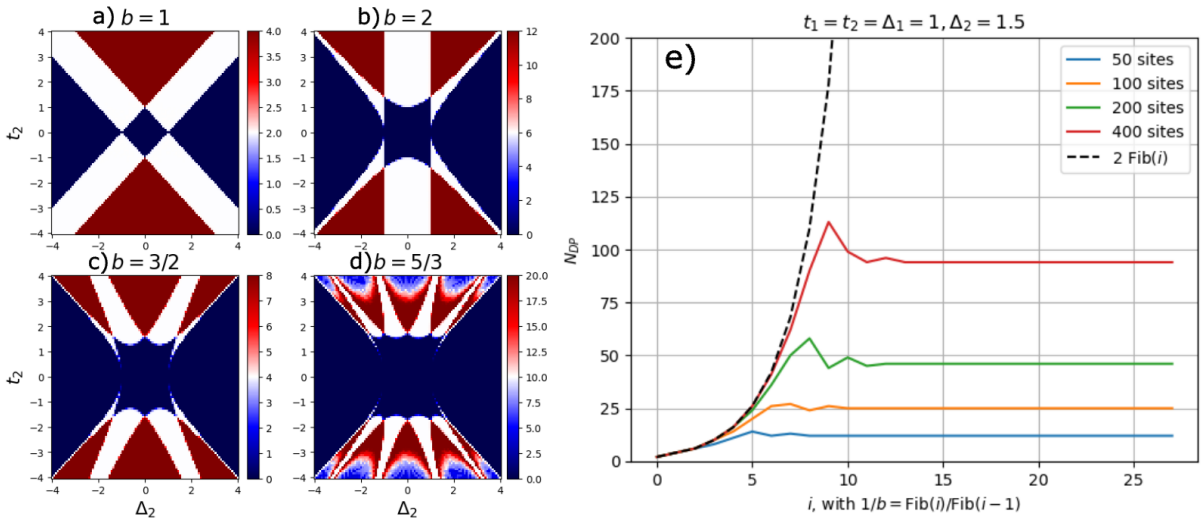

Figure 15: (a)-(d). Number of Dirac nodes calculated from the method relying on the 1D winding number for finite b and fixed $\Delta_1 = 0$. For each of the phase diagrams, successive approximants to the golden ratio $\tau = \left(1 + \sqrt{5}\right)/2$ are utilized as the inverse field. Explicitly, $b = 1, 2, 3/2$ and $5/3$ are used. (e) Growth of the number of nodes as better approximants are utilized. For finite chains, the number of Dirac cones appears to attain a maximum value and then stabilize at a smaller amount. The colored curves correspond to different system sizes. Increasing this size shifts the point at which the number of Dirac nodes stabilizes.

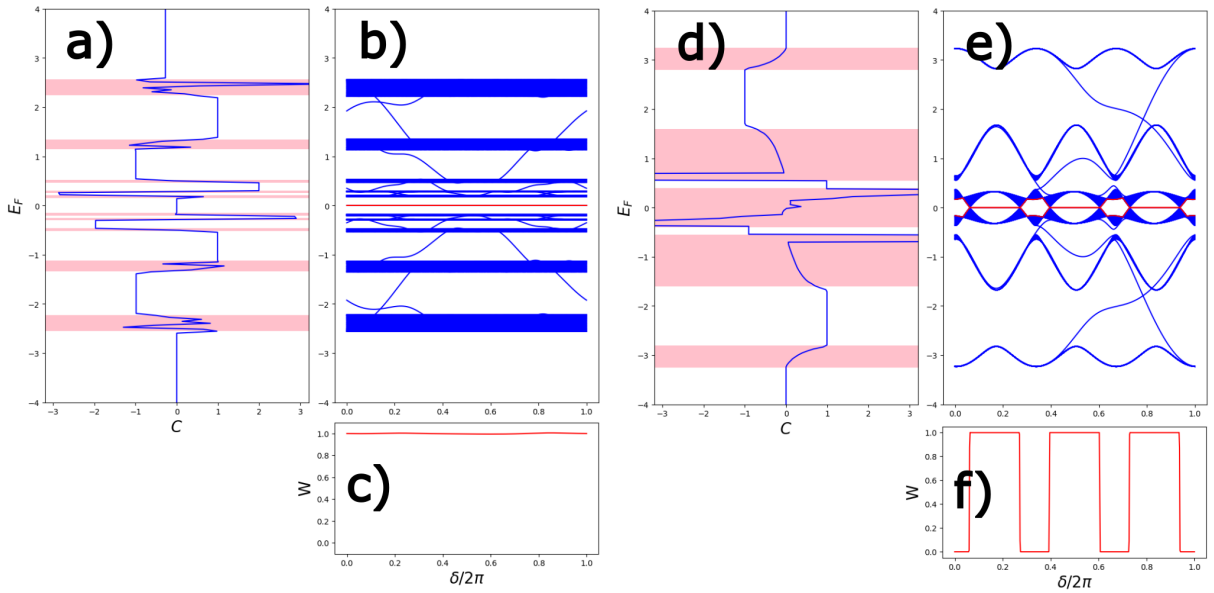

Figure 16: (b) and (e): Energy spectrum for the cAA model with a commensurate $b = 1/3$ and incommensurate $b = 1/\tau$ periodicity, and the same parameters utilized in Fig. 12. (a) and (d): Chern numbers calculated using the topological marker. For both cases, the Chern number correctly predicts the amount of localized edge states which can simultaneous occur in each gap. When it is calculated for a value where energy bands are present, the Chern marker is not quantized, and fluctuates within the areas highlighted in light red. (c) and (f): Winding number calculated using the topological marker. For both cases, the winding number correctly predicts the existence of doubly degenerate edge modes at zero energy. When $W(\delta) = 0$, no such states are present, and the edge modes move into the bulk. Shifting E_F and δ, several phases $(C, W) = (\pm 1, 0), (\pm 1, 1)$ for the $b = 1/3$ and $(C, W) = (\pm 1, 1), (\pm 2, 1), (\pm 3, 1)$ for $b = 1/\tau$.

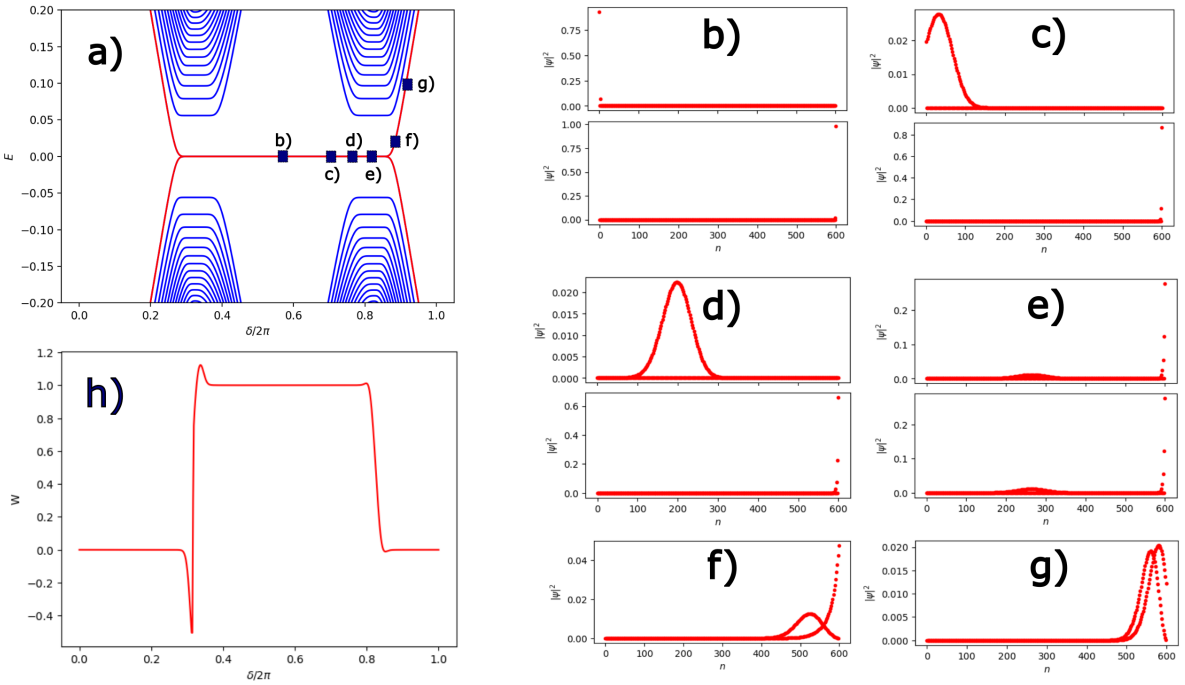

Figure 17: (a) Emergence of Landau levels in the cAA model in a topological semimetal phase with two Dirac cones. The parameters $t_1 = t_2 = \Delta_1 = 1$ and $\Delta_2 = 0.5$ are utilized in a chain cAA chain with 600 atoms, and a periodicity or field $b = 1/2001$. (b)-(g): Evolution of the doubly degenerate edge mode into a pair of non-degenerate Landau level edge state. The chiral symmetry initially ensures that the wave-function has support in a single sublattice. By the time the degeneracy is lifted, the wave-function acquires support in both sublattices but with distinct envelopes. (h) Winding number invariant, matching the presence of doubly degenerate edge modes as a function of the modulation shift δ.

edge states when k passes through the location of a Dirac cone. Additionally, the characteristic square root dispersion of the Landau levels observed in the HIQHE effect of graphene is also present in the cAA model. These similarities are showcased in Fig. 17, together with the useful winding number invariant, which has the value of unity while the model hosts degenerate zero energy modes, and becomes zero after the degeneracy is lifted by shifting the modulation. This analogy goes a bit further, since graphene could be thought of as a particular case of the cAA model. This is discussed in Appendix D.

The coexistence of 1D and 2D topology in the cAA model is perhaps the most fascinating result for this chapter, and quite remarkably, much like other previously studied topological quasi-crystals, an experimentally feasible implementation of the cAA should be possible with currently accessible technologies. Photonic crystals could be used, where the hopping modulation could be achieved by controlling the spacing between distinct fiber optics [140]. In this setting, minimal changes to the way waveguides are spaced are necessary to realize the cAA model. Besides this one, many other alternatives exist, such as quantum

simulators, using, for instance superconducting qubits [164], or other types of quantum computational devices could be used.

Other proposals could include the aforementioned twisted graphene vdW heterostructures with adsorbed hydrogen atoms to realize odAA-type modulations in spin systems. Turning such systems into cAA models could be a case of carefully tuning the adhered atom's positions, or even using twisted trilayer heterostructures, with each additional layer responsible for modulations of different periodicity. One such layer could be responsible for the SSH part of the model, and the other for the odAAH part. Finally, the realization of the cAA model in the context of spin systems could also be implemented in cold-atom trap simulators which have, in the past, been used to simulate and study AA-type models [165, 166].

Chapter 5

Dilution, topology, and future work

Replacing magnetic atoms by other types of either magnetic or non-magnetic atoms is a well known approach for modifying the magnetic properties of a pristine system [167, 168, 169]. When non-magnetic atoms substitute some of the original magnetic atoms, the magnetization diminishes and the spectrum of the magnons is renormalized by the concentration of the nonmagnetic atoms. From a theoretical point of view, the aforementioned substitution is formally equivalent to site dilution. This will be the main concern of this chapter and is the final form of disorder I will cover in this thesis. The primary objective will be to investigate the effects of dilution on the band-structure of a 2D honeycomb ferromagnet with a DMI. To this end, It is an important goal to employ and develop a strategy that addresses the topological properties of dilute spin systems.

The theoretical study of dilution, like any type of disorder, is hindered by the breaking of translational symmetry, which renders the usual condensed-matter techniques of diagonalization in the reciprocal space unusable. Indeed, for a dilute magnetic system the concept of energy bands becomes undefined, due to the breaking of translation symmetry. Due to the added difficulty in the available methods, the study of spin-wave stability and the finding of critical concentrations was the subject of much attention during the 60s and 70s. Systems where a single impurity is present in a Heisenberg ferromagnet were studied first [170, 171], followed by studies of systems with a low impurity concentration [172]. Variational approaches also appeared, which allowed the study of the stability of spin-waves [173, 174]. The first Green's function techniques for the spin-wave theory of dilute ferromagnets were developed by Kaneyoshi [175], and later expanded on by Edwards and Jones [176]. A simplification of the formalism of Edwards and Jones was then developed by Matsubara [177] following the pioneering work of Yonezawa and her development of the coherent potential approximation (CPA) [178, 179]. The Yonezawa-Matsubara CPA provides a method to analyze the type of non-local disorder which emerges in the dilution of Heisenberg ferromagnets in terms of Feynman diagrams. Simpler CPA methods have also been considered in the past, including the so-called single-site CPA, which models disorder as a local potential [180], and single-bond CPA [181, 182, 183,

184], as well as other hybrid approaches [185], which keep the non-local disorder at the level of nearest neighbors. A review of several distinct CPA methods was provided by Elliott *et. al.* [186], and a good summary is presented in a recent paper by Weiss *et. al. [187]*

Somewhat more recent work has been done by Bouzerar and Bruno [188], which combined the CPA with the random phase approximation (RPA), handling finite temperature effects together with dilution, as well as Buczek et. al. [189], which generalized the Yonezawa-Matsubara CPA to the case of composite lattices with more than one atom per unit-cell and to account for substitutional disorder with more than one species of atoms, thus being suitable for the honeycomb lattice of the DMCI.

In previous studies, it has been shown from ab-initio methods that a trivial insulator can become a topological insulator by introducing vacancy-type disorder into the system [190]. In the same vein, and as a gentle introduction into dilute systems, I will show how diluting a lattice to which a 1D FMSSH model is coupled can lead to such a phase transition. For this I will describe a simple numerical approach reliant on topological markers. Here, a future perspective of analyzing the effect of phonon dynamics within the dilute lattice is opened up, and left for future work.

Also using topological markers, a comparison is drawn between the dilute DMCI and the dilute Haldane model, where although the two systems are in direct correspondence in the pristine undiluted case in the thermodynamic limit, removing atoms results in qualitatively different behavior and phase transitions between the two. This numerical approach predicts a topological to trivial phase transition well above the classical percolation threshold, but interestingly, well below the point where the excitation gap is closed. Furthermore, the nature of the transition is unlike the cases studied in previous chapters, as the transition seemingly occurs in a smooth manner, consistently with an intermediate metallic gapless phase.

Finally, I will show that a CPA approach also predicts a transition from a DMCI topological phase to a trivial phase if its honeycomb lattice is diluted. This perturbative self-consistent method predicts that the topological transition occurs at a concentration c_{topo} with a density of states consistent with a gapless phase. This suggests that dilution results in the appearance of in-gap localized states for small amounts of impurities, and only for a much larger critical concentration of non-magnetic atoms does dilution affect topology directly, a phenomenology which is consistent with the numerical topological marker method.

The topological features of the DMCI are computed, for the CPA, following the methods of Wang [191], where an effective topological Hamiltonian is constructed from the Green's function at zero frequency. The topological invariant of the DMCI model can then be extracted from this topological Hamiltonian using, for instance, Fukui's method [192]. The Green's function used in this process can be obtained from any of the methods outlined above, and I will focus on only the simplest: the single-site CPA. Despite the already

interesting phenomenology recovered by the single-site CPA, more sophisticated approaches, such as the diagrammatic Yonezawa-Matsubara CPA are expected to yield much more adequate results. Note that in this final chapter, results are preliminary, but since this was a major focus for research during the development of this thesis, they are included nonetheless. The aim of this chapter is to present the as an introduction to the subject of dilution of 2D topological magnets, as well as discuss some tools and methods relevant for this field.

5.1 Topological marker approach to dilution in 1D and 2D

5.1.1 FMSSH coupled to a dilute non-magnetic lattice

In order to understand how dilution may play a role in the manipulation of topological invariants, I will first showcase a very simplified description of a FMSSH model coupled to a dilute non-magnetic lattice. In 1D, dilution is in principle a fairly trivial phenomena if only NN hoppings are considered. This is because a single dilute site breaks a chain into two chains which don't interact with each other. That is to say, the percolation threshold is immediately reached if a single atom is removed. By coupling a chain to a lattice and focusing on the properties of the chain, one can avoid this problem by considering that only the lattice is diluted. The effects of dilution on the topological properties of a toy quasi-1D model, can then effectively be studied in such a way as to stay above the percolation limit of the chain itself. If an FMSSH model is coupled to a non-magnetic lattice, the simplest way to proceed is to imagine that each magnetic atom in the chain couples to two non-magnetic atoms in the lattice (see Fig. 18 (a)).

The rest of the lattice is ignored for simplicity. Despite its overly simplistic nature, such a toy model has been used in the past to model the coupling between 1D magnons and lattice phonons. Since this section is meant only as a demonstration of the possibility of using dilution to engineer topological properties, phonon dynamics are ignored for now. The quasi-1D toy model is described by the Hamiltonian

$$\begin{aligned} H = &\sum_i \left(J_1 + (\alpha_{i,1} + \beta_{i,1})\, J_1'\right) a_i^\dagger b_i + \text{h.c.} \\ &+ \sum_i \left(J_2 + (\alpha_{i,2} + \beta_{i,2})\, J_2'\right) b_i^\dagger a_{i+1} + \text{h.c.}, \end{aligned} \tag{5.1}$$

where J_1 and J_2 play the role of the usual FMSSH intra- and inter-cell exchange interactions, and where J_1' and J_2' are additional contributions to the exchange mediated by the non-magnetic lattice atoms. Each pair of NN atoms in the FMSSH chain, is coupled to two such atoms in the lattice. These atoms are, for

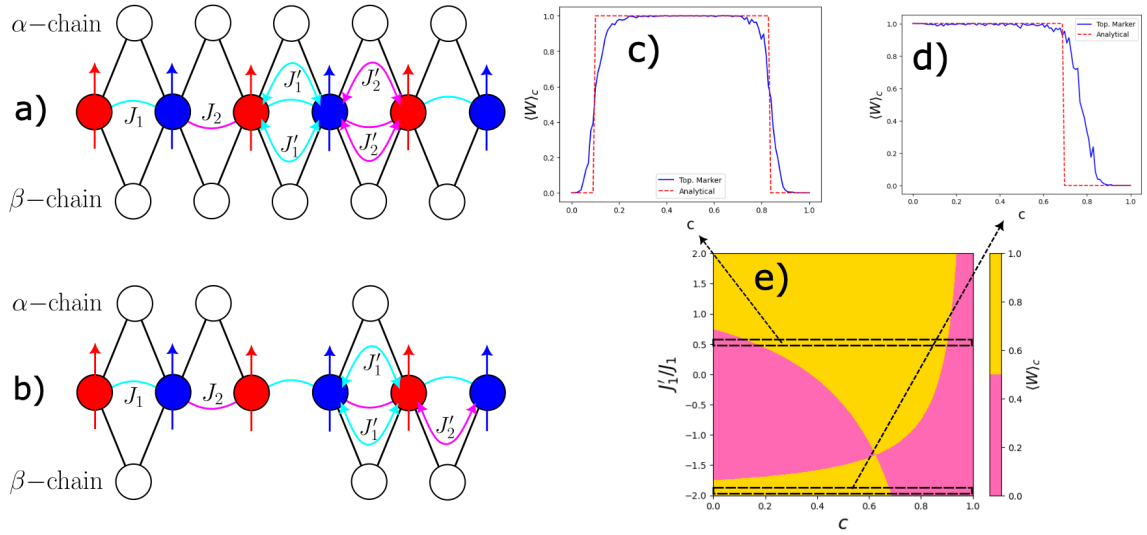

Figure 18: (a) Schematic illustration of the pristine quasi-1D FMSSH model. (b) Dilute version of the model. Red and blue circles with arrows form the magnetic SSH model, while white circles represent non-magnetic lattice atoms coupled to the FMSSH model. Diluting the non-magnetic lattice amounts to randomly removing a certain percentage of lattice atoms, resulting in a change in the effective exchange coupling between magnetic atoms (pink and teal arrows). (c)-(d) Topological marker calculation of the topological invariant (blue line) and analytical calculation of the invariant (dashed red line). (c) Dilution induced Trivial-topological-trivial phase transition using parameters $J_1'/J_1 = 0.5$, $J_2/J_1 = 1.5$, $J_2'/J_1 = -2$ (d) Dilution induced trivial-topological phase transition $J_2/J_1 = 1.5$, $J_2'/J_1 = J_1'/J_1 = -2$. (e) Phase diagram of the quasi-1D dilute FMSSH model for parameters $J_2/J_1 = 1.5$, $J_2'/J_1 = -2$.

simplicity assumed to be arranged in two chains labeled by α and β. The variables $\alpha_{i,1}, \beta_{i,1}$ and $\alpha_{i,2}, \beta_{i,2}$ are random variables which can take the values 0 and 1. These variables play the role of introducing dilution in the model. For instance, if $\alpha_i = 0$, the atom in the $\alpha-$chain connecting the atoms in lattice site i does not contribute with an effective exchange. On the other hand if the atom is not diluted, then $\alpha_i = 1$. For a certain concentration of lattice atoms c, on average $\langle \alpha_{i,1} \rangle_c = \langle \alpha_{i,2} \rangle_c = \langle \beta_{i,1} \rangle_c = \langle \beta_{i,2} \rangle_c = c$. Thus, averaging over the possible dilution configurations for a fixed non-magnetic atom concentration, one can construct a Hamiltonian

$$\begin{aligned} \langle H \rangle_c = &\sum_i \left(J_1 + 2cJ_1'\right) a_i^\dagger b_i + \text{h.c.} \\ &+ \sum_i \left(J_2 + 2cJ_2'\right) b_i^\dagger a_{i+1} + \text{h.c.}, \end{aligned} \tag{5.2}$$

and the topological invariant corresponding to the $\mathbb{Z}$-valued winding number can be computed for the average system as $\langle W \rangle_c = \Theta\left(|J_2 + 2cJ_2'| - |J_1 + 2cJ_1'|\right)$. Thus, it becomes clear that depending on the relative values of J_1, J_2, J_1' and J_2', several interesting phenomena can occur. It is possible to express the Hamiltonian's parameters relative to J_1, or simply fix $J_1 = 1$. Transitions between topological and trivial phases occurs at $|1 + 2c_{\text{topo}} J_1'/J_1| = |J_2/J_1 + 2c_{\text{topo}} J_2'/J_1|$, or solving for the concentration

$$c_{\text{topo}} = \frac{1}{2} \frac{1 \pm J_2/J_1}{J_2'/J_1 \pm J_1'/J_1}. \tag{5.3}$$

Fig. 18 showcases some phase transitions as predicted by this equation. This simple toy model showcases how dilution can be used to tailor topological spin-systems, as reentrant behavior in the winding number is observed, with disorder driven trivial to topological transitions occurring. Nevertheless, the magnetic system is never actually diluted, with this kind of system experiencing it in an indirect "off-diagonal" manner. The direct dilution of a spin system, with magnetic atoms being replaced by non-magnetic ones is discussed in the following section.

5.1.2 Dilute Dirac magnon Chern insulator

The previous section showcased an example of dilution in a quasi-1D model consisting of a FMSSH model coupled to a non-magnetic lattice. Here, I will describe another, perhaps more interesting case of a topological spin system subject to dilution, namely, the dilute DMCI. Such a system will be the focus of the remainder of this chapter. I will now describe how the diluted system is numerically simulated, and using a depth-first search algorithm a dilute sample of finite size is divided into clusters. I will then showcase how

topological markers can be used to compute the Chern invariant for the dilute system, and averaging over configurations I will estimate using this numerical approach, the critical concentration c_{topo} of magnetic atoms, above which the system is in a topological phase, with Chern invariant $C = 1$, and below which the system is in a trivial phase with Chern invariant $C = 0$.

The first step in numerically simulating a dilute honeycomb lattice, is to generate a random set of Boolean variables $\eta_i^{\alpha=A,B} = 0, 1$ in order to account for the dilution. This occurs in the same manner as the quasi-1D FMSSH model described in the previous section, where the Hamiltonian can be written at the cost of such variables. In case a certain atom at site i in sublattice α is non-magnetic or diluted, then $\eta_i^{\alpha} = 0$, killing off the interaction from the Hamiltonian. To model the DMCI, let us consider only NN interactions, and a DMI, such that the dilute Hamiltonian reads

$$\begin{aligned} H = &- J \sum_{\langle i,j \rangle} \eta_i^A \eta_j^B \boldsymbol{S}_i \cdot \boldsymbol{S}_j \\ &- J_{\text{DM}} \sum_{\langle\langle i,j \rangle\rangle} \eta_i^A \eta_j^B \hat{\boldsymbol{z}} \cdot (\boldsymbol{S}_i \times \boldsymbol{S}_j) \,. \end{aligned} \tag{5.4}$$

The model, can, as usual be written in terms of HP operators, yielding a somewhat different expression from the usual Haldane model. In particular, the S_i^z components of the NN FM interaction term yield a on-site energy term which depends on the η_j^{α} variables of its nearest neighbors, and a summation cannot be performed as in the case of the pristine DMCI. The Hamiltonian in real space reads

$$\begin{aligned} H = &- JS \sum_{\langle i,j \rangle} \left(\eta_i^A \eta_j^B a_i^\dagger a_i + \eta_i^B \eta_j^A b_i^\dagger b_i \right) \\ &- JS \sum_{\langle i,j \rangle} \eta_i^A \eta_j^B a_i^\dagger b_j + \text{h.c.} \\ &+ iJ_{\text{DM}} S \sum_{\langle\langle i,j \rangle\rangle} \nu_{ij} \left(\eta_i^A \eta_j^A a_i^\dagger a_j - \eta_i^B \eta_j^B b_i^\dagger b_j \right) + \text{h.c.} \end{aligned} \tag{5.5}$$

To numerically simulate an $N \times N$ lattice, one generates two $N \times N$ Boolean matrices corresponding to the variables η_i^A and η_i^B with the lattice variable $i = (x, y)$ running over the matrix entries. A more challenging aspect of the resulting system is that spin-waves, and for that matter, long-range magnetic order, can only exist only if spin excitations can percolate throughout the lattice. This means that one must find, in the thermodynamic limit $N \to \infty$ a cluster of infinite size of magnetic atoms, held together by NN and NNN bonds. For this reason it is important to divide the $N \times N$ lattice into clusters, and for this a depth-first-search algorithm is employed. The algorithm is as follows:

1. Initialize the two random matrices containing η_i^A and η_i^B with a concentration of values $\eta_i^\alpha = 1$ of c
2. Initialize an empty list of clusters
3. In the list of clusters, initialize an empty cluster
4. Initialize an empty queue or stack of sites to check
5. Add at a certain site to the queue indexed by the position and sublattice (x, y, α)
6. Check if it has been visited or $\eta_i^\alpha = 0$. If either is true, pick another site.
7. If it the site has not yet been visited, and $\eta_i^\alpha = 1$ add it to the cluster, add its NN and NNN sites to the queue, mark it as visited, remove it from the queue and move back to step 6.
8. When the queue is empty once again, check if all sites of the cluster are NN or NNN to sites in another cluster. If so, merge the two clusters. If not, add the cluster to the list of clusters
9. Move back to step 5.
10. Repeat until all sites are visited, and return the list of clusters.

The result from the application of this algorithm is a list of clusters spanning the entire $N \times N$ lattice. These clusters can be counted, and in particular, the cluster of maximum size can be analyzed. The analysis of the topological properties of spin-waves in the dilute lattice is restricted only to this largest cluster, and only concentrations above the percolative threshold are considered.

Of course, since only finite clusters without translation symmetry are considered, reciprocal space methods for computing topological invariants are not suited to the approach presented here, and for this reason, much like in the case of the dilute quasi-1D FMSSH model, topological markers are utilized. As described in the Appendix E, the correct real space topological operator for the DMCI is the Chern marker

$$\hat{C} = 2\pi i \left[Q\hat{x}P\hat{y}Q - P\hat{x}Q\hat{y}P \right]. \tag{5.6}$$

The operators P and Q are obtained from numerically computed eigenstates, using the Python tight-binding package PyBinding [193]. Finally, two averaging procedures are necessary. The first is the usual trace over states deep in the bulk of the system over a region $\mathcal{R}$, yielding $C = \mathrm{tr}_{\mathcal{R}} \left(\hat{C} \right) / N_{\mathcal{R}}$, and additionally, a configurational average is necessary, summing over different configurations of dilution with the same concentration c. Such an average produces the averaged topological invariant $\langle C_{\pm} \rangle_c$, in which

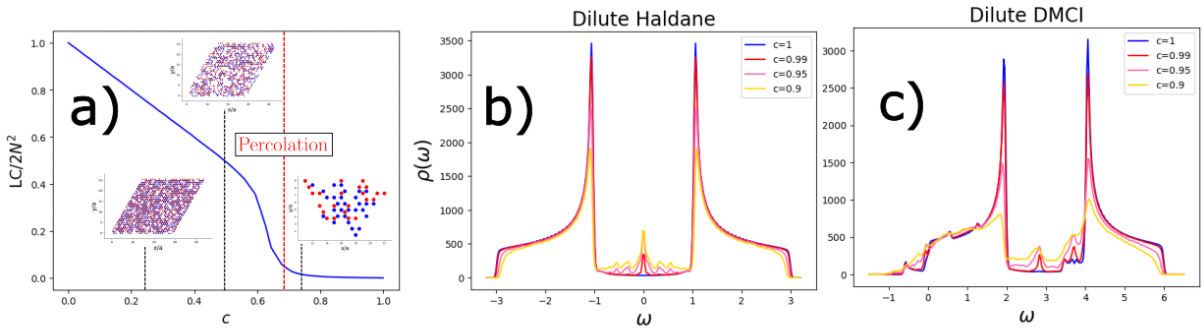

Figure 19: (a) Examples of dilution of the honeycomb lattice. The blue line maps the average number of atoms within the largest cluster LC normalized by the number of atoms in the pristine lattice $2N^2$. A size of $N \times N = 50 \times 50$ is picked, and an average over 100 configurations of vacancy positions is computed. Examples of the largest clusters are given for concentrations of magnetic atoms $c = 0.75, 0.5$ and 0.25. The size of the largest cluster decreases linearly at first, with a sharp drop occurring near the percolation threshold. (b) Density of states of the dilute Haldane model as a function of the dimensionless energy $\omega = \varepsilon/t_1$ normalized over the strength of NN hopping strength. Particle-hole maintained for arbitrary dilution. (c) Density of states of the dilute DMCI. Particle-hole symmetry is broken for finite samples, and this breaking is exacerbated by the presence of dilution.

one can observe a topological phase transition. Other properties can be calculated numerically, and in particular, the density of states (DoS) $\rho(\omega)$ can be obtained using PyBinding. Here, the key difference between a dilute electronic Haldane model and the dilute DMCI becomes very relevant, as the effects of dilution on the DoS is qualitatively different. The differences are illustrated in Fig. 19 (b)-(c). Common to both cases is the smoothing of the van-Hove singularities in teh DoS. In the case of the dilute Haldane model, the DoS is symmetric around zero, spanning from $\omega = \varepsilon/JS = -z$ to $\omega = \varepsilon/JS = z$. In the pristine lattice, $z = 3$, and as dilution is increased, a peak emerges at zero energy, and symmetry around the zero energy is conserved as the peak expands and eventually closes the energy gap. On the other hand, in the DMCI, the DoS is located between $\omega = 0$ and $\omega = 2z$ in the pristine case and in the thermodynamic limit $N \to \infty$. This is because of the on-site energy term which shifts the DoS onto positive energy in the pristine lattice. Even if only the pristine case is analyzed, for a finite lattice, the onsite energy term makes the density of states different between the Haldane model and the DMCI, as in the border of the system, the neighbor count for atoms placed at the edge is reduced, leading to states of negative energy becoming populated. The features should decrease in relevance as $\mathcal{O}(1/N)$ corresponding to the ratio between contribution of sites in the bulk, which is equivalent to that of any site in the thermodynamic limit, and the perimeter, which contributes with lower onsite energies. In any

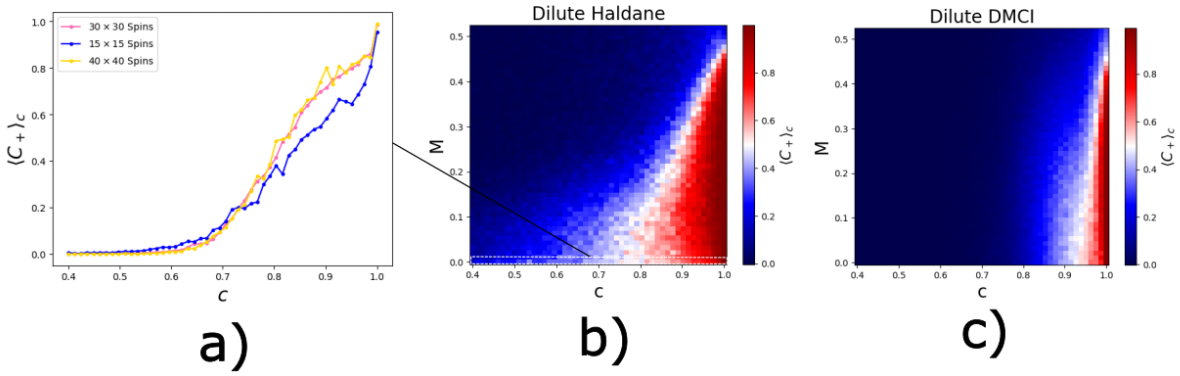

Figure 20: (a) Average Chern number $\langle C_+ \rangle_c$ for the dilute DMCI with Haldane mass $M = (J_A^z - J_B^z)\, S/2$ and several system sizes. (b) Phase diagram as a function of concentration and Haldane mass and magnetic atom concentration c for the Haldane model. (c) Similar phase diagram for the DMCI.

case, these effects break the "particle-hole" symmetry of the DMCI, which is simply the symmetry of the DoS around the middle of the energy spectrum ($\omega = z$ in the pristine case). Furthermore, as dilution is increased and the number of NN spins to each site is reduced, more and more negative energy states are occupied. Of course, this points at an instability of the spin system under dilution, however, to stabilize it, many approaches can be used. A possibility is to apply a magnetic field, shifting the energy spectrum globally to positive energies. Similarly, the use of an anisotropic $J_z > J_{x,y}$ can play the same role, of shifting the DoS such that only positive energy states are occupied.

Unlike in previous discussions, the behavior of the topological invariant is not as direct as one might expect. Indeed, the topological invariant starts with the value $\langle C_\pm \rangle_c = \pm 1$ in the case of the pristine lattice, and also, it reaches the value of $\langle C_\pm \rangle_c = 0$ for a concentration $c \approx 0.7$ in the case of the Haldane model and around $c \approx 0.8$ for the DMCI. However, unlike in previous discussions, it appears to become non-quantized in an intermediate phase, extending since the moment a few impurities are introduced up until the point where the topological invariant becomes zero. For the dilute Haldane model, as the Haldane mass is increased, the transition appears to become sharper, as evident in Fig. 20 (c), however the transition to a trivial phase also occurs for a lower concentration of impurities.

Together with the density of states, which fills the gap for a very small amount of dilution, this points to an intermediate gapless or metallic phase, wherein the topological invariant becomes ill defined. Furthermore, as the system size is increased, the transition becomes sharper around the critical concentration. Note, however, that even when the topological invariant becomes zero, the system is in a gapless phase. To better understand these results, a Green's function based approach is employed in the following section

.

5.2 The Coherent Potential Approximation for topological spin systems

5.2.1 The CPA, and topology from Green's functions

The coherent potential approximation (CPA) is a methodology, or rather, a collection of methodologies, developed to handle substitutional disorder in alloys. It has been successfully applied to many electronic systems and spin systems, and despite missing key features of localization even in its more sophisticated diagrammatic forms, due to several of the usually employed approximations, it proves to be extremely useful when dealing with these kinds of disorder. Dilution of spin systems is, of course, a form of substitutional disorder where magnetic atoms are substituted for vacancies, and thus, the CPA is a useful tool. The CPA is based on the theory of Green's functions (GF), and essentially comprises a self-consistent computation of the GF.

This GF is a tool often used in perturbative calculations to determine properties such as the energy spectrum, density of states, excitation lifetime and many other properties of interacting systems. In this case, only the retarded variant of the GF shall be employed. Consider a DMCI described by the usual Hamiltonian

$$H = -JS \sum_{\langle i,j \rangle} \left(a_j^\dagger b_i + b_i^\dagger a_j - a_i^\dagger a_i - b_j^\dagger b_j \right) + 2J_{DM} Si \sum_{\langle\langle i,j \rangle\rangle} \nu_{ij} \left[a_i a_j^\dagger - b_i b_j^\dagger \right]. \tag{5.7}$$

The (retarded) GFs are defined as

$$G_{ij}^{AA}(t) = -i\Theta(t) \left\langle \left\langle \left[a_i(t), a_j^\dagger(0) \right] \right\rangle \right\rangle, \tag{5.8}$$

$$G_{ij}^{AB}(t) = -i\Theta(t) \left\langle \left\langle \left[a_i(t), b_j^\dagger(0) \right] \right\rangle \right\rangle, \tag{5.9}$$

$$G_{ij}^{BA}(t) = -i\Theta(t) \left\langle \left\langle \left[b_i(t), a_j^\dagger(0) \right] \right\rangle \right\rangle, \tag{5.10}$$

$$G_{ij}^{BB}(t) = -i\Theta(t) \left\langle \left\langle \left[b_i(t), b_j^\dagger(0) \right] \right\rangle \right\rangle, \tag{5.11}$$

where A and B represent the sublattices of honeycomb lattice, i and j run over the lattice sites, and t is a time variable. The interpretation of the GF is that $G_{ij}^{\alpha\beta}(t)$ measures the probability of finding an excitation

in the $\alpha-$sublattice at site i and time t, if an excitation is created at $t = 0$ in the $\beta-$sublattice at site j. In the expressions for the Green's function the double bracket $\langle\langle \dots \rangle\rangle$ signifies an average over the ferromagnetic ground state or a thermal average, in case $T > 0$, to be distinguished from a bracket $\langle \dots \rangle_c$ which denotes the configurational average. This quantity is unknown from the outset if to the Hamiltonian a generic perturbation V is added, and the role of the GF formalism is to provide a way to handle such a perturbation.

Dilution can be simulated in a variety of ways, one of which is by letting a magnetic field of infinite intensity pointing in the $\hat{z}$ direction act in a random configuration of lattice sites. Such a magnetic field freezes the spins at the affected sites in place, and renders propagation of spin-waves through them infinitely costly. Thus, from the point of view of spin-wave dynamics, it is as if the affected sites are non-magnetic or diluted. Let V be understood as playing the role of a magnetic field acting in a single site

$$V = -BSa_0^\dagger a_0, \tag{5.12}$$

In the absence of V, the GF can be computed exactly as described in the Appendix F using an equation of motion approach. Grouping the GFs into the form of a 2×2 matrix with entries corresponding to the different sublattices, for the pristine system, and upon Fourier transforming to the frequency ω, and momentum $\boldsymbol{k}$ domains, one finds

$$\begin{aligned}\left[G_{\boldsymbol{k}}^0(\omega)\right]^{-1} &= \begin{bmatrix} G_{\boldsymbol{k}}^{0AA}(\omega) & G_{\boldsymbol{k}}^{0AB}(\omega) \\ G_{\boldsymbol{k}}^{0BA}(\omega) & G_{\boldsymbol{k}}^{0BB}(\omega) \end{bmatrix}^{-1} \\ &= \begin{bmatrix} \omega - JSz + 2iJ_{DM}Sz\xi(\boldsymbol{k}) & JSz\gamma(\boldsymbol{k}) \\ JSz\gamma^*(\boldsymbol{k}) & \omega - JSz - 2iJ_{DM}Sz\xi(\boldsymbol{k}) \end{bmatrix}. \end{aligned} \tag{5.13}$$

Note here that for simplicity we use a frequency $\omega = \varepsilon/t_1$ corresponding to a dimensionless energy divided by the NN hopping strength. The above equation (5.13) is defined at the cost of the structure factors $\gamma(\boldsymbol{k})$ and $\xi(\boldsymbol{k})$ written as

$$\gamma(\boldsymbol{k}) = \frac{1}{z}\sum_{i=1}^{3} e^{-i\boldsymbol{k}\cdot\boldsymbol{\delta}}, \tag{5.14}$$

$$\xi(\boldsymbol{k}) = \frac{1}{z}\sum_{i=1}^{3} \sin\left(\boldsymbol{k}\cdot\boldsymbol{a}_i\right), \tag{5.15}$$

Taking the perturbation V into account, a similar equation of motion approach can be shown to yield a matrix equation

$$G_0^{-1} G = \mathbb{1} + VG, \tag{5.16}$$

where G_0^{-1} is the pristine GF, and where G is the full unknown GF. This equation is often called the Dyson equation, and the usefulness of GFs stems precisely from the ability to solve this equation perturbatively, and often with recourse to diagrammatic methods. In this work, I will solve the Dyson equation self-consistently by making use of an approach called the single-site CPA. Within this single-site CPA, the GF is determined by imposing the self-consistency condition that in an effective medium material which is averaged over dilution configurations, substituting a single averaged site with an impurity, i.e. acting with V should result in no additional scattering on average. To quantify this, a quantity called the CPA self-energy, Σ_{CPA}, is introduced. Σ_{CPA} is defined in such a way that subtracting it from the unperturbed GF yields the averaged GF

$$\left(G_0^{-1} - \Sigma_{\text{CPA}}\right) = \langle G \rangle_c^{-1} . \tag{5.17}$$

Using this relation, one can write a Dyson equation for the full Green's function, where the configurational average $\langle G \rangle_c$ plays the role of G_0, and where $V - \Sigma_{\text{CPA}}$ plays the role of the perturbation

$$G = \langle G \rangle_c + \langle G \rangle_c \left(V - \Sigma_{\text{CPA}}\right) G. \tag{5.18}$$

To quantify the scattering induced by V, it is usual to define a quantity called the T-matrix, which is defined by the equality

$$\left(V - \Sigma_{\text{CPA}}\right) G = T \langle G \rangle_c . \tag{5.19}$$

It is worth noting that in the CPA, the self-energy $\Sigma_{\text{CPA}} \equiv \Sigma_{\text{CPA}}(\omega)$ is assumed to be only a function of the frequency, and thus diagonal in the momenta. At the cost of the $T-$matrix, the Dyson equation can be rewritten as

$$G = \langle G \rangle_c + \langle G \rangle_c T \langle G \rangle_c , \tag{5.20}$$

and taking the average on both sides yields $\langle G \rangle_c = \langle G \rangle_c + \langle G \rangle_c \langle T \rangle_c \langle G \rangle_c$. From this equation the self-consistency condition reads as $\langle T \rangle_c = 0$. In other words, the average of the scattering produced by replacing a single site with an impurity, is zero. In general, it is customary to assume that two types of atoms ξ and ζ are present, since the CPA is a framework for substitutional disorder. Let these different types be described by T-matrices t_ξ and t_ζ, and let these be subject to generic perturbations V_ζ and

V_ξ such that the self-consistency condition reads $\langle T \rangle_c = (1-c)\langle t_\xi \rangle_c + c\langle t_\zeta \rangle_c = 0$, where ξ is assumed to correspond to magnetic, and ζ to non-magnetic atoms. Explicitly, in momentum space, the self-consistency condition can be written as

$$\langle t_{\xi/\zeta} \rangle = \left[V_{\xi/\zeta} - \Sigma_{\text{CPA}}(\omega)\right] \left(\mathbb{1} - \frac{1}{N}\sum_{\boldsymbol{q}} \langle G_{\boldsymbol{q}}(\omega)\rangle_c \left[V_{\xi/\zeta} - \Sigma_{\text{CPA}}(\omega)\right]\right)^{-1}, \tag{5.21}$$

The dilution limit of the substitutional disorder corresponds to taking $V_\zeta = 0$ and $V_\xi \to \infty$, corresponding to the case of or freezing spins of type ξ, which, again, are the ones assumed to be substituted by non-magnetic atoms. The resulting self-consistency condition can easily be simplified to

$$\Sigma_{\text{CPA}}(\omega) = -(1-c)\left[\frac{1}{N}\sum_{\boldsymbol{q}} \langle G_{\boldsymbol{q}}(\omega)\rangle_c\right]^{-1}. \tag{5.22}$$

Notice, in particular, that the this can be written as an equation where the self-energy depends on itself, and hence why it is called a self-consistent condition

$$\Sigma_{\text{CPA}}(\omega) = -(1-c)\left[\frac{1}{N}\sum_{\boldsymbol{q}} \left(G^{-1}_{0,\boldsymbol{q}}(\omega) - \Sigma_{\text{CPA}}(\omega)\right)^{-1}\right]^{-1}. \tag{5.23}$$

Solution proceeds by providing this equation with an initial guess for the self-energy and computing a new value from this guess. Iterating this procedure until the self-energy converges to a fixed point enables the calculation of the average GF as $\langle G_{\boldsymbol{q}}(\omega)\rangle_c = G^{-1}_{0,\boldsymbol{k}}(\omega) - \Sigma_{\text{CPA}}(\omega)$. As stated, from this GF, most relevant physical quantities relating to the average system can be recovered. Excitation energies correspond to poles of the GF, and the density of states or the topological invariant can be recovered as the imaginary part of the Green's function

$$\rho(\omega) = -\frac{1}{\pi}\sum_{\boldsymbol{q}} \Im\left\langle G_{\boldsymbol{q}}(\omega + i0^+)\right\rangle, \tag{5.24}$$

where $i0^+$ is a small imaginary quantity added to the frequency. The density of states, as predicted from the GF is represented in Fig. 21. Unlike the numerical simulation, as dilution is increased, the CPA does not correctly predict the peak appearing at the center of the energy spectrum, and instead states appear close to the edges of the gap. Nevertheless, the gap becomes closed for a very small impurity concentration, of around $c = 0.95$. Thus, despite the qualitatively different behavior, the gap closing at fairly high concentration of magnetic vacancies is observed in the numerical simulation of the DMCI as well.

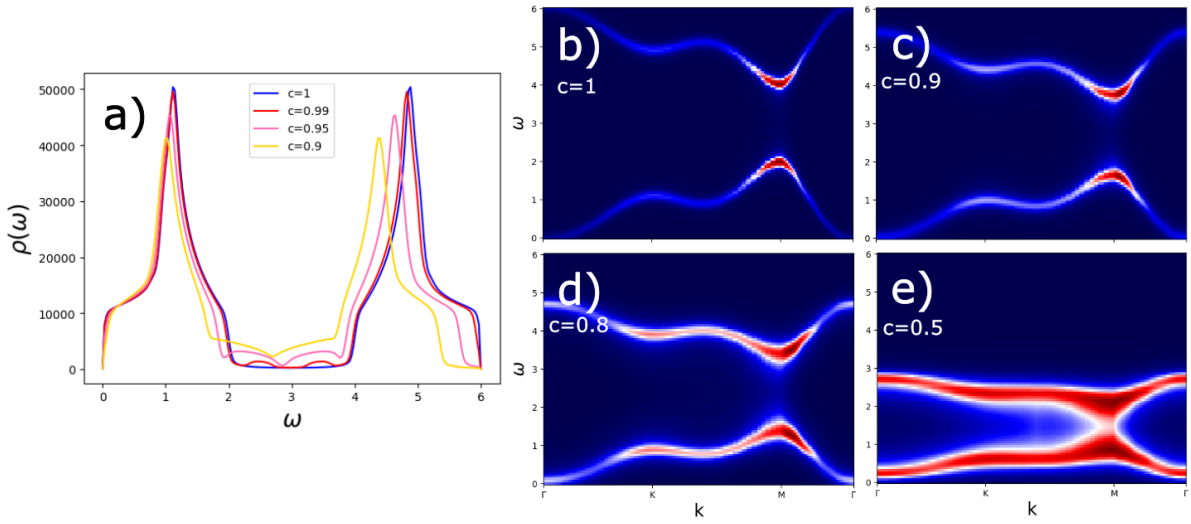

Figure 21: (a) Density of states for the honeycomb lattice for different magnetic atom concentrations within the single-site CPA. As the concentration of magnetic atoms becomes lower, states begin filling the original DMI induced gap, and for very high concentrations $c = 0.9$ the gap is already closed as can be seen in the DoS. (b)-(e) Band structure given by the poles of $\det G_{\boldsymbol{q}}(\omega)$ along the high symmetry points of the BZ: $\boldsymbol{\Gamma} \to \boldsymbol{K} \to \boldsymbol{M} \to \boldsymbol{\Gamma}$.

What remains, is merely the characterization of the band topology of the dilute system within the CPA framework, and perhaps surprisingly, this characterization is also possible using the GF, as topological order in interacting systems has been studied in the past, and methods using the GF have been developed, generalizing the topological invariants to the case of interacting systems [194, 195, 191]. In fact, the method of computing the Chern number from the GF is fairly simple. One often, proceeds by defining an effective topological Hamiltonian for the interacting system.

For models which obey the Dyson equation, this topological Hamiltonian is defined as the inverse of the full GF operator at zero energy, namely

$$H^{\text{topo}}(\boldsymbol{k}) = \left[G^0_{\boldsymbol{k}}(0)\right]^{-1} - \Sigma_{\boldsymbol{k}}(0), \tag{5.25}$$

$$G^{\text{topo}}(\boldsymbol{k}) = \left[\left[G^0_{\boldsymbol{k}}(0)\right]^{-1} - \Sigma_{\boldsymbol{k}}(0)\right]^{-1}. \tag{5.26}$$

Note that both the $G^{\text{topo}}(\boldsymbol{k})$ and its inverse $H^{\text{topo}}(\boldsymbol{k})$ are codified by 2×2 matrices, and indeed, a Dirac matrix representation can be utilized for the Hamiltonian matrix. Using such a topological Hamiltonian matrix, the Chern number can be computed using any standard reciprocal space approach, such as Fukui's method [192]. Employing such an approach within the CPA framework one finds familiar results

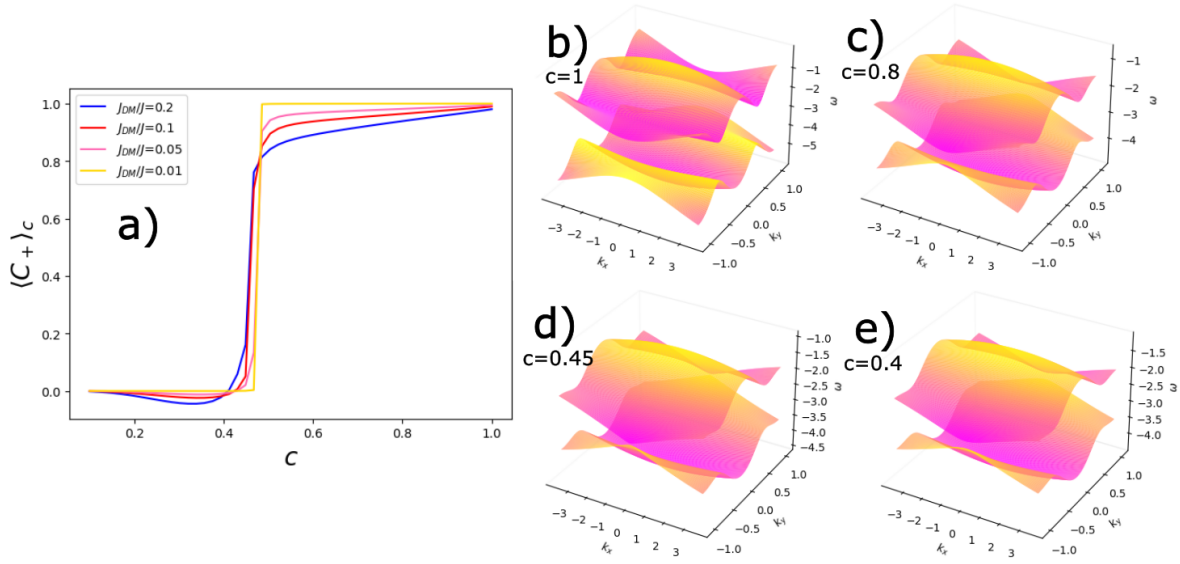

Figure 22: (a) Chern number as a function of concentration of magnetic atoms as computed from the effective topological Hamiltonian in the single-site CPA. (b)-(d) Band structure for the effective topological Hamiltonian $H^{\text{topo}}(\boldsymbol{k})$. The gap of the effective model closes near $c_{\text{topo}} \approx 0.47$ and reopens aafter this critical concentration. Small values of the DMCI J_{DM}/J yield sharper phase transitions .

regarding the topology of the model, when increasing dilution. First, the closing of the DMI induced gap at a very high concentration. This transition does not change the Chern number for the magnon bands from $C_{\pm} = \pm 1$ to a trivial state with $C = 0$ right away, and instead this occurs only for a much lower concentration $c_{\text{topo}} \approx 0.47$. The effective band structure, and topological phase transition, showcased in Fig. 22 seems to mimic the topological marker results and numerically agree with them fairly well, despite a phenomenological disagreement in the way the gap is filled: Unlike the numerical approach, the CPA predicts that the states appear at the edges of the DMI gap, closing it towards the center as the concentration of vacancies is increased, and no peak in the center of the gap is predicted.

Nevertheless, it is quite remarkable that the single-site CPA approach is enough to capture some features of the numerical calculation of the topological invariant, due to its overly simplistic nature. Indeed, many important aspects are missed in this approach. The first is localization. Indeed, throughout this thesis I have not really delved deeply into the theory of localization, even though it is quite relevant in the properties of disordered and quasi-disordered systems. Analyzing the localization properties of the states in the numerical simulation of the dilute DMCI may shed light on the type of transition observed in the topological invariant. Additionally, cluster effects are completely ignored in the single-site CPA framework. Approaches such as that of [188] enable a swift extension of the CPA to a Feynman diagrammatic method,

whereas longer range interactions are considered in the self-consistent expansion. A class of diagrams can be summed analytically to infinite order, and the self-consistent procedure can be carried out as well. Some preliminary results not included here point to the fact that such approaches break the particle-hole symmetry of the model for the square lattice, where the implementation of the diagrammatic methods is much simpler. As observed in both the dilute Haldane and DMCI models, the breaking of particle-hole symmetry is a very salient feature of the process of dilution. For this reason, it may be the case that extending this method to the setting of the honeycomb lattice is a worthwhile pursuit, resulting in better agreement between the phenomenology obtained using the numerical topological marker approach and the semi-analytical CPA. In any case, the agreement between the two methods outlined in this chapter already point to the fact that dilution can be used to manipulate the band-topological properties of magnons in a DMCI, as both predict that dilute ferromagnets become topologically trivial well above the percolation threshold.

Summary of Results

As a conclusion to this thesis, I provide a short summary of the main results presented herein. In general, I showcase throughout this work that spin systems are a rich platform for the realization of band topological models. In particular, I focus on spin-wave or magnon models in 1D or 2D, spurred by the recent discovery of 2D magnetic monolayer van der Waals materials . In 1D, emphasis is given to the SSH model realized by staggered exchange integrals in a chain of magnetic atoms, further specifying to the case of XY ferromagnetic interactions. In 2D, the Haldane model is studied, as realized in the magnonic context via the introduction of a DMI.

In Chapter 3, a synthetic DMI is introduced in a honeycomb lattice via topological phases induced by an electric field, based on pioneering work of Owerre [90, 91]. The main result of the chapter is that the synthetic DMI can be further manipulated using straining [115]. The results are two-fold: If the honeycomb ferromagnet is driven by an electric field and also uniaxially strained, around a magnitude of 15% strain in the Armchair direction, a vanishing electric field is enough to invert the sign of the synthetic topological invariant called the Floquet Chern number; On the other hand, if it is driven by an electric field of around $E_0 \approx 1 \times 10^{13}\mathrm{V/cm}$ vanishing strain amounts can switch the Floquet Chern number. Such a switch results in a revesal of the direction of magnon conduction at the edges, and thus, the latter senario or a middle-ground with smaller electric fields and larger strain could be used to implement an all-strain engingeering approach to topological spintronics and magnonics. This could occur, for instance, by depositing the topological ferromagnet atop a patterned substrate inducing localized strain and implementing topology based devices.

In Chapter 4, I showcased a new toy model which I call the chiral Aubry-André (cAA) model. This is a chiral symmetric quasicrystalline model generated by modulating SSH-type staggered hoppings with a periodicity incomensurate with the lattice. This model simultaneously hosting a 1D and a 2D topological invariant in a purely 1D topological quasicrystal [141, 140, 196]. The former invariant is a 1D winding number owing to the chiral symmetric nature of the cAA model, and the latter is a 2D Chern number, inherited by the superspace description of the quasicrystalline model. This result is the most relevant for

this chapter, with additional results stemming from the topological properties of the model, such as the possibility of counting the number of Dirac cones in the superspace description, and thus characterizing metallic or insulating phases all in terms of the winding number invariant. This enables an understanding and simulation in a 1D platform both the IQHE [77] characteristic of metals, and the HIQHE characteristic of semimetals such as graphene [79]. Such cAA could be realized, for instance, in magnetic chains of adsorbed to twisted graphene heterostructures [149] or in the context of photonic crystals [140].

Finally, in Chapter 5, I presented a study of the effects of dilution on the Chern number of the Dirac magnon Chern insulator, i.e. of the substitution of non-magnetic impurities in I show that when the concentration of non-magnetic impurities is increased, the average Chern number becomes non-quantized, resulting in an intermediate metalic phase before eventually reaching a trivial phase. Differences between dilute Dirac magnon Chern insulators and the dilute Haldane model are highlighted. The transition to a trivial phase occurs well after the topological gap is filled pointing to the metallic nature of this intermediate phase. The numerical approach is compared with a semi-analytical coherent potential approximation (CPA) [179], which provides results compatible with the topological marker approach. This approximate method surprisingly predicts some of the effects of dilution, namely, the gapless nature of the trivial to topological transition. The CPA predicts a sharp transition in the topological invariant, however, at a critical concentration of $c_{\text{topo}} \approx 0.47$. The breaking of particle-hole symmetry is not correctly predicted and the significantly lower numerical value of critical concentration of magnetic atoms predicted by the CPA points to the fact that localization properties are missed, and that a more complete diagrammatic CPA theory [177, 178, 179, 188, 189] could be utilized to build on these results.

Bibliography

[1] D. J. Thouless, M. Kohmoto, M. P. Nightingale, and M. den Nijs. Quantized hall conductance in a two-dimensional periodic potential. *Physical Review Letters*, 49(6):405–408, August 1982.

[2] R. B. Laughlin. Anomalous quantum hall effect: An incompressible quantum fluid with fractionally charged excitations. *Physical Review Letters*, 50(18):1395–1398, May 1983.

[3] B. I. Halperin. Quantized hall conductance, current-carrying edge states, and the existence of extended states in a two-dimensional disordered potential. *Physical Review B*, 25(4):2185–2190, February 1982.

[4] Qian Niu, D. J. Thouless, and Yong-Shi Wu. Quantized hall conductance as a topological invariant. *Physical Review B*, 31(6):3372–3377, March 1985.

[5] F. D. M. Haldane. Model for a quantum hall effect without landau levels: Condensed-matter realization of the "parity anomaly". *Physical Review Letters*, 61(18):2015–2018, October 1988.

[6] Joel E. Moore. The birth of topological insulators. *Nature*, 464(7286):194–198, March 2010.

[7] P. W. Anderson. More is different. *Science*, 177(4047):393–396, August 1972.

[8] A Yu Kitaev. Unpaired majorana fermions in quantum wires. *Physics-Uspekhi*, 44(10S):131–136, October 2001.

[9] C. L. Kane and E. J. Mele. Quantum spin hall effect in graphene. *Physical Review Letters*, 95(22), November 2005.

[10] Ernst Ising. Beitrag zur theorie des ferromagnetismus. *Zeitschrift für Physik*, 31(1):253–258, February 1925.

[11] W. Heisenberg. Zur theorie des ferromagnetismus. *Zeitschrift für Physik*, 49(9-10):619–636, September 1928.

[12] J Vannimenus and G Toulouse. Theory of the frustration effect. II. ising spins on a square lattice. *Journal of Physics C: Solid State Physics*, 10(18):L537–L542, September 1977.

[13] P.W. Anderson. Resonating valence bonds: A new kind of insulator? *Materials Research Bulletin*, 8(2):153–160, February 1973.

[14] Patrick A Lee. Quantum spin liquid: a tale of emergence from frustration. *Journal of Physics: Conference Series*, 529:012001, August 2014.

[15] X. G. Wen, Frank Wilczek, and A. Zee. Chiral spin states and superconductivity. *Physical Review B*, 39(16):11413–11423, June 1989.

[16] Alexei Kitaev. Anyons in an exactly solved model and beyond. *Annals of Physics*, 321(1):2–111, January 2006.

[17] Lucile Savary and Leon Balents. Quantum spin liquids: a review. *Reports on Progress in Physics*, 80(1):016502, November 2016.

[18] Jung Hoon Han. *Skyrmions in Condensed Matter*. Springer International Publishing, 2017.

[19] Ehsan Elahi, Ghulam Dastgeer, Ghazanfar Nazir, Sobia Nisar, Mudasar Bashir, Haroon Akhter Qureshi, Deok kee Kim, Jamal Aziz, Muhammad Aslam, Kashif Hussain, Mohammed A. Assiri, and Muhammad Imran. A review on two-dimensional (2d) magnetic materials and their potential applications in spintronics and spin-caloritronic. *Computational Materials Science*, 213:111670, October 2022.

[20] Igor Žutić, Jaroslav Fabian, and S. Das Sarma. Spintronics: Fundamentals and applications. *Reviews of Modern Physics*, 76(2):323–410, April 2004.

[21] Elliott Lieb, Theodore Schultz, and Daniel Mattis. Two soluble models of an antiferromagnetic chain. *Annals of Physics*, 16(3):407–466, December 1961.

[22] Ian Affleck, Tom Kennedy, Elliott H. Lieb, and Hal Tasaki. Rigorous results on valence-bond ground states in antiferromagnets. *Physical Review Letters*, 59(7):799–802, August 1987.

[23] F. D. M. Haldane. Nonlinear field theory of large-spin heisenberg antiferromagnets: Semiclassically quantized solitons of the one-dimensional easy-axis néel state. *Physical Review Letters*, 50(15):1153–1156, April 1983.

[24] F.D.M. Haldane. Continuum dynamics of the 1-d heisenberg antiferromagnet: Identification with the o(3) nonlinear sigma model. *Physics Letters A*, 93(9):464–468, February 1983.

[25] I Affleck. Quantum spin chains and the haldane gap. *Journal of Physics: Condensed Matter*, 1(19):3047–3072, May 1989.

[26] Jiannis K. Pachos. *Introduction to Topological Quantum Computation*. Cambridge University Press, April 2012.

[27] Chetan Nayak, Steven H. Simon, Ady Stern, Michael Freedman, and Sankar Das Sarma. Non-abelian anyons and topological quantum computation. *Reviews of Modern Physics*, 80(3):1083–1159, September 2008.

[28] J M Kosterlitz and D J Thouless. Ordering, metastability and phase transitions in two-dimensional systems. *Journal of Physics C: Solid State Physics*, 6(7):1181–1203, April 1973.

[29] L. D. Landau. ON THE THEORY OF PHASE TRANSITIONS. In *Collected Papers of L.D. Landau*, pages 193–216. Elsevier, 1965.

[30] Daniel C Mattis. *The Theory of Magnetism Made Simple*. WORLD SCIENTIFIC, March 2006.

[31] Xue Jiang, Qinxi Liu, Jianpei Xing, Nanshu Liu, Yu Guo, Zhifeng Liu, and Jijun Zhao. Recent progress on 2d magnets: Fundamental mechanism, structural design and modification. *Applied Physics Reviews*, 8(3), July 2021.

[32] Yoichiro Nambu. Quasi-particles and gauge invariance in the theory of superconductivity. *Physical Review*, 117(3):648–663, February 1960.

[33] J. Goldstone. Field theories with « superconductor » solutions. *Il Nuovo Cimento*, 19(1):154–164, January 1961.

[34] F. Bloch. Zur theorie des ferromagnetismus. *Zeitschrift für Physik*, 61(3-4):206–219, March 1930.

[35] T. Holstein and H. Primakoff. Field dependence of the intrinsic domain magnetization of a ferromagnet. *Physical Review*, 58(12):1098–1113, December 1940.

[36] N. N. Bogolyubov. On the theory of superfluidity. *J. Phys. (USSR)*, 11:23–32, 1947.

[37] Miguel Kiwi, Tsung han Lin, and L. M. Falicov. Antiferromagnetism, projected density of states, and the bogoliubov transformation for bosons. *Physical Review B*, 25(1):432–435, January 1982.

[38] John Parkinson and Damian J J Farnell. *An Introduction to Quantum Spin Systems*. Springer Berlin Heidelberg, 2010.

[39] Antonio Sergio Teixeira Pires. *Theoretical Tools for Spin Models in Magnetic Systems*. IOP Publishing, April 2021.

[40] R. M. White, M. Sparks, and I. Ortenburger. Diagonalization of the antiferromagnetic magnon-phonon interaction. *Physical Review*, 139(2A):A450–A454, July 1965.

[41] David L. Cortie, Grace L. Causer, Kirrily C. Rule, Helmut Fritzsche, Wolfgang Kreuzpaintner, and Frank Klose. Two-dimensional magnets: Forgotten history and recent progress towards spintronic applications. *Advanced Functional Materials*, 30(18):1901414, May 2019.

[42] N. D. Mermin and H. Wagner. Absence of ferromagnetism or antiferromagnetism in one- or two-dimensional isotropic heisenberg models. *Physical Review Letters*, 17(22):1133–1136, November 1966.

[43] Sidney Coleman. There are no goldstone bosons in two dimensions. *Communications in Mathematical Physics*, 31(4):259–264, December 1973.

[44] Lars Onsager. Crystal statistics. i. a two-dimensional model with an order-disorder transition. *Physical Review*, 65(3-4):117–149, February 1944.

[45] M.E. Lines. Examples of two dimensional ordered magnetic systems. *Physics Letters A*, 24(11):591–592, May 1967.

[46] M. E. Lines. Magnetism in two dimensions. *Journal of Applied Physics*, 40(3):1352–1358, March 1969.

[47] Hans-Joachim Elmers. Ferromagnetc Monolayers. *International Journal of Modern Physics B*, 09(24):3115–3180, October 1995.

[48] Jae-Ung Lee, Sungmin Lee, Ji Hoon Ryoo, Soonmin Kang, Tae Yun Kim, Pilkwang Kim, Cheol-Hwan Park, Je-Geun Park, and Hyeonsik Cheong. Ising-type magnetic ordering in atomically thin $FePS_3$. *Nano Letters*, 16(12):7433–7438, November 2016.

[49] Xingzhi Wang, Kezhao Du, Yu Yang Fredrik Liu, Peng Hu, Jun Zhang, Qing Zhang, Man Hon Samuel Owen, Xin Lu, Chee Kwan Gan, Pinaki Sengupta, Christian Kloc, and Qihua Xiong. Raman spec-

troscopy of atomically thin two-dimensional magnetic iron phosphorus trisulfide ($FePS_3$) crystals. *2D Materials*, 3(3):031009, August 2016.

[50] Dante J. O'Hara, Tiancong Zhu, Amanda H. Trout, Adam S. Ahmed, Yunqiu Kelly Luo, Choong Hee Lee, Mark R. Brenner, Siddharth Rajan, Jay A. Gupta, David W. McComb, and Roland K. Kawakami. Room temperature intrinsic ferromagnetism in epitaxial manganese selenide films in the monolayer limit. *Nano Letters*, 18(5):3125–3131, April 2018.

[51] Yujun Deng, Yijun Yu, Yichen Song, Jingzhao Zhang, Nai Zhou Wang, Zeyuan Sun, Yangfan Yi, Yi Zheng Wu, Shiwei Wu, Junyi Zhu, Jing Wang, Xian Hui Chen, and Yuanbo Zhang. Gate-tunable room-temperature ferromagnetism in two-dimensional fe3gete2. *Nature*, 563(7729):94–99, October 2018.

[52] Cheng Tan, Jinhwan Lee, Soon-Gil Jung, Tuson Park, Sultan Albarakati, James Partridge, Matthew R. Field, Dougal G. McCulloch, Lan Wang, and Changgu Lee. Hard magnetic properties in nanoflake van der waals fe3gete2. *Nature Communications*, 9(1), April 2018.

[53] Cheng Gong, Lin Li, Zhenglu Li, Huiwen Ji, Alex Stern, Yang Xia, Ting Cao, Wei Bao, Chenzhe Wang, Yuan Wang, Z. Q. Qiu, R. J. Cava, Steven G. Louie, Jing Xia, and Xiang Zhang. Discovery of intrinsic ferromagnetism in two-dimensional van der waals crystals. *Nature*, 546(7657):265–269, April 2017.

[54] Bevin Huang, Genevieve Clark, Efrén Navarro-Moratalla, Dahlia R. Klein, Ran Cheng, Kyle L. Seyler, Ding Zhong, Emma Schmidgall, Michael A. McGuire, David H. Cobden, Wang Yao, Di Xiao, Pablo Jarillo-Herrero, and Xiaodong Xu. Layer-dependent ferromagnetism in a van der waals crystal down to the monolayer limit. *Nature*, 546(7657):270–273, June 2017.

[55] A T Costa, D L R Santos, N M R Peres, and J Fernández-Rossier. Topological magnons in CrI_3 monolayers: an itinerant fermion description. *2D Materials*, 7(4):045031, September 2020.

[56] J. Zhou, Q. Wang, Q. Sun, X. S. Chen, Y. Kawazoe, and P. Jena. Ferromagnetism in semihydrogenated graphene sheet. *Nano Letters*, 9(11):3867–3870, August 2009.

[57] Yandong Ma, Ying Dai, Meng Guo, Chengwang Niu, Lin Yu, and Baibiao Huang. Strain-induced magnetic transitions in half-fluorinated single layers of BN, GaN and graphene. *Nanoscale*, 3(5):2301, 2011.

[58] Zhiyong Wang, Chi Tang, Raymond Sachs, Yafis Barlas, and Jing Shi. Proximity-induced ferromagnetism in graphene revealed by the anomalous hall effect. *Physical Review Letters*, 114(1), January 2015.

[59] J. B. S. Mendes, O. Alves Santos, L. M. Meireles, R. G. Lacerda, L. H. Vilela-Leão, F. L. A. Machado, R. L. Rodríguez-Suárez, A. Azevedo, and S. M. Rezende. Spin-current to charge-current conversion and magnetoresistance in a hybrid structure of graphene and yttrium iron garnet. *Physical Review Letters*, 115(22), November 2015.

[60] Michael Victor Berry. Quantal phase factors accompanying adiabatic changes. *Proceedings of the Royal Society of London. A. Mathematical and Physical Sciences*, 392(1802):45–57, March 1984.

[61] David Vanderbilt. *Berry Phases in Electronic Structure Theory*. Cambridge University Press, October 2018.

[62] J Cayssol and J N Fuchs. Topological and geometrical aspects of band theory. *Journal of Physics: Materials*, 4(3):034007, April 2021.

[63] Y. Aharonov and D. Bohm. Significance of Electromagnetic Potentials in the Quantum Theory. *Physical Review*, 115(3):485–491, August 1959.

[64] Y. Aharonov and A. Casher. Topological Quantum Effects for Neutral Particles. *Physical Review Letters*, 53(4):319–321, July 1984.

[65] Miguel Araújo and Pedro Sacramento. *Topology in Condensed Matter*. WORLD SCIENTIFIC, February 2021.

[66] Shinsei Ryu, Andreas P Schnyder, Akira Furusaki, and Andreas W W Ludwig. Topological insulators and superconductors: tenfold way and dimensional hierarchy. *New Journal of Physics*, 12(6):065010, jun 2010.

[67] M.P. do Carmo. *Riemannian Geometry*. Mathematics (Boston, Mass.). Birkhäuser, 1992.

[68] M.P. do Carmo. *Differential Geometry of Curves and Surfaces: Revised and Updated Second Edition*. Dover Books on Mathematics. Dover Publications, 2016.

[69] Shiing-Shen Chern. A simple intrinsic proof of the gauss-bonnet formula for closed riemannian manifolds. *The Annals of Mathematics*, 45(4):747, October 1944.

[70] Wu-Pei Su, J. R. Schrieffer, and Alan J. Heeger. Solitons in polyacetylene. *Physical Review Letters*, 1979.

[71] János K. Asbóth, László Oroszlány, and András Pályi. *A Short Course on Topological Insulators*. Springer International Publishing, 2016.

[72] Alexander Altland and Martin R. Zirnbauer. Nonstandard symmetry classes in mesoscopic normal-superconducting hybrid structures. *Phys. Rev. B*, 55:1142–1161, Jan 1997.

[73] W. Rudin. *Real and Complex Analysis*. Higher Mathematics Series. McGraw-Hill Education, 1987.

[74] Linhu Li, Zhihao Xu, and Shu Chen. Topological phases of generalized su-schrieffer-heeger models. *Physical Review B*, 89(8), February 2014.

[75] Raffaele Resta. Manifestations of berry's phase in molecules and condensed matter. *Journal of Physics: Condensed Matter*, 12(9):R107–R143, February 2000.

[76] B. Andrei Bernevig and Taylor L. Hughes. *Topological Insulators and Topological Superconductors*. Princeton University Press, April 2013.

[77] K. v. Klitzing, G. Dorda, and M. Pepper. New method for high-accuracy determination of the fine-structure constant based on quantized hall resistance. *Physical Review Letters*, 45(6):494–497, August 1980.

[78] A. K. Geim and K. S. Novoselov. The rise of graphene. *Nature Materials*, 6(3):183–191, March 2007.

[79] A. H. Castro Neto, F. Guinea, N. M. R. Peres, K. S. Novoselov, and A. K. Geim. The electronic properties of graphene. *Reviews of Modern Physics*, 81(1):109–162, January 2009.

[80] I. Dzyaloshinsky. A thermodynamic theory of "weak" ferromagnetism of antiferromagnetics. *Journal of Physics and Chemistry of Solids*, 1958.

[81] Tôru Moriya. Anisotropic superexchange interaction and weak ferromagnetism. *Physical Review*, 1960.

[82] Paul A. McClarty. Topological magnons: A review. *Annual Review of Condensed Matter Physics*, 13(1):171–190, March 2022.

[83] A T Costa, D L R Santos, N M R Peres, and J Fernández-Rossier. Topological magnons in cri3 monolayers: an itinerant fermion description. *2D Materials*, 7(4):045031, sep 2020.

[84] Hosho Katsura, Naoto Nagaosa, and Patrick A. Lee. Theory of the Thermal Hall Effect in Quantum Magnets. *Physical Review Letters*, 104(6):066403, February 2010.

[85] Hosho Katsura, Naoto Nagaosa, and Patrick A. Lee. Theory of the thermal hall effect in quantum magnets. *Phys. Rev. Lett.*, 104:066403, Feb 2010.

[86] Y. Onose, T. Ideue, H. Katsura, Y. Shiomi, N. Nagaosa, and Y. Tokura. Observation of the Magnon Hall Effect. *Science*, 329(5989):297–299, July 2010.

[87] Ryo Matsumoto and Shuichi Murakami. Theoretical Prediction of a Rotating Magnon Wave Packet in Ferromagnets. *Physical Review Letters*, 106(19):197202, May 2011.

[88] Ryo Matsumoto, Ryuichi Shindou, and Shuichi Murakami. Thermal Hall effect of magnons in magnets with dipolar interaction. *Physical Review B*, 89(5):054420, February 2014.

[89] Jung Hoon Han and Hyunyong Lee. Spin Chirality and Hall-Like Transport Phenomena of Spin Excitations. *Journal of the Physical Society of Japan*, 86(1):011007, January 2017.

[90] S. A. Owerre. Floquet topological magnons. *Journal of Physics Communications*, 2017.

[91] S. A. Owerre. Corrigendum: Floquet topological magnons (2017 *J. Phys. Commun.* **1** 021002). *Journal of Physics Communications*, 2(10):109501, October 2018.

[92] Peng-Tao Wei, Jin-Yu Ni, Xia-Ming Zheng, Da-Yong Liu, and Liang-Jian Zou. Topological magnons in one-dimensional ferromagnetic su-schrieffer-heeger model with anisotropic interaction. *Journal of Physics: Condensed Matter*, 34(49):495801, October 2022.

[93] Wei Chen. Universal topological marker. *Physical review B*, 2022.

[94] Cheng Gong, Lin Li, Zhenglu Li, Huiwen Ji, Alex Stern, Yang Xia, Ting Cao, Wei Bao, Chenzhe Wang, Yuan Wang, Z. Q. Qiu, R. J. Cava, Steven G. Louie, Jing Xia, and Xiang Zhang. Discovery of intrinsic ferromagnetism in two-dimensional van der Waals crystals. *Nature*, 546(7657):265–269, June 2017.

[95] Bevin Huang, Genevieve Clark, Efrén Navarro-Moratalla, Dahlia R. Klein, Ran Cheng, Kyle L. Seyler, Ding Zhong, Emma Schmidgall, Michael A. McGuire, David H. Cobden, Wang Yao, Di Xiao, Pablo

Jarillo-Herrero, and Xiaodong Xu. Layer-dependent ferromagnetism in a van der Waals crystal down to the monolayer limit. *Nature*, 546(7657):270–273, June 2017.

[96] Lifa Zhang, Jie Ren, Jian-Sheng Wang, and Baowen Li. Topological magnon insulator in insulating ferromagnet. *Physical Review B*, 87(14):144101, April 2013.

[97] Zhengwei Cai, Song Bao, Zhao-Long Gu, Yi-Peng Gao, Zhen Ma, Yanyan Shangguan, Wenda Si, Zhao-Yang Dong, Wei Wang, Yizhang Wu, Dongjing Lin, Jinghui Wang, Kejing Ran, Shichao Li, Devashibhai Adroja, Xiaoxiang Xi, Shun-Li Yu, Xiaoshan Wu, Jian-Xin Li, and Jinsheng Wen. Topological magnon insulator spin excitations in the two-dimensional ferromagnet CrBr 3. *Physical Review B*, 104(2):L020402, July 2021.

[98] R. Chisnell, J.S. Helton, D.E. Freedman, D.K. Singh, R.I. Bewley, D.G. Nocera, and Y.S. Lee. Topological magnon bands in a kagome lattice ferromagnet. *Physical Review Letters*, 115(14):147201, September 2015.

[99] Qing Lin He, Taylor L. Hughes, N. Peter Armitage, Yoshinori Tokura, and Kang L. Wang. Topological spintronics and magnetoelectronics. *Nature Materials*, 21(1):15–23, January 2022.

[100] Zhixiong Li, Yunshan Cao, and Peng Yan. *Topology in Collective Magnetization Dynamics*. 2053-2563. IOP Publishing, 2023.

[101] T. Schneider, A. A. Serga, B. Leven, B. Hillebrands, R. L. Stamps, and M. P. Kostylev. Realization of spin-wave logic gates. *Applied Physics Letters*, 92(2), 01 2008. 022505.

[102] Michael Balynskiy, Howard Chiang, David Gutierrez, Alexander Kozhevnikov, Yuriy Filimonov, and Alexander Khitun. Reversible magnetic logic gates based on spin wave interference. *Journal of Applied Physics*, 123(14), 04 2018. 144501.

[103] L. J. Cornelissen, J. Liu, R. A. Duine, J. Ben Youssef, and B. J. van Wees. Long-distance transport of magnon spin information in a magnetic insulator at room temperature. *Nature Physics*, 11(12):1022–1027, 12 2015.

[104] P. Pirro, T. Brächer, A. V. Chumak, B. Lägel, C. Dubs, O. Surzhenko, P. Görnert, B. Leven, and B. Hillebrands. Spin-wave excitation and propagation in microstructured waveguides of yttrium iron garnet/Pt bilayers. *Applied Physics Letters*, 104(1), 01 2014. 012402.

[105] Chuanpu Liu, Jilei Chen, Tao Liu, Florian Heimbach, Haiming Yu, Yang Xiao, Junfeng Hu, Mengchao Liu, Houchen Chang, Tobias Stueckler, Sa Tu, Youguang Zhang, Yan Zhang, Peng Gao, Zhimin Liao, Dapeng Yu, Ke Xia, Na Lei, Weisheng Zhao, and Mingzhong Wu. Long-distance propagation of short-wavelength spin waves. *Nature Communications*, 9(1):738, February 2018.

[106] X. S. Wang, Ying Su, and X. R. Wang. Topologically protected unidirectional edge spin waves and beam splitter. *Phys. Rev. B*, 95:014435, Jan 2017.

[107] X. S. Wang, H. W. Zhang, and X. R. Wang. Topological magnonics: A paradigm for spin-wave manipulation and device design. *Phys. Rev. Appl.*, 9:024029, Feb 2018.

[108] Zhiwei Peng, Xiaolin Chen, Yulong Fan, David J. Srolovitz, and Dangyuan Lei. Strain engineering of 2D semiconductors and graphene: from strain fields to band-structure tuning and photonic applications. *Light: Science & Applications*, 9(1):190, November 2020.

[109] T. Low, F. Guinea, and M. I. Katsnelson. Gaps tunable by electrostatic gates in strained graphene. *Physical Review B*, 83(19):195436, May 2011.

[110] Vitor M. Pereira, A. H. Castro Neto, and N. M. R. Peres. Tight-binding approach to uniaxial strain in graphene. *Physical Review B*, 80(4):045401, July 2009.

[111] Vitor M. Pereira and A. H. Castro Neto. Strain Engineering of Graphene's Electronic Structure. *Physical Review Letters*, 103(4):046801, July 2009.

[112] Junchuan Zhong, Mingshan Wang, Teng Liu, Yinghe Zhao, Xiang Xu, Shasha Zhou, Junbo Han, Lin Gan, and Tianyou Zhai. Strain-sensitive ferromagnetic two-dimensional Cr2Te3. *Nano Research*, 15(2):1254–1259, February 2022.

[113] Marwa Mannaï and Sonia Haddad. Strain tuned topology in the Haldane and the modified Haldane models. *Journal of Physics: Condensed Matter*, 32(22):225501, May 2020.

[114] O. G. Udalov and I. S. Beloborodov. Strain-dependent Dzyaloshinskii-Moriya interaction in a ferromagnet/heavy-metal bilayer. *Physical Review B*, 102(13):134422, October 2020.

[115] T. V. C. Antão and N. M. R. Peres. Strain engineering of photoinduced topological phases in two-dimensional ferromagnets. *Physical Review B*, 107(23), June 2023.

[116] André Eckardt and Egidijus Anisimovas. High-frequency approximation for periodically driven quantum systems from a Floquet-space perspective. *New Journal of Physics*, 17(9):093039, September 2015.

[117] A. M. León, J. W. González, J. Mejía-López, F. Crasto de Lima, and E Suárez Morell. Strain-induced phase transition in cri3 bilayers. *2D Materials*, 7(3):035008, apr 2020.

[118] Lev Davidovich Landau and Evgenij M. Lifshitz. *Theory of elasticity*. Number 7 in Course of theoretical physics. Elsevier, Butterworth-Heinemann, Amsterdam Heidelberg, 3. engl. ed., rev.ised and enlarged edition, 2009.

[119] Patrice E. A. Turchi, Antonios Gonis, and Luciano Colombo, editors. *Tight-binding approach to computational materials science: symposium held December 1-3, 1997, Boston, Massachusetts, U.S.A.* Materials Research Society symposium proceedings ; v. 491. Materials Research Society, Warrendale, Pa, 1998.

[120] A. H. Castro Neto and Francisco Guinea. Electron-phonon coupling and Raman spectroscopy in graphene. *Physical Review B*, 75(4):045404, January 2007.

[121] Jin Woo Yoon, Yeong Gyu Kim, Il Woo Choi, Jae Hee Sung, Hwang Woon Lee, Seong Ku Lee, and Chang Hee Nam. Realization of laser intensity over 10^{23} W/cm ^{2}. *Optica*, 8(5):630, May 2021.

[122] Emil Vinas Boström, Martin Claassen, James McIver, Gregor Jotzu, Angel Rubio, and Michael Sentef. Light-induced topological magnons in two-dimensional van der Waals magnets. *SciPost Physics*, 9(4):061, October 2020.

[123] Marin Bukov, Michael Kolodrubetz, and Anatoli Polkovnikov. Schrieffer-Wolff Transformation for Periodically Driven Systems: Strongly Correlated Systems with Artificial Gauge Fields. *Physical Review Letters*, 116(12):125301, March 2016.

[124] J. H. Mentink, K. Balzer, and M. Eckstein. Ultrafast and reversible control of the exchange interaction in Mott insulators. *Nature Communications*, 6(1):6708, March 2015.

[125] Martin Claassen, Hong-Chen Jiang, Brian Moritz, and Thomas P. Devereaux. Dynamical time-reversal symmetry breaking and photo-induced chiral spin liquids in frustrated Mott insulators. *Nature Communications*, 8(1):1192, October 2017.

[126] Harald Bohr. Zur theorie der fast periodischen funktionen: I. eine verallgemeinerung der theorie der fourierreihen. *Acta Mathematica*, 45(0):29–127, 1925.

[127] Dan Shechtman, I. Blech, D. Gratias, , and John W. Cahn. Metallic phase with long-range orientational order and no translational symmetry. *Phys. Rev. Lett.I*, 2013.

[128] Enrique Maciá. The role of aperiodic order in science and technology. *Reports on Progress in Physics*, 2006.

[129] P J Steinhardt and S Ostlund. *The Physics of Quasicrystals*. WORLD SCIENTIFIC, December 1987.

[130] M. Senechal. *Quasicrystals and Geometry*. Cambridge University Press, 1996.

[131] Michel Duneau and André Katz. Quasiperiodic patterns. *Physical Review Letters*, 1985.

[132] Veit Elser and Christopher L. Henley. Crystal and quasicrystal structures in al-mn-si alloys. *Physical Review Letters*, 1985.

[133] Anuradha Jagannathan. The fibonacci quasicrystal: Case study of hidden dimensions and multifractality. *Reviews of Modern Physics*, 2021.

[134] N. G. de Bruijn. Algebraic theory of penrose's non-periodic tilings of the plane. ii. *Indagationes Mathematicae (Proceedings)*, 1981.

[135] Pilkyung Moon, Mikito Koshino, and Young-Woo Son. Quasicrystalline electronic states in 30° rotated twisted bilayer graphene. *Phys. Rev. B*, 99:165430, Apr 2019.

[136] Miguel Gonçalves, Bruno Amorim, Flavio Riche, Eduardo V. Castro, and Pedro Ribeiro. Incommensurability enabled quasi-fractal order in 1d narrow-band moiré systems, 2023.

[137] J. A. Crosse and Pilkyung Moon. Quasicrystalline electronic states in twisted bilayers and the effects of interlayer and sublattice symmetries. *Physical Review B*, 103(4), January 2021.

[138] Ang-Kun Wu. Fractal spectrum of the aubry-andre model, 2021.

[139] G.A. Domínguez-Castro and R. Paredes. The aubry-andré model as the hobbyhorse for understanding localization phenomenon. *arXiv: Quantum Gases*, 2018.

[140] Yaacov E. Kraus, Yoav Lahini, Zohar Ringel, Mor Verbin, and Oded Zilberberg. Topological states and adiabatic pumping in quasicrystals. *Bulletin of the American Physical Society*, 2012.

[141] Yaacov E. Kraus, Zohar Ringel, and Oded Zilberberg. Four-dimensional quantum hall effect in a two-dimensional quasicrystal. *Physical Review Letters*, 2013.

[142] Michael Lohse, Christian Schweizer, Hannah M. Price, Oded Zilberberg, and Immanuel Bloch. Exploring 4d quantum hall physics with a 2d topological charge pump. *Nature*, 2018.

[143] Emil Prodan. Virtual topological insulators with real quantized physics. *Physical Review B*, 2015.

[144] Douglas R. Hofstadter. Energy levels and wave functions of bloch electrons in rational and irrational magnetic fields. *Physical Review B*, 1976.

[145] Klaus von Klitzing, G. Dorda, and Michael Pepper. New method for high-accuracy determination of the fine-structure constant based on quantized hall resistance. *Physical Review Letters*, 1980.

[146] Yasuhiro Hatsugai. Chern number and edge states in the integer quantum hall effect. *Physical Review Letters*, 1993.

[147] D. J. Thouless, M. Kohmoto, M. P. Nightingale, and M. den Nijs. Quantized hall conductance in a two-dimensional periodic potential. *Phys. Rev. Lett.*, 49:405–408, Aug 1982.

[148] Dominic V. Else, Sheng-Jie Huang, Abhinav Prem, and Andrey Gromov. Quantum many-body topology of quasicrystals. *Physical Review X*, 2021.

[149] J. L. Lado and Oded Zilberberg. Topological spin excitations in harper-heisenberg spin chains. *Physical Review Research*, 1(3), October 2019.

[150] Juan Zurita, Charles Creffield, and Gloria Platero. Tunable zero modes and quantum interferences in flat-band topological insulators. *Quantum*, 5:591, November 2021.

[151] Sriram Ganeshan and S. Das Sarma. Constructing a weyl semimetal by stacking one-dimensional topological phases. *Physical Review B*, 91(12), March 2015.

[152] Peter Rosenberg and Efstratios Manousakis. Topological superconductivity in a two-dimensional weyl SSH model. *Physical Review B*, 106(5), August 2022.

[153] Yaacov E. Kraus and Oded Zilberberg. Topological equivalence between the fibonacci quasicrystal and the harper model. *Physical Review Letters*, 2012.

[154] A. H. Castro Neto, Francisco Guinea, N. M. R. Peres, Kostya S. Novoselov, and Andre K. Geim. The electronic properties of graphene. *Reviews of Modern Physics*, 2009.

[155] H.B. Nielsen and M. Ninomiya. A no-go theorem for regularizing chiral fermions. *Physics Letters B*, 105(2-3):219–223, October 1981.

[156] H.B. Nielsen and M. Ninomiya. Absence of neutrinos on a lattice. *Nuclear Physics B*, 185(1):20–40, July 1981.

[157] H.B. Nielsen and M. Ninomiya. Absence of neutrinos on a lattice. *Nuclear Physics B*, 193(1):173–194, December 1981.

[158] J. Zak. Magnetic translation group. *Physical Review*, 134(6A):A1602–A1606, June 1964.

[159] Gero von Gersdorff, Shahram Panahiyan, and Wei Chen. Unification of topological invariants in dirac models. *arXiv: Mesoscale and Nanoscale Physics*, 2021.

[160] Yury S Krivosenko, Ivan V Iorsh, and Ivan A Shelykh. Bosonic hofstadter butterflies in synthetic antiferromagnetic patterns. *Journal of Physics: Condensed Matter*, 33(13):135802, January 2021.

[161] Joseph Sykes and Ryan Barnett. 1d quasicrystals and topological markers. *Materials for quantum technology*, 2022.

[162] David J. Thouless. Quantization of particle transport. *Physical Review B*, 1983.

[163] Nicola A. Spaldin. A beginner's guide to the modern theory of polarization. *Journal of Solid State Chemistry*, 2012.

[164] Hao Li, Yong-Yi Wang, Yun-Hao Shi, Kaixuan Huang, Xiaohui Song, Gui-Han Liang, Zheng-Yang Mei, Bozhen Zhou, He Zhang, Jia-Chi Zhang, Shu Chen, S. P. Zhao, Ye Tian, Zhan-Ying Yang, Zhongcheng Xiang, Kai Xu, Dongning Zheng, and Heng Fan. Observation of critical phase transition in a generalized aubry-andŕé-harper model with superconducting circuits. *npj Quantum Information*, 9(1), April 2023.

[165] Kunal K. Das and Jacob Christ. Realizing the harper model with ultracold atoms in a ring lattice. *Phys. Rev. A*, 99:013604, Jan 2019.

[166] Yi Li, Jia-Hui Zhang, Feng Mei, Jie Ma, Liantuan Xiao, and Suotang Jia. Generalized aubry-andré-harper models in optical superlattices. *Chinese Physics Letters*, 39(6):063701, jun 2022.

[167] K. Zhao, Z. Deng, X. C. Wang, W. Han, J. L. Zhu, Xiang Li, Xixia Li, Qiufeng Liu, Qing-Yan Liu, Q. Q. Liu, R. C. Yu, Richeng Yu, Tatsuo Goko, Benjamin A. Frandsen, Lian Liu, Fanlong Ning, Yasutomo J.

Uemura, Hanna Dabkowska, Graeme Luke, Hubertus Luetkens, Elvezio Morenzoni, Sarah Dunsiger, Anatoliy Senyshyn, Peter Böni, and Changqing Jin. New diluted ferromagnetic semiconductor with curie temperature up to 180 k and isostructural to the '122' iron-based superconductors. *Nature Communications*, 2013.

[168] Z. Deng, K. Zhao, Bo Gu, Wen-Peng Han, Wen-Peng Han, W. Han, Wen-Peng Han, J. L. Zhu, X. C. Wang, Xiang Li, Xixia Li, Xiang Li, Xiang Li, Qiufeng Liu, Q. Q. Liu, Qing-Yan Liu, Q. Q. Liu, Richeng Yu, Tatsuo Goko, Benjamin A. Frandsen, Li Liu, Lian Liu, Jinsong Zhang, Yayu Wang, Yayu Wang, Fanlong Ning, Sadamichi Maekawa, Yasutomo J. Uemura, Yohei Uemura, and Changqing Jin. Diluted ferromagnetic semiconductor li(zn,mn)p with decoupled charge and spin doping. *Physical Review B*, 2013.

[169] Tomasz Dietl and Hideo Ohno. Dilute ferromagnetic semiconductors: Physics and spintronic structures. *Reviews of Modern Physics*, 2014.

[170] T. Wolfram, Thomas Wolfram, Thomas Wolfram, T. Wolfram, Joseph Callaway, and Joseph Callaway. Spin-wave impurity states in ferromagnets. *Physical Review*, 1963.

[171] Shozo Takeno. Spin-wave impurity levels in a heisenberg ferromagnet. *Progress of Theoretical Physics*, 1963.

[172] Yu Izyumov. The theory of inelastic scattering of neutrons in ferromagnetic crystals containing impurities. *Proc. Phys. Soc.*, 1966.

[173] G A Murray. Low-energy spin waves for impure heisenberg ferromagnets. *Proc. Phys. Soc.*, 1966.

[174] Deepak Kumar and A. Brooks Harris. Spin-wave excitations and perpendicular susceptibility of a diluted antiferromagnet near percolation threshold. *Physical Review B*, 1985.

[175] Takahito Kaneyoshi. Contribution to the spin-wave theory of a dilute heisenberg ferromagnet. *Progress of Theoretical Physics*, 1969.

[176] Sam F. Edwards and Raymund C. Jones. A green function theory of spin waves in randomly disordered magnetic systems. i. the ferromagnet. *Journal of Physics C: Solid State Physics*, 1971.

[177] Takeo Matsubara. An application of cpa to a random spin system. *Progress of Theoretical Physics Supplement*, 1973.

[178] Fumiko Yonezawa and Kazuo Morigaki. Coherent potential approximation. basic concepts and applications. *Progress of Theoretical Physics Supplement*, 1973.

[179] F Yonezawa, L M Roth, and M Watabe. On the coherent potential approximation for liquid metals. *Journal of Physics F: Metal Physics*, 1975.

[180] G. Rickayzen. *Green's Functions and Condensed Matter*. Dover Publications, 1984.

[181] E-Ni Foo, H. Amar, and Marcel Ausloos. Coherent-potential approximation for alloys with random off-diagonal elements. *Physical Review B*, 1971.

[182] E-Ni Foo and Der-Hsueh Wu. Coherent-potential approximation for disordered ferromagnetic binary alloys. *Physical Review B*, 1972.

[183] E-Ni Foo and Shyamalendu M. Bose. Study of an amorphous ferromagnet by the coherent-potential approximation. *Physical Review B*, 1974.

[184] Takehiko Oguchi, Ikuo Ono, and Takuma Ishikawa. Theory of a disordered heisenberg model by the coherent potential approximation. *Journal of the Physical Society of Japan*, 1973.

[185] A B Harris, P. L. Leath, B G Nickel, and R. J. Elliott. Excitations in the dilute heisenberg ferromagnet using the coherent potential approximation. *Journal of Physics C: Solid State Physics*, 1974.

[186] R. J. Elliott, J. A. Krumhansl, J. A. Krumhansl, and P. L. Leath. The theory and properties of randomly disordered crystals and related physical systems. *Reviews of Modern Physics*, 1974.

[187] Z.J. Weiss and A.R. Massih. Spin-wave theory in a randomly disordered lattice: A heisenberg ferromagnet. *Annals of Physics*, 2022.

[188] G. Bouzerar and P. Bruno. RPA-CPA theory for magnetism in disordered heisenberg binary systems with long-range exchange integrals. *Physical Review B*, 66(1), June 2002.

[189] Paweł Buczek, Leonid M. Sandratskii, Nadine Buczek, Stefan Thomas, Giovanni Vignale, and Arthur Ernst. Magnons in disordered nonstoichiometric low-dimensional magnets. *Physical Review B*, 2016.

[190] Caetano R. Miranda, Felipe Crasto de Lima, and Adalberto Fazzio. At the verge of topology: Vacancy-driven quantum spin hall in trivial insulators. *Nano Letters*, 2021.

[191] Zhong Wang and Shou-Cheng Zhang. Simplified topological invariants for interacting insulators. *Physical Review X*, 2012.

[192] Takahiro Fukui, Yasuhiro Hatsugai, and Hiroshi Suzuki. Chern numbers in discretized brillouin zone: Efficient method of computing (spin) hall conductances. *Journal of the Physical Society of Japan*, 2005.

[193] Dean Moldovan, Miša Andelković, and Francois Peeters. pybinding v0.9.5: a python package for tight-binding calculations, 2020.

[194] Zhong Wang, Xiao-Liang Qi, Xiao-Liang Qi, and Shou-Cheng Zhang. Topological order parameters for interacting topological insulators. *Physical Review Letters*, 2010.

[195] Lei Wang, Xi Dai, and Xincheng Xie. Frequency domain winding number and interaction effect on topological insulators. *Physical Review B*, 2011.

[196] Xiaofeng Fan, Zexiang Shen, Ai Qun Liu, and Jer-Lai Kuo. Band gap opening of graphene by doping small boron nitride domains. *Nanoscale*, 2012.

[197] Takashi Oka and Sota Kitamura. Floquet engineering of quantum materials. *Annual Review of Condensed Matter Physics*, 10(1):387–408, March 2019.

[198] Mark S. Rudner and Netanel H. Lindner. The floquet engineer's handbook, 2020.

[199] Raffaello Bianco and Raffaele Resta. Mapping topological order in coordinate space. *Phys. Rev. B*, 84:241106, Dec 2011.

Part III
Appendices

Appendix A
The algebra of spin operators

The Heisenberg Spin Model (HSM) is introduced in Chapter 1 as the basic model for spin systems. There, I mentioned that it is built by placing a spin $\boldsymbol{S}_i$ at each site of a $d-$dimensional lattice. The spin vector operator is composed of the spin operators along the spin projections along three Cartesian axes $\boldsymbol{S}_i = (S_i^x, S_i^y, S_i^z)$. The square norm of the operator is called the total spin operator and is of the form $S_i^2 = (S_i^x)^2 + (S_i^y)^2 + (S_i^z)^2$. It has eigenvalues $S(S+1)$, where S is an integer or a half odd integer. This eigenvalue is taken to be $S = 1$ for simplicity in most of the main text. As stated in Chapter 1, the simplest interaction between two spins is given by the HSM

$$H_{\text{HSM}} = -\sum_{i,j} J_{ij} \boldsymbol{S}_i \cdot \boldsymbol{S}_j, \tag{A.1}$$

where the sum runs over lattice sites indexed by i and j, and where $J_{ij} = J_{ji}$ is symmetric and called the exchange integral. The algebra of spin operators is described by the commutation relations

$$\left[S_i^\alpha, S_j^\beta\right] = i \sum_\gamma \varepsilon_{\alpha\beta\gamma} \delta_{ij} S_j^\gamma, \tag{A.2}$$

where δ_{ij} is the Kronecker delta, defined by $\delta_{ij} = 1$ if $i = j$ and 0 otherwise, and where $\varepsilon_{\alpha\beta\gamma}$ is the completely anti-symmetric Levi-Civita symbol. Another useful way of writing the HSM is at the cost of the so-called spin ladder operators $S_i^\pm = S_i^x \pm i S_i^y$, using which one may write

$$H_{\text{HSM}} = -\sum_{i,j} J_{ij} \left(S_i^z S_j^z + \frac{1}{2} \left[S_i^+ S_j^- + S_i^- S_j^+ \right] \right). \tag{A.3}$$

For a ferromagnetic (FM) spin-S system, the basis of the Hilbert space associated to each site can be constructed from states $|S, m\rangle$ defined by

$$S_i^2 |S, m\rangle = S(S+1) |S, m\rangle, \tag{A.4}$$

$$S_i^z |S, m\rangle = m |S, m\rangle. \tag{A.5}$$

It is often useful to drop the eigenvalue S from the notation, since S is fixed by construction of the spin-S HSM. For a lattice model with N sites, the total Hilbert space can therefore be spanned by the product states $|\phi\rangle = |m_1\rangle \otimes |m_2\rangle \otimes \cdots \otimes |m_N\rangle$. It is clear that $|\phi\rangle$ is always an eigenstate of $S_i^z S_j^z$, however, it is not an eigenstate of H_{HSM} due to the presence of the spin-ladder operators. To find the effect of $S_i^{\pm}$ on such a state, let us consider

$$\begin{aligned} S_i^z S_i^+ |m_i\rangle &= S_i^z S_i^x |m_i\rangle + i S_i^z S_i^y |m_i\rangle \\ &= \left(S_i^x S_i^z + [S_i^z, S_i^x]\right) |m_i\rangle + i \left(S_i^y S_i^z + [S_i^z, S_i^y]\right) |m_i\rangle \\ &= S_i^x m_i |m_i\rangle + i S_i^y |m_i\rangle + i S_i^y m_i |m_i\rangle + S_i^x |m_i\rangle \\ &= (m_i + 1) S_i^+ |m_i\rangle , \end{aligned} \tag{A.6}$$

where the spin commutation relations (A.2) have been used. Thus, since the state $S_i^+ |m_i\rangle$ has an S_i^z eigenvalue of $(m_i + 1)$, it must be the state $|m_i + 1\rangle$. An analogous proof works to show that $S_i^- |m_i\rangle \propto |m_i - 1\rangle$. The action of the ladder operators is to raise or lower the spin projection eigenvalue along z, labeled by m_i, by one unit. Furthermore, the constant of proportionality between $S_i^{\pm} |m_i\rangle$ and $|m_i \pm 1\rangle$ can easily be found by noting that $S_i^{\pm} S_i^{\mp} = S_i^2 - (S_i^z)^2 \pm S_z$, and comparing this result with the expectation values of $\langle m_i| S_i^{\pm} S_i^{\mp} |m_i\rangle$ by direct usage of the raising and lowering rules. It is simple to show that

$$S_i^{\pm} |m_i\rangle = \sqrt{S(S+1) - m(m \pm 1)}\, |m_i \pm 1\rangle . \tag{A.7}$$

From this simple formula it is clear that $-S < m_i < S$. Chapter 1 drew on this idea to introduce the concept of a magnon as a quasi-particle excitation resulting from acting with S_i^-, on the FM ground state, which using the established limit for m_i can be written as $|\text{FM}\rangle = |S\rangle \otimes |S\rangle \otimes \cdots \otimes |S\rangle$. To show that this is actually the ground state, one can compute the energy associated with a given state amounts to computing the expectation value $E(\phi) = \langle\phi| H_{\text{HSM}} |\phi\rangle$. It is clear that the only term which remains in this average is $E(\phi) = -\sum_{ij} J_{ij} \langle\phi| S_i^z S_j^z |\phi\rangle = -\sum_{ij} J_{ij} m_i m_j$. Due to the restriction $-S < m_i < S$, one finds that $E(\phi) > E(\text{FM}) = -S^2 \sum_{ij} J_{ij}$, and thus $|\text{FM}\rangle$ is the state with the lowest possible energy, i.e. the ground state of the ferromagnet.

Appendix B
Floquet Engineering of Synthetic Hamiltonians

B.1 Floquet Engineering in Condensed matter Physics

Generically, in condensed matter physics, research can be roughly split into two distinct approaches. On one hand, one can have a passive approach, being interested in analyzing, and simulating the complicated Hamiltonians of real materials with rich interacting structures and competing physical phenomena, and on the other hand, one can focus on simplified, effective models which exact analytical solutions and extract from them profound conclusions about the phenomenology and theoretical foundations of interacting matter. It is often the case, however, that in the second case, the simplified Hamiltonians are not available as real materials found in nature. When it is the case that they are available, the models are often celebrated and lead to revolutions. This was, without a doubt, a great contributing factor to the success story of materials such as graphene. In reality, however, these cases are few and far between, and really, condensed matter physicists are now much more interested in actively changing material's properties. This is a more modern "engineering" vision of the physics of solid state, which has lead to a lot of interest in how interactions can be tuned, and how models can be realized using artificial heterostructures, or external means such as magnetic or electric fields. The study of non-equilibrium properties of materials has blossomed in this new panorama, and a variety of methods exist for manipulating such properties. A powerful class of these methods involve light-matter coupling, and a burgeoning field of study particularizes to the manipulation of material properties using time-periodic fields. This is called "Floquet Engineering". Several reviews exist for this theory [197, 116, 198] which I will base appendices B.1-B.3 and C. A Floquet engineered system is described by a T-periodic Hamiltonian

$$H(t) = H(t+T), \tag{B.1}$$

where the periodicity is tied to a driving frequency $T = 2\pi/\hbar\omega$, or photon energy $\hbar\omega$. The core idea of this Floquet approach, is that for a high enough energy, the system can be described by an effective time independent model by "integrating out" the Fourier components of the rapidly varying fields and incorporating them into a new static synthetic Hamiltonian. In essence, the Floquet approach develops a

perturbation theory in the inverse frequency $1/\hbar\omega$, and systematically takes into account corrections to a Hamiltonian stemming from averaged out fields. I will now proceed with a brief description of Floquet theory, and in Appendix C describe how it can be used to synthesize topology in spin systems.

The objective here is to solve the time-dependent Schrodinger equation

$$i\hbar\partial_t \left|\psi_n(t)\right\rangle = H(t) \left|\psi_n(t)\right\rangle, \tag{B.2}$$

for a T-periodic Hamiltonian, and the first guiding principle of the Floquet approach is a familiar one from the theory of crystals. Namely, recall that for Hamiltonians with discrete space-translation symmetry under multiples of some lattice vector $\boldsymbol{R}$, the Bloch theorem assures us that eigenstates can be written in Bloch form as $|\psi(\boldsymbol{r})\rangle = |u(\boldsymbol{r})\rangle\, e^{i\boldsymbol{k}\cdot\boldsymbol{R}}$, with a space periodic part $|u(\boldsymbol{r})\rangle = |u(\boldsymbol{r}+\boldsymbol{R})\rangle$ multiplied by a phase factor which grows linearly with the crystal momentum $\boldsymbol{k}$. In a similar fashion, an analogous theorem exists for discrete time-translation symmetry. This is called the Floquet theorem, which states that an eigenstates of a $T-$periodic Hamiltonian can be written as $|\psi_n(t)\rangle = |u_n(t)\rangle\, e^{-i\varepsilon_n t/\hbar}$, where n is a band index, ε_n is the so-called quasi-energy and$|u_n(t)\rangle$ is a part of the state periodic in time $|u_n(t)\rangle = |u_n(t+T)\rangle$ often called the Floquet mode. In essence, the Floquet theorem allows us to split the time-evolution of a $T-$periodic Hamiltonian into two parts: A fast evolution, or micro-motion, is given by the Floquet mode, and a slow evolution is given by the quasi-energy phase.

Alternatively, this latter interpretation of the Floquet theorem allows us to write the total evolution operator of a Floquet system which obeys equation (B.2) as

$$U(t,t_0) = e^{-iK(t)/\hbar} e^{iH_F(t-t_0)/\hbar} e^{iK(t_0)/\hbar}, \tag{B.3}$$

where $K(t)$ is called the kick operator and obeys $K(t) = K(t+T)$, while H_F is time-independent and is called the Floquet effective Hamiltonian. The quasi-energies correspond to the eigenvalues of H_F, and the Floquet modes $|u_n\rangle$ are the corresponding eigenvalues. The kick operators play the role of the time evolution operator for the Floquet mode $|u_n(t)\rangle = e^{iK(t)}\,|u_n\rangle$, within each T-period. Note also that as presented, the system clearly exhibits a gauge invariance under changes of choice of reference frame t_0, i.e. regardless of the choice of t_0 the time-evolution must describe the same physics.

The reason for the name quasi-energy, as well as the reason for performing this split in the firs is that this quantity plays a role analogous to the crystal momentum or quasi-momentum time-periodic Hamiltonians. Much like the crystal momentum, a redundancy is present in its definition. To the crystal momentum, reciprocal lattice vectors can be added at will without changing the Bloch state. Similarly, one can add integer multiples of the photon energy $\hbar\omega = 2\pi\hbar/T$ to the quasi-energy, and this does not result

in changes to the state. This freedom leads, in the case of translations, to all distinguished vectors in the reciprocal space being restricted to the first BZ, and similarly, in the case of $T-$periodicity, it is customary to introduce the concept of the Floquet-Brillouin Zone (FBZ) $[-\hbar\omega/2, \hbar\omega/2]$. This results in the replication of the system's energy bands into a set of replicas $\varepsilon_{nm} = \varepsilon_n + m\hbar\omega$, with energy now indexed by an additional replica label m. Now, even though these considerations are always always mathematically true in virtue of the Floquet theorem, it is not always the case that H_F and $K(t)$ can be found. Indeed, the case when H_F and $K(t)$ are computable in an exact manner is the exception rather than the rule, and thus perturbative strategies are often employed. I will sketch here an approach connecting the so-called high-frequency approximation, to familiar degenerate perturbation theory.

With this objective in mind, it is useful to represent the time-dependent Schrodinger equation (B.2) as an eigenvalue problem with respect to these quasi-energies. Such an eigenvalue problem can be represented in matrix form if one augments the Hilbert space of the undriven system, $\mathcal{H}$, into what is often called the Floquet space $\mathcal{F} = \mathcal{H} \otimes \mathcal{L}_T$. Here $\mathcal{L}_T$ is the space of square-integrable functions, and $\mathcal{F}$ can be treated itself as a Hilbert space by equipping it with an inner product. To differentiate between states in $\mathcal{H}$ and $\mathcal{F}$ I will use a double braket notation and represent $|u_n\rangle\, e^{i\varepsilon_{nm}t} \rightarrow |u_{nm}\rangle\rangle \in \mathcal{F}$. The inner product in $\mathcal{F}$ can be written as

$$\langle\langle u \ | v\rangle\rangle = \frac{1}{T}\int_0^T \langle u \, | v\rangle \, , \tag{B.4}$$

and a basis of $\mathcal{F}$ can be picked by combining a generic basis of $\mathcal{H}$ of states $|\alpha\rangle$ and the Fourier basis of the space $\mathcal{L}_T$, $|\alpha\rangle\, e^{im\omega t} \equiv ||\alpha m\rangle\rangle$. In this space, it is possible to represent (B.2) as

$$\overline{Q}\, |u_{nm}\rangle\rangle = \varepsilon_{nm}\, |u_{nm}\rangle\rangle \, , \tag{B.5}$$

where $\overline{Q} = H(t) - i\hbar\partial_t$ is called the quasi-energy operator. It is simple to show that matrix elements of $\overline{Q}$ in the aforementioned basis of $\mathcal{F}$ read $\langle\langle \alpha' m' |\, \overline{Q}\, |\alpha m\rangle\rangle = \langle \alpha' |\, H_{m'-m}(t)\, |\alpha\rangle + \delta_{m'm}\delta_{\alpha'\alpha} m\hbar\omega$, where H_m represent the Fourier components of the Hamiltonian

$$H_m \;\; = \;\; \frac{1}{T}\int_0^T dt e^{-im\omega t} H(t) = H_{-m}^{\dagger}. \tag{B.6}$$

The $\overline{Q}$ operator can be represented in matrix form, as in panel (b) of Fig. The representation is closely related to the dressed-atom picture for a quantum system driven by coherent radiation. For this reason, the Fourier index m is often called the "photon" number, and H_m are said to describe m-photon processes. This terminology suggests an intuitive picture for the physics of the time-periodically driven

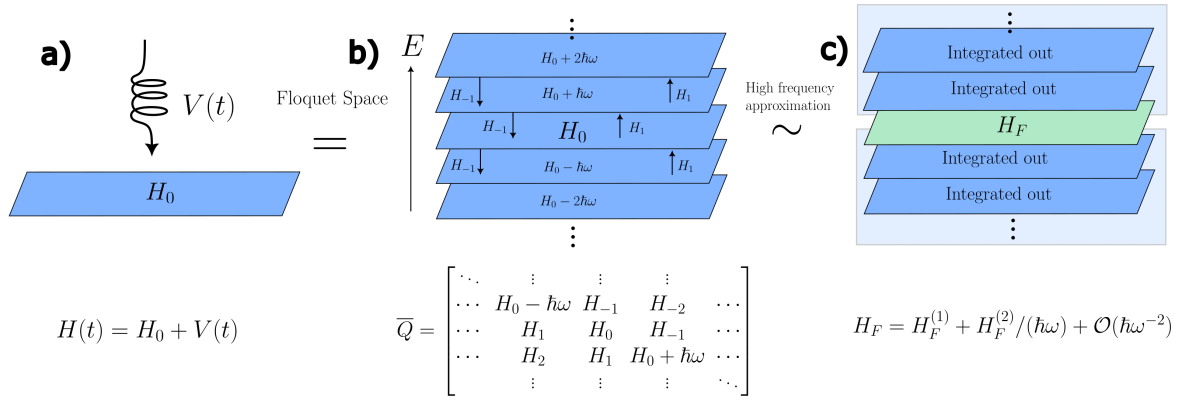

Figure 23: (a) Hamiltonian H_0 driven by a periodic field $V(t) = V(t+T)$. (b) Representation of the system in Floquet space, with replicas of the undriven system shifted by integer multiples of the driving frequency. The picture is an intuitive representation of the matrix $\overline{Q}$ in Floquet space. (c) Representation of the high frequency approximation as a scheme for integrating out the Fourier modes coupling different replicas of the system. Figure inspired and adapted from [197].

quantum system, and can be employed even when the system is actually not driven by a photon mode.

Solving the time-dependent Schrodinger equation amounts to simply amounts to diagonalizing $\overline{Q}$ but a full diagonalization in Floquet space requires diagonalizing the matrix form of $\overline{Q}$ as well as each of the time-independent H_ms. In practice, to deal with the time-dependent nature of the problem, a block diagonalization in terms of the photon number is sufficient. This proceeds by finding $m-$translational invariant unitary operators $\overline{U}_B$ such that $\overline{Q}_B = \overline{U}_B^\dagger \overline{Q} \overline{U}_B$ is block-diagonal. Conjugation by $\overline{U}_B$ in the Floquet space is equivalent to a gauge transformation

$$H(t) \to H'(t) = U^\dagger(t) H(t) U(t) - i\hbar U^\dagger(t) \partial_t U(t), \tag{B.7}$$

$$|\psi(t)\rangle \to |\psi'(t)\rangle = U^\dagger(t) |\psi(t)\rangle , \tag{B.8}$$

where $U(t)$ is a time-periodic unitary operator. The advantage found in treating the problem in the Floquet space is that one can use methods from time-independent perturbation theory to approximately block-diagonalize $\overline{Q}$. Note that block-diagonalizing $\overline{Q}$, and finding the corresponding time-independent $H_B = U_B^\dagger(t) H(t) U_B(t) - i\hbar U_B^\dagger(t) \partial_t U_B(t)$ is the same, up to a unitary transformation, as finding the Floquet effective Hamiltonian H_F, and indeed the operators $U_B(t)$ can be related to the kick operators as $U_B(t) = e^{iK(t)/\hbar}$. The use of perturbative methods, and in particular, Van Vleck degenerate perturbation theory, is appropriate here, as one can often write

$$\overline{Q} = \overline{Q}_0 + \overline{V}, \tag{B.9}$$

where $\overline{Q}_0$ is an already block-diagonal part of the Hamiltonian, containing the undriven Hamiltonian,

and which obeys $\overline{Q}_0 \left|\alpha m\right\rangle\rangle = \varepsilon^{(0)}_{\alpha m} \left|\alpha m\right\rangle\rangle$. If the energy $\hbar\omega$ is much larger than the energy scale of the Hamiltonian, the $\mathbb{Z}$-index m separates the eigenstates into multiple subsets, and the states within each subset m are labeled by the index α, spanning the unperturbed subspace $\mathcal{F}^{(0)}_m$ with m photons. The idea is that if the perturbation $\overline{V}$ is slowly turned on without closing the spectral gaps between the replicas, the unperturbed subspaces $\mathcal{F}^{(0)}_m$ will be transformed adiabatically to the perturbed subspaces $\mathcal{F}_m$, corresponding to a diagonal block of the perturbed problem. These subspaces will be spanned by new basis states $\left|\alpha m\right\rangle\rangle_B$ that deviate from the unperturbed states by small perturbative admixtures of states from the $m-$photon subspace alone. Thus, an expansion in the perturbation containing successive corrections can be written down. This is exactly the content of the Van Vleck perturbation theory. Here, the form of the first two non-zero corrections for the Hamiltonian are given for completeness

$$H_F^{(0)} = 0 \tag{B.10}$$

$$H_F^{(1)} = H_0 \tag{B.11}$$

$$H_F^{(2)} = \sum_{m\neq 0} \frac{[H_m, H_{-m}]}{m\hbar\omega}. \tag{B.12}$$

As could be intuited from this discussion, the first order correction is simply the time-average of the Hamiltonian over a driving period, and further corrections involve couplings of different Fourier modes of the Hamiltonian. These time-independent corrections stemming from periodic driving of a system can have a profound impact on the ground state as well as topological properties of materials, which suggests driving protocols as a powerful method for engineering and manipulating transport, response and topological properties. This has been explored thoroughly, for instance for Dirac Fermions in graphene subject to a periodic laser field by means of the Aharonov-Bohm effect. In Appendix C an application of these corrections to a honeycomb HSM is provided, resulting in a DMCI.

B.2 Van Vleck Degenerate perturbation theory in the Floquet Hilbert space

Degenerate perturbation theory is an approximation scheme that allows for the systematic block diagonalization of a hermitian operator into two subspaces separated by a spectral gap. In this Appendix I will describe the degenerate perturbation theory as applied to the quasi-energy operator $\overline{Q}$ in the extended Floquet Hilbert space $\mathcal{F}$ and generalize it into an approximation scheme for the systematic block diagonalization of $\overline{Q}$ into multiple subspaces separated by spectral gaps. Let a Floquet system be described by a quasi-energy operator

$$\overline{Q} = \overline{Q}_0 + \lambda \overline{V}, \tag{B.13}$$

where the dimensionless parameter λ is eventually set to unity but is otherwise included to keep track of the perturbation order in which $\overline{V}$ appears. The eigenstates of the unperturbed quasi-energy operator $\overline{Q}_0$ are $|\alpha m\rangle\rangle$, the eigenvalues $\varepsilon^{(0)}_{\alpha m}$, the unperturbed quasi-energies, are known and fulfill $\overline{Q}_0 \, |\alpha m\rangle\rangle = \varepsilon^{(0)}_{\alpha m} \, |\alpha m\rangle\rangle$ as described in Appendix C. The index m separates the eigenstates into multiple subsets, and the states within each subset m are labeled by the index α and span the unperturbed subspace $\mathcal{F}^{(0)}_m$ related to m. In order to proceed, assume that the quasi-energies of two subsets m and m' shall be separated by a quasi-energy gap that is large compared to the matrix elements of the perturbation $\overline{V}$. When this perturbation is slowly turned on without closing the spectral gaps, the unperturbed subspaces $\mathcal{F}^{(0)}_m$ will be transformed adiabatically to the perturbed subspaces $\mathcal{F}_m$, corresponding to a diagonal block of the perturbed problem. These subspaces will be spanned by new basis states $|\alpha m\rangle\rangle_B$ that deviate from the unperturbed states by small perturbative admixtures of states from other subspaces. The states $|\alpha m\rangle\rangle$ are decoupled from subspaces $\mathcal{F}_{m'}$ with $m' \neq m$.

$$_B\langle\langle \alpha' m' | \, \overline{Q} \, |\alpha m\rangle\rangle_B = 0 \text{ for } m' \neq m, \tag{B.14}$$

but generally they are not eigenstates of the perturbed quasi-energy operator $\overline{Q}$, so that it is possible that $_B \langle\langle \alpha' m | \, \overline{Q} \, |\alpha m\rangle\rangle_B \neq 0$ for $\alpha' \neq \alpha$. The role of degenerate perturbation theory is to find systematic expansions for both the states $|\alpha m\rangle\rangle_B$, for the unitary operator $\overline{U}$ that relates them to the unperturbed states via

$$|\alpha m\rangle\rangle_B = \overline{U} \, |\alpha m\rangle\rangle \, , \tag{B.15}$$

as well as for the matrix elements $_B \langle\langle \alpha' m | \, \overline{Q} \, |\alpha m\rangle\rangle_B$ describing the physics within each subspace $\mathcal{F}_m$. First of all, define projectors

$$\overline{P}_m = \sum_\alpha |\alpha m\rangle\rangle \, \langle\langle \alpha m | \, , \tag{B.16}$$

onto the unperturbed subspaces $\mathcal{F}^{(0)}_m$ such that $\sum_m \overline{P}_m = \overline{\mathbb{1}}$.These can be used to decompose any operator as $\overline{A} = \overline{A}_D + \overline{A}_X$,into a block-diagonal part

$$\overline{A}_D = \sum_m \overline{P}_m \overline{A P}_m, \tag{B.17}$$

and a block-off-diagonal part

$$\overline{A}_X = \sum_m \sum_{m' \neq m} \overline{P}_{m'} \overline{A P}_m. \tag{B.18}$$

A few useful properties of products of block-diagonal and block-off-diagonal operators read, for generic operators A and B,

$$\overline{A}_D \overline{B}_D = \left(\overline{A}_D \overline{B}_D\right)_D, \ \left(\overline{A}_D \overline{B}_D\right)_X = 0, \tag{B.19}$$

$$\overline{A}_D \overline{B}_X = \left(\overline{A}_D \overline{B}_X\right)_X, \ \left(\overline{A}_D \overline{B}_X\right)_D = 0, \tag{B.20}$$

$$\overline{A}_X \overline{B}_D = \left(\overline{A}_X \overline{B}_D\right)_X, \ \left(\overline{A}_X \overline{B}_D\right)_D = 0. \tag{B.21}$$

Another slightly different property, is that the product of two block-off-diagonal operators may contain a block-diagonal part, and thus

$$\overline{A}_X \overline{B}_X = \left(\overline{A}_X \overline{B}_X\right)_D + \left(\overline{A}_X \overline{B}_X\right)_X. \tag{B.22}$$

The objective of this Appendix B.2. is to provide a systematic procedure to block diagonalize the full unperturbed quasi-energy operator $\overline{Q}$ by means of a unitary operator $\overline{U}$ such that

$$\overline{U}^\dagger \overline{Q U} = \overline{Q}_0 + \overline{W}, \tag{B.23}$$

where $\overline{W}$ is block-diagonal, i.e. $\overline{W} = \overline{W}_D$, $\overline{W}_X = 0$. A parameter λ is introduced which allows to keep track of the perturbation order when computing any quantity in the perturbative analysis, such that

$$\overline{U}^\dagger \overline{Q U} = \overline{U}^\dagger \left[\overline{Q}_0 + \lambda \left(\overline{V}_D + \overline{V}_X\right)\right] \overline{U}. \tag{B.24}$$

The requirement that $\overline{U}^\dagger \overline{Q U}$ be diagonal amounts to imposing the condition

$$\text{COND 1: } \left[\overline{U}^\dagger \left(\overline{Q}_0 + \lambda \left(\overline{V}_D + \overline{V}_X\right)\right) \overline{U}\right]_D = \overline{Q}_0 + \overline{W}, \tag{B.25}$$

as well as

$$\text{COND 2: } \left[\overline{U}^\dagger \left(\overline{Q}_0 + \lambda \left(\overline{V}_D + \overline{V}_X\right)\right) \overline{U}\right]_X = 0. \tag{B.26}$$

The unitary operator $\overline{U}$ defines the new basis of $\mathcal{F}_m$. It can be expressed, like any other unitary operator, in terms of an anti-hermitian operator $\overline{G}$ via the exponential map $\overline{U} = e^{\overline{G}}$, however it is not uniquely determined unless the additional conditions $\overline{G} = \overline{G}_X$, $\overline{G}_D = 0$, are also added. These keep the mixing of states within each subspace $\mathcal{F}_m^{(0)}$ small. $\overline{W}$ and $\overline{U}$ can be expanded in powers n of the perturbation

$$\overline{W} = \sum_{n=0}^{\infty} \lambda^n \overline{W}^{(n)}, \tag{B.27}$$

with $\overline{W}^{(n)} = \overline{W}_D^{(n)}$, $\overline{W}_X^{(n)} = 0$,and similarly

$$\overline{U} = \sum_{n=0}^{\infty} \lambda^n \overline{U}^{(n)}. \tag{B.28}$$

Note that the terms $\overline{U}^{(n)}$ can be related to the terms in a perturbative expansion of $\overline{G}$ as

$$\overline{G} = \sum_{n=0}^{\infty} \lambda^n \overline{G}^{(n)}, \tag{B.29}$$

where $\overline{G}^{(n)} = \overline{G}_X^{(n)}$, $\overline{G}_D^{(n)} = 0$. Furthermore, anti-Hermiticity imposes $\overline{G}^{(n)} = -\left[\overline{G}^{(n)}\right]^\dagger$,and therefore one finds

$$\begin{aligned}
\overline{U}^{(0)} &= \overline{\mathbb{1}} \\
\overline{U}^{(1)} &= \overline{G}^{(1)} \\
\overline{U}^{(2)} &= \overline{G}^{(2)} + \frac{1}{2}\left[\overline{G}^{(1)}\right]^2 \\
&\vdots
\end{aligned} \tag{B.30}$$

Plugging these expressions into the conditions COND 1 and COND 2 a set of equations are obtained which relate the power expansions of $\overline{W}$ and those of $\overline{V}$ and $\overline{G}$, and determine $\overline{W}$ and $\overline{G}$ order by order. For the zeroth order, one finds $\left[\overline{U}^{\dagger(0)}\overline{Q}_0\overline{U}^{(0)}\right]_D = \overline{Q}_0 + \overline{W}^{(0)}$ and thus $\overline{W}^{(0)} = 0$. The condition COND 2 reduces, in the zeroth order, to $0 = 0$. Proceeding with the first correction,

$$\begin{aligned}
\overline{W}^{(1)} &= \left[\overline{U}^{\dagger(1)}\overline{Q}_0\overline{U}^{(0)}\right]_D + \left[\overline{U}^{\dagger(0)}\overline{Q}_0\overline{U}^{(1)}\right]_D + \left[\overline{U}^{\dagger(0)}\left(\overline{V}_D + \overline{V}_X\right)\overline{U}^{(0)}\right]_D \\
\Rightarrow \overline{W}^{(1)} &= \left[\overline{G}^{(1)\dagger}\overline{Q}_0\right]_D + \left[\overline{Q}_0\overline{G}^{(1)}\right]_D + \left[\overline{V}_D + \overline{V}_X\right]_D. \\
\Rightarrow \overline{W}^{(1)} &= \left[\overline{Q}_0, \overline{G}^{(1)}\right]_D + \overline{V}_D.
\end{aligned} \tag{B.31}$$

Using (B.21) it is quite simple to show that $\left[\overline{Q}_0, \overline{G}^{(1)}\right]_D = 0$. From the COND 2, it is also simple to find the equality $\left[\overline{Q}_0, \overline{G}^{(1)}\right]_X = -\overline{V}_X$. For second and third order corrections, the mathematics becomes more cumbersome, but from COND 1 and COND 2 also follow

$$\overline{W}^{(1)} = \overline{V}_D, \tag{B.32}$$

$$\overline{W}^{(2)} = \frac{1}{2}\left[\overline{V}_X, \overline{G}^{(1)}\right]_D, \tag{B.33}$$

$$\overline{W}^{(3)} = \frac{1}{2}\left[\overline{V}_X, \overline{G}^{(2)}\right]_D + \frac{1}{12}\left[\left[\overline{V}_X, \overline{G}^{(1)}\right], \overline{G}^{(1)}\right]_D, \tag{B.34}$$

The general idea is that from the commutators $\left[\overline{G}^{(n)}, \overline{Q}_0\right]$, all matrix elements of $\overline{G}$ can be constructed order by order. Since $\overline{G}_D = 0$, due to anti-Hermiticity, $\langle\langle \alpha' m' | \, \overline{G}^{(n)} \, | \alpha m \rangle\rangle = 0$,and therefore the matrix elements of $\overline{G}^{(n)}$ couple states $|\alpha m\rangle\rangle$ and $|\alpha' m'\rangle\rangle$ for $m' \neq m$ only, and obey $\langle\langle \alpha' m' | \, \overline{G}^{(n)} \, | \alpha m \rangle\rangle = -\langle\langle \alpha m | \, \overline{G}^{(n)} \, | \alpha' m' \rangle\rangle^*$. Using the matrix elements of the commutator $\langle\langle \alpha' m' | \left[\overline{G}^{(n)}, \overline{Q}_0\right] | \alpha m \rangle\rangle = \left(\varepsilon^{(0)}_{\alpha m} - \varepsilon^{(0)}_{\alpha' m'}\right) \langle\langle \alpha' m' | \, \overline{G}^{(n)} \, | \alpha m \rangle\rangle$,it is possible to compute the matrix elements for $m' \neq m$ of the first perturbations $\overline{G}^{(n)}$ as

$$\langle\langle \alpha' m' | \, \overline{G}^{(1)} \, | \alpha m \rangle\rangle = -\frac{\langle\langle \alpha' m' | \, \overline{V}_X \, | \alpha m \rangle\rangle}{\varepsilon^{(0)}_{\alpha m} - \varepsilon^{(0)}_{\alpha' m'}} \tag{B.35}$$

$$\begin{aligned}
\langle\langle \alpha' m' | \, \overline{G}^{(2)} \, | \alpha m \rangle\rangle = &-\sum_{\alpha''} \frac{\langle\langle \alpha' m' | \, \overline{V}_X \, | \alpha'' m' \rangle\rangle \, \langle\langle \alpha'' m' | \, \overline{V}_X \, | \alpha m \rangle\rangle}{\left(\varepsilon^{(0)}_{\alpha'' m'} - \varepsilon^{(0)}_{\alpha' m'}\right)\left(\varepsilon^{(0)}_{\alpha m} - \varepsilon^{(0)}_{\alpha'' m'}\right)} \\
&-\sum_{\alpha''} \frac{\langle\langle \alpha' m' | \, \overline{V}_X \, | \alpha'' m \rangle\rangle \, \langle\langle \alpha'' m | \, \overline{V}_D \, | \alpha m \rangle\rangle}{\left(\varepsilon^{(0)}_{\alpha' m'} - \varepsilon^{(0)}_{\alpha m}\right)\left(\varepsilon^{(0)}_{\alpha' m'} - \varepsilon^{(0)}_{\alpha'' m}\right)} \\
&+\sum_{\alpha''} \sum_{m'' \neq m, m'} \frac{\langle\langle \alpha' m' | \, \overline{V}_X \, | \alpha'' m'' \rangle\rangle \, \langle\langle \alpha'' m'' | \, \overline{V}_D \, | \alpha m \rangle\rangle}{\left(\varepsilon^{(0)}_{\alpha' m'} - \varepsilon^{(0)}_{\alpha m}\right)} \qquad \text{(B.36)} \\
&\times \frac{1}{2}\left[\frac{1}{\left(\varepsilon^{(0)}_{\alpha'' m''} - \varepsilon^{(0)}_{\alpha' m'}\right)} + \frac{1}{\left(\varepsilon^{(0)}_{\alpha'' m''} - \varepsilon^{(0)}_{\alpha m}\right)}\right]. \qquad \text{(B.37)}
\end{aligned}$$

To reconstruct $\overline{U}$ from $\overline{G}^{(n)}$, one can either write $\overline{U} \approx \exp\left(\overline{G}^{(1)} + \overline{G}^{(2)} + \cdots + \overline{G}^{(n)}\right) \equiv \overline{U}^{[n]}$,or consider $\overline{U} \approx \overline{\mathbb{1}} + \overline{U}^{(1)} + \overline{U}^{(2)} + \cdots + \overline{U}^{(n)}$. The first option has the advantage of preserving unitary at every finite n, however, the second approximation does not. Regardless, sometimes unitarity is not relevant to the problem at hand, and the second approximation is more convenient to compute. For this reason, the latter approach is used, where the leading terms in the expansion of the matrix elements can be evaluated as

$$\langle\langle \alpha' m' | \, \overline{U}^{(0)} \, | \alpha m \rangle\rangle = \langle\langle \alpha' m' | \, | \alpha m \rangle\rangle = \delta_{\alpha,\alpha'} \delta_{m,m'} \tag{B.38}$$

$$\langle\langle \alpha' m' | \, \overline{U}^{(1)} \, | \alpha m \rangle\rangle = - \frac{\langle\langle \alpha' m' | \, \overline{V}_X \, | \alpha m \rangle\rangle}{\varepsilon^{(0)}_{\alpha m} - \varepsilon^{(0)}_{\alpha' m'}} \tag{B.39}$$

$$\begin{aligned} \langle\langle \alpha' m' | \, \overline{U}^{(2)} \, | \alpha m \rangle\rangle = & \sum_{\alpha''} \frac{\langle\langle \alpha' m' | \, \overline{V}_D \, | \alpha'' m' \rangle\rangle \, \langle\langle \alpha'' m' | \, \overline{V}_X \, | \alpha m \rangle\rangle}{\left(\varepsilon^{(0)}_{\alpha'' m'} - \varepsilon^{(0)}_{\alpha' m'} \right) \left(\varepsilon^{(0)}_{\alpha m} - \varepsilon^{(0)}_{\alpha'' m'} \right)} \\ & - \sum_{\alpha''} \frac{\langle\langle \alpha' m' | \, \overline{V}_X \, | \alpha'' m \rangle\rangle \, \langle\langle \alpha'' m | \, \overline{V}_D \, | \alpha m \rangle\rangle}{\left(\varepsilon^{(0)}_{\alpha' m'} - \varepsilon^{(0)}_{\alpha m} \right) \left(\varepsilon^{(0)}_{\alpha' m'} - \varepsilon^{(0)}_{\alpha'' m} \right)} \\ & + \sum_{\alpha''} \sum_{m'' \neq m, m'} \frac{\langle\langle \alpha' m' | \, \overline{V}_X \, | \alpha'' m'' \rangle\rangle \, \langle\langle \alpha'' m'' | \, \overline{V}_D \, | \alpha m \rangle\rangle}{\left(\varepsilon^{(0)}_{\alpha' m'} - \varepsilon^{(0)}_{\alpha m} \right) \left(\varepsilon^{(0)}_{\alpha' m'} - \varepsilon^{(0)}_{\alpha'' m''} \right)}. \end{aligned} \tag{B.40}$$

The only object that remains to be determined are the matrix elements of the diagonal blocks of the quasi-energy operator that describe the physics within the subspace $\mathcal{F}_m$, namely

$$\begin{aligned} Q_{m,\alpha'\alpha} =_B & \langle\langle \alpha' m | \, \overline{Q} \, | \alpha m \rangle\rangle_B \\ = & \langle\langle \alpha' m | \, \overline{U}^{\dagger} \overline{Q U} \, | \alpha m \rangle\rangle \\ = & \langle\langle \alpha' m | \, \overline{Q}_0 + \overline{W} \, | \alpha m \rangle\rangle \, . \end{aligned} \tag{B.41}$$

Expanding the quasi-energy operator in perturbation theory $Q_{m,\alpha'\alpha} = \sum_{n=0}^{\infty} \lambda^n Q^{(n)}_{m,\alpha'\alpha}$,and matching the same powers in λ term by term with the respective corrections one finds:

$$Q^{(0)}_{m,\alpha'\alpha} = \delta_{\alpha,\alpha'} \varepsilon^{(0)}_{\alpha m} \tag{B.42}$$

$$Q^{(1)}_{m,\alpha'\alpha} = \langle\langle \alpha' m | \, \overline{V}_D \, | \alpha m \rangle\rangle \tag{B.43}$$

$$Q^{(2)}_{m,\alpha'\alpha} = \sum_{\alpha''} \sum_{m' \neq m} \langle\langle \alpha' m' | \, \overline{V}_X \, | \alpha'' m' \rangle\rangle \, \langle\langle \alpha'' m' | \, \overline{V}_X \, | \alpha m \rangle\rangle \tag{B.44}$$

$$\times \frac{1}{2} \left[\frac{1}{\varepsilon^{(0)}_{\alpha' m} - \varepsilon^{(0)}_{\alpha'' m'}} + \frac{1}{\varepsilon^{(0)}_{\alpha m} - \varepsilon^{(0)}_{\alpha'' m'}} \right]. \tag{B.45}$$

These expressions are relevant for the computation of the effective Hamiltonian. It is, at this point, worthwhile to particularize to the case of a driven system, a particularization performed in Appendix B.3.

B.3 Application to a driven system

The previously derived perturbation theory can be applied to the case of a Floquet system. The unperturbed problem by reducing $Q_0(t)$ to the "photonic" part of the quasi-energy operator $Q(t) = -i\hbar\partial_t$,or in Floquet space

$$\overline{Q}_0 = \sum_m \sum_\alpha m\hbar\omega \left|\alpha m\right\rangle\rangle \left\langle\langle \alpha m\right| , \tag{B.46}$$

which does not depend on the undriven Hamiltonian of the lattice model. Note that $\overline{Q}_0$ is diagonal with respect to any set of basis states of the type $\left|\alpha m\right\rangle\rangle$. The perturbation is given by the driven Hamiltonian $\hat{V}(t) = \hat{H}(t)$,or in the Floquet space notation $\overline{V} = \overline{H} = \sum_{m'} \sum_{m\alpha'\alpha} \left|\alpha' m'\right\rangle\rangle \left\langle \alpha'\right| \hat{H}_{m'-m} \left|\alpha\right\rangle \left\langle\langle \alpha m\right|$. The perturbation can be decomposed as $\overline{V} = \overline{V}_D + \overline{V}_X$,where $\overline{V}_D$ comprises the $m' = m$ terms describing zero-"photon" processes, which are determined by the time-averaged Hamiltonian $\hat{V}_D = \hat{H}_0$. The block-off-diagonal part $\overline{V}_X$ describes $\Delta m = m' - m$-"photon" processes determined by the Fourier components $H_{m'-m}$ of the Hamiltonian

$$\hat{V}_X = \sum_{\Delta m \neq 0} e^{i\Delta m\omega t} \hat{H}_{\Delta m}. \tag{B.47}$$

The application of the degenerate perturbation theory to this system. The objective is to compute the unitary operator $\overline{U}_B$ that relates the unperturbed basis states $\left|\alpha' m'\right\rangle\rangle$ to the perturbed basis states $\left|\alpha m\right\rangle\rangle_B$ that block diagonalize the quasi-energy operator in a perturbative fashion. As described before, these operators can be written at the cost of anti-hermitian operators $\overline{G}$ which can be themselves calculated perturbatively. The expansion is

$$\begin{aligned} \overline{U}_B = \exp\left(\overline{G}\right) &\approx \overline{U}_B^{(0)} + \overline{U}_B^{(1)} + \overline{U}_B^{(2)} + \cdots \\ &\approx \mathbb{1} + \frac{1}{2}\left[\overline{G}^{(1)}\right]^2 + \cdots \end{aligned} \tag{B.48}$$

the leading terms in the expansion of $\overline{G}$ can be computed from the previously derived formulae such as

$$\begin{aligned} \left\langle\langle \alpha' m'\right| \overline{G}^{(1)} \left|\alpha m\right\rangle\rangle &= -\frac{\left\langle\langle \alpha' m'\right| \overline{V}_X \left|\alpha m\right\rangle\rangle}{\varepsilon^{(0)}_{\alpha' m'} - \varepsilon^{(0)}_{\alpha m}} \\ &= -\sum_{m_3 \neq m_2} \sum_{m_2 \alpha_3 \alpha_2} \frac{\left\langle\langle \alpha' m'\right| \left|\alpha_3 m_3\right\rangle\rangle \left\langle \alpha_3\right| \hat{H}_{m'-m} \left|\alpha_2\right\rangle \left\langle\langle \alpha_2 m_2\right| \left|\alpha m\right\rangle\rangle}{(m'-m)\hbar\omega} \\ &= -\sum_{m_3 \neq m_2} \sum_{m_2 \alpha_3 \alpha_2} \frac{\delta_{m_3 m'} \delta_{\alpha_3, \alpha'} \left\langle \alpha_3\right| \hat{H}_{m'-m} \left|\alpha_2\right\rangle \delta_{m_2, m} \delta_{\alpha_2, \alpha}}{(m'-m)\hbar\omega} \\ &= -\frac{\left\langle \alpha'\right| \hat{H}_{m'-m} \left|\alpha\right\rangle}{(m'-m)\hbar\omega}. \end{aligned} \tag{B.49}$$

Using a similar procedure, one finds

$$\langle\langle \alpha' m' | \, \overline{G}^{(2)} \, | \alpha m \rangle\rangle = \frac{\langle \alpha' | \left[\hat{H}_0, \hat{H}_{m'-m} \right] | \alpha \rangle}{\left[(m'-m)\, \hbar\omega \right]^2} + \sum_{m'' \neq m, m'} \frac{\langle \alpha' | \left[\hat{H}_{m'-m''}, \hat{H}_{m''-m} \right] | \alpha \rangle}{(m'-m)\, \hbar\omega} \tag{B.50}$$

$$\frac{1}{2} \left[\frac{1}{(m''-m')\, \hbar\omega} + \frac{1}{(m''-m)\, \hbar\omega} \right]. \tag{B.51}$$

From the expansion in powers of $\overline{G}$, $\overline{U}_B$ can be approximated. The first order correction is

$$\langle\langle \alpha' m' | \, \frac{1}{2} \left[\overline{G}^{(1)} \right]^2 | \alpha m \rangle\rangle = \sum_{m'' \neq m} \frac{\langle \alpha' | \, \hat{H}_{m'-m} \hat{H}_{m''-m} \, | \alpha \rangle}{(m'-m)\,(m''-m)\,(\hbar\omega)^2}. \tag{B.52}$$

And finally, since for translationally invariant operators in the photon number

$$\hat{A}_m = \sum_{\alpha' \alpha} \langle\langle \alpha m | \, \overline{A} \, | \alpha' 0 \rangle\rangle \, | \alpha' \rangle \, \langle \alpha' | \,, \tag{B.53}$$

one can write

$$\begin{aligned} \hat{G}^{(1)} &= -\sum_{m \neq 0} e^{im\omega t} \sum_{\alpha' \alpha} \frac{\langle \alpha' | \, \hat{H}_{-m} \, | \alpha \rangle}{m\hbar\omega} \, | \alpha' \rangle \, \langle \alpha' | \\ &= -\sum_{m \neq 0} \frac{e^{im\omega t}}{m\hbar\omega} \hat{H}_m. \end{aligned} \tag{B.54}$$

As for the effective Floquet Hamiltonian, the procedure is much the same. Firstly, the matrix elements for $m = m' = 0$ can be computed

$$\begin{aligned} H^B_{\alpha',\alpha} &= \langle \alpha' | \, \hat{H}_F \, | \alpha \rangle \\ &= \langle\langle \alpha' 0 | \, \overline{U}^\dagger_B \overline{Q U}_B \, | \alpha 0 \rangle\rangle \\ &= Q_{0,\alpha'\alpha}, \end{aligned} \tag{B.55}$$

and expanding $\overline{U}_B$ and grouping together terms in the same perturbation order, leads to an expansion as

$$\hat{H}_F = \sum_{\nu=0}^{\infty} \hat{H}_F^{(\nu)}. \tag{B.56}$$

Carrying out this computation explicitly is a long-winded process. But the result, to second order, is simply the corrections given at the end of section B.1.

Appendix C
Details on the Floquet Magnon Chern Insulator

In this Appendix I will go over some details of the derivation of the FMCI Hamiltonian using the high-frequency approximation of Floquet theory. Consider a spin-S system in the honeycomb lattice spanning the xy plane, and an incident electric field

$$\boldsymbol{E}(t) = E_0 \left(\cos\omega t, \tau \sin\omega t, 0\right), \tag{C.1}$$

that is irradiates the lattice propagating in the z direction. $\tau = \pm 1$ indicates the polarization with $\tau = +1$ corresponding to right-handed and $\tau = -1$ to left-handed polarizations. The Aharonov-Casher (A-C) phase picked up between two points $\boldsymbol{r}_i$ and $\boldsymbol{r}_j$ is

$$\gamma_{ij}^{AC}(t) = -\frac{\mu_B}{\hbar e c^2}\int_{\boldsymbol{r}_i}^{\boldsymbol{r}_j} \hat{\boldsymbol{z}} \times \boldsymbol{E}(\boldsymbol{r}') \cdot d\boldsymbol{l}'. \tag{C.2}$$

The integral can be computed explicitly, first by computing the vector product $\hat{\boldsymbol{z}}\times\boldsymbol{E} = E_0\left(-\tau\sin\omega t, \cos\omega t, 0\right)$, and then by taking the path between $\boldsymbol{r}_\alpha$ and $\boldsymbol{r}_\beta$ to be a straight line. To integrate in Cartesian coordinates, the distance between the points is written as δ_{ij} and the angle between the straight line and the x axis to be ϕ_{ij}, that is to say $d\boldsymbol{l}' = (\cos\phi_{ij}dx', \sin\phi_{ij}dy', 0)$, the A-C phase is given by

$$\begin{aligned}
\gamma_{ij}^{AC}(t) &= -\frac{\mu E_0}{\hbar e c^2}\int_{\boldsymbol{r}_i}^{\boldsymbol{r}_j} \begin{bmatrix} -\tau\sin\Omega t \\ \cos\Omega t \\ 0 \end{bmatrix} \cdot \begin{bmatrix} \cos\phi_{ij}dx' \\ \sin\phi_{ij}dy' \\ 0 \end{bmatrix} \\
&= \frac{\mu E_0}{\hbar e c^2}\delta_{ij}\tau\left[\sin\omega t\cos\phi_{ij} - \tau\cos\omega t\sin\phi_{ij}\right] \\
&= \frac{\mu E_0}{\hbar e c^2}\delta_{ij}\tau\sin\left(\omega t - \tau\phi_{ij}\right),
\end{aligned} \tag{C.3}$$

where in the last line the identity $\sin(\alpha+\tau\beta) = \sin\alpha\cos\beta + \tau\cos\alpha\sin\beta$ was used. It is conventional to define $\lambda_{ij} \equiv \mu_B E_0\delta_{ij}/\hbar e c^2$ to write more succinctly

$$\gamma_{ij}^{AC}(t) = \tau\lambda_{ij}\sin\left(\omega t - \tau\phi_{ij}\right). \tag{C.4}$$

For a 2D ferromagnetic spin-S system described by the Heisenberg model, as

$$H = -J \sum_{\langle i,j \rangle} \left[S_i^z S_j^z + \frac{1}{2} \left(S_i^+ S_j^- + S_j^+ S_i^- \right) \right], \tag{C.5}$$

the AC phase generated by the field generates a time-dependence results in

$$H(t) = -J \sum_{\langle i,j \rangle} \left[S_i^z S_j^z + \frac{1}{2} \left(S_i^+ S_j^- e^{i\gamma_{ji}^{AC}(t)} + S_j^+ S_i^- e^{i\gamma_{ij}^{AC}(t)} \right) \right], \tag{C.6}$$

which can be compressed to

$$H(t) = -J \sum_{\langle i,j \rangle} \left[S_i^z S_j^z + S_j^+ S_i^- e^{i\gamma_{ij}^{AC}(t)} \right], \tag{C.7}$$

by noting that the summation is occurring over all sites, and therefore each of the two terms involving $S_i^+ S_j^-$ in the Hamiltonian gives exactly the same contribution. Now, the first order correction of the high-frequency approximation corresponds to the average Hamiltonian, reading

$$H_F^{(1)} = \frac{1}{T} \int_0^T dt_1 H(t_1), \tag{C.8}$$

and "killing two birds with one stone" and calculating all Fourier components of the Hamiltonian, noting that in particular $H_F^{(1)} = H^{(m=0)}$. The generic Fourier component is given by

$$H^{(m)} = \frac{1}{T} \int_0^T dt_1 H(t_1) e^{-im\omega t_1}, \tag{C.9}$$

and the Fourier coefficients of the driven exchange integrals can be written as

$$J_{ij}^{(m)} = J \frac{\omega}{2\pi} \int_0^{2\pi/\omega} dt_1 e^{i\tau\lambda_{ij} \sin\left(\omega t_1 - \tau\phi_{\alpha\beta}\right)} e^{-im\omega t_1}. \tag{C.10}$$

This integral can be solved by employing a Jacobi-Anger expansion

$$\begin{aligned} e^{iz\sin\phi} &= e^{iz\cos(\phi - \pi/2)} \\ &= \sum_{n=-\infty}^{\infty} i^n \mathcal{J}_n(z) e^{in(\phi - \pi/2)} \\ &= \sum_{n=-\infty}^{\infty} \mathcal{J}_n(z) e^{in\phi}, \end{aligned} \tag{C.11}$$

where $\mathcal{J}_n(z)$ is the nth Bessel function. Plugging it into the expression for the Fourier coefficients of the exchange integrals, one finds

$$J_{ij}^{(m)} = J \frac{\Omega}{2\pi} \int_0^{2\pi/\omega} dt_1 \sum_{n=-\infty}^{\infty} \mathcal{J}_n(\tau\lambda_{ij}) e^{in(\omega t_1 - \tau\phi_{ij})} e^{-im\omega t_1}. \tag{C.12}$$

Simplifying the expression by bringing the summation and constant phase outside the integral and grouping together the common terms yields the result

$$\begin{aligned} J_{ij}^{(m)} &= J \sum_{n=-\infty}^{\infty} \mathcal{J}_n(\tau\lambda_{ij}) e^{-in\tau\phi_{\alpha\beta}} \frac{\omega}{2\pi} \int_0^{2\pi/\omega} dt_1 e^{i(n-m)\omega t_1} \\ &= J \sum_{n=-\infty}^{\infty} \mathcal{J}_n(\tau\lambda_{ij}) e^{-in\tau\phi_{ij}} \delta_{nm} \\ &= J\mathcal{J}_m(\tau\lambda_{ij}) e^{-im\tau\phi_{ij}}. \end{aligned} \tag{C.13}$$

A useful property which can be easily derived is $J_{ji}^{(m)} = (-1)^m J_{ij}^{(m)}$. Using this result, and setting $m = 0$, find the average Hamiltonian is

$$H_F^{(1)} = -\sum_{\langle i,j \rangle} J S_i^z S_j^z + J_{ij}^{(0)} S_j^+ S_i^-, \tag{C.14}$$

thus concluding that the first term stays the same up to a renormalization of the hopping interaction $J \to J_{ij}^{(0)}$ as discussed in the main text. The second order effective Hamiltonian will be

$$H_F^{(2)} = \sum_{m=1}^{\infty} \frac{1}{m\hbar\omega} \left[H^{(m)}, H^{(-m)} \right]. \tag{C.15}$$

Note however that for all m, the Fourier component of the Hamiltonian is

$$H^{(m)} = -\sum_{\langle i,j \rangle} \left[J\delta_{m,0} S_i^z S_j^z + J_{ij}^{(m)} S_i^+ S_j^- \right], \tag{C.16}$$

and therefore the $m = 0$ contribution does not appear in the second order correction. Thus, one finds

$$\begin{aligned} \left[H^{(m)}, H^{(-m)} \right] &= \sum_{i,j} \left[J_{ij}^{(m)} S_i^+ S_j^-, J_{kl}^{(-m)} S_k^+ S_l^- \right] \\ &= \sum_{i,j} J_{ij}^{(m)} J_{kl}^{(-m)} \left[S_k^+ S_l^-, S_k^+ S_l^- \right]. \end{aligned} \tag{C.17}$$

Explicitly, the commutator of spin operators can be computed as

$$\left[S_i^+ S_j^-, S_k^+ S_l^- \right] = 2\hbar \left(\delta_{il} S_k^+ S_i^z S_j^- - \delta_{kj} S_i^+ S_j^z S_l^- \right), \tag{C.18}$$

and up to a term which vanishes when performing a summation over NNs, one can commute the S_i^z operators with S_k^+ making the replacement

$$\left[S_i^+ S_j^-, S_k^+ S_l^-\right] \to 2\hbar \left(\delta_{il} S_i^z S_k^+ S_j^- - \delta_{kj} S_j^z S_i^+ S_l^-\right). \tag{C.19}$$

The commutator of Fourier coefficients of Hamiltonians yields, after some manipulations

$$\begin{aligned}\left[H^{(m)}, H^{(-m)}\right] &\to 2\hbar \sum_{\langle i,j\rangle} \sum_{\langle k,l\rangle} J_{ij}^{(m)} J_{kl}^{(-m)} \left(\delta_{il} S_i^z S_k^+ S_j^- - \delta_{kj} S_k^z S_i^+ S_l^-\right) \\ &= 2\hbar(-1)^m \sum_{\langle i,\langle j\rangle,l\rangle} S_i^z \left(J_{ij}^{(m)} J_{il}^{(m)*} S_l^+ S_j^- - J_{ij}^{(m)} J_{il}^{(m)*} S_j^+ S_l^-\right). \end{aligned} \tag{C.20}$$

And using the previously mentioned result $J_{ji}^{(m)} = (-1)^m J_{ij}^{(m)}$, one can simplify the above expression to

$$\left[H^{(m)}, H^{(-m)}\right] = 2\hbar(-1)^m \sum_{\langle j,\langle i\rangle,l\rangle} J_{ji}^{(m)} J_{il}^{(m)*} S_i^z \left(S_j^+ S_l^- - S_l^+ S_j^-\right). \tag{C.21}$$

The summation can be interpreted as occurring over possible paths $i \to j \to l$. In a generic isotropic unstrained case, since the distance to nearest neighbors is the same, the simplification $\mathcal{J}_m(\tau\lambda) = \mathcal{J}_m(\tau\lambda_{jl}) \equiv \mathcal{J}_m(\tau\lambda_{li})$ can be performed. With some further manipulations, one can find

$$\left[H^{(m)}, H^{(-m)}\right] = \hbar J^2 \sum_{\langle j,\langle i\rangle,l\rangle} \left[\mathcal{J}_m^2(\tau\lambda) i \sin\left(m\tau\Phi_{il}\right) S_i^z \left(S_j^+ S_l^- - S_l^+ S_j^-\right)\right], \tag{C.22}$$

where $\Phi_{jl} = \phi_{ji} - \phi_{il}$ is defined. The second order correction is written succinctly as

$$H_F^{(2)} = \frac{J^2}{\hbar\omega} \sum_{\langle i,\langle j\rangle,l\rangle} \left[\sum_{m=1}^{\infty} \frac{1}{m} \mathcal{J}_m^2(\tau\lambda) i \sin\left(m\tau\Phi_{il}\right) S_j^z \left(S_i^+ S_l^- - S_l^+ S_i^-\right)\right]. \tag{C.23}$$

One final approximation is in order, which pertains to the fact that $\sum_{m=1}^{\infty} \frac{1}{m} \mathcal{J}_m^2(\tau\lambda)$ is dominated by small m contributions, and hence it is possible to approximate

$$H_F^{(2)} = \frac{\tau\sqrt{3}J^2}{\hbar\omega} \sum_{\langle i,\langle j\rangle,l\rangle} \mathcal{J}_1^2(\tau\lambda) i S_j^z \left(S_i^+ S_l^- - S_l^+ S_i^-\right). \tag{C.24}$$

This Hamiltonian is useful as is, but it is worth noting that in the ferromagnetic ground state, and employing the philosophy of the linear spin-wave approximation, using $S_j^z \approx S$, it is possible to write

$$H_F^{(2)} = \frac{\tau 3\sqrt{3}J^2 S \mathcal{J}_1^2(\tau\lambda)}{\hbar\omega} \sum_{\langle i,l\rangle} \hat{\boldsymbol{z}} \cdot \left(\boldsymbol{S}_i \times \boldsymbol{S}_l\right), \tag{C.25}$$

which is exactly a DMI term. This mechanism of driving by a $T-$periodic electric field coupling to a magnetic system in the honeycomb lattice is therefore seen to yield a synthetic DMI as a second-order correction. As discussed in the main text, the mapping between such a system and the Haldane model results in a topologically non-trivial band structure for magnonic excitations, and thus the model described by $H_F = H_F^{(1)} + H_F^{(2)}$ is called the Floquet magnon Chern insulator (FMCI).

Appendix D
Details on the analytics of the cAA model and relations with graphene

In the main text we have presented the superspace model in the vanishing field limit without much discussion of its derivation. In this Appendix, we provide a quick and simple derivation, starting from the Hamiltonian which realizes, for a fixed δ, a physical implementation of the cAA model. It reads

$$\begin{aligned} H(\delta) = &- \sum_n \left[t_1 + \Delta_1 \cos\left(2\pi b n - \delta\right)\right] a_n^\dagger b_n \\ &+ \left[t_2 + \Delta_2 \cos\left(2\pi b n - \delta\right)\right] b_n^\dagger a_{n+1} + \text{h.c.}, \end{aligned} \tag{D.1}$$

The very simple trick which allows us to generate the 2D superspace model is to expand the cosine modulations in terms of exponentials and allow, in the vanishing field limit $b \to 0$, the dependence on b to drop out from the Hamiltonian, yielding a $b-$independent Hamiltonian.

$$\begin{aligned} H(\delta) = &- \sum_n \left[t_1 + \frac{\Delta_1}{2}\left(e^{i\delta} + e^{-i\delta}\right)\right] a_n^\dagger b_n \\ &+ \left[t_2 + \frac{\Delta_2}{2}\left(e^{i\delta} + e^{-i\delta}\right)\right] b_n^\dagger a_{n+1} + \text{h.c.}, \end{aligned} \tag{D.2}$$

The fact that this form of the Hamiltonian is a good description of the model can be checked numerically, by setting, for instance $b = 1/1001$, which produces results for the 1D topology practically indistinct from the vanishing field limit. The idea now is to imagine that δ plays the role of a momentum variable, and promote the creation and annihilation operators into objects with two indices. The first is n, the lattice site along physical space which for the sake of clarity we rename to i to better signify this change to a 2D model, and the second one is j which is the position along the synthetic dimension, conjugate to the momentum δ. So, the aim is to transform $a_n^\dagger$ and $b_n^\dagger$ as

$$a_n^\dagger \to \sum_j a_{i,j}^\dagger e^{-i\delta j}, \tag{D.3}$$

$$b_n^\dagger \to \sum_j b_{i,j}^\dagger e^{-i\delta j}, \tag{D.4}$$

and account for the already existing exponentials $e^{\pm i\delta}$ as indicators of the existence of couplings in the synthetic direction. To see why this can be done, simply note that it is possible to write

$$\begin{aligned} a_i^\dagger b_i e^{-i\delta} &= \sum_{j,j'} b_{i,j'}^\dagger e^{-i\delta j'} a_{i,j} e^{i\delta j} e^{-i\delta}. \\ &= \sum_{j,j'} b_{i,j'}^\dagger a_{i,j} e^{-i\delta(j'+1)} e^{i\delta j} \\ &= \sum_j b_{i,j}^\dagger a_{i,j+1}. \end{aligned} \tag{D.5}$$

Thus, the Hamiltonian of the system can be brought into 2D by splitting up the terms proportional to $e^{\pm i\delta}$, adding a summation in the synthetic dimension, an adjusting for the synthetic couplings generated as in equation (D.5). This procedure results in equation (4.2) of the main text, which we repeat here for convenience.

$$\begin{aligned} H_{\text{2D}} = &- \sum_{i,j} t_1 a_{i,j}^\dagger b_{i,j} + \Delta_1' a_{i,j}^\dagger b_{i,j+1} + \text{h.c.} \\ &- \sum_{i,j} t_1 b_{i,j}^\dagger a_{i+1,j} + \Delta_2' b_{i,j}^\dagger a_{i+1,j+1} + \text{h.c.}, \end{aligned} \tag{D.6}$$

This concludes this small derivation of the 2D superspace model in a "real space" representation. The generated hoppings are "diagonal" in the 2D lattice, as illustrated in Fig. 11 of the main text. Instead of choosing this representation, we can instead go into momentum space in both physical and synthetic dimensions. This amounts to performing the transformation

$$a_n^\dagger \to \sum_k a_k^\dagger e^{ikn}, \tag{D.7}$$

$$b_n^\dagger \to \sum_k b_k^\dagger e^{ikn}, \tag{D.8}$$

which leads to, summing over all possible values of δ in order to take into account the synthetic dimension

$$H_{2D} = \sum_{k,\delta} \left[t_1 + \Delta_1 \cos\delta\right] a_k^\dagger b_k + \left[t_2 + \Delta_2 \cos\delta\right] b_k^\dagger a_k e^{ik} + \text{h.c.}, \tag{D.9}$$

A more convenient form is the Hamiltonian matrix which was described in the main text

$$H_{2D}(\boldsymbol{k}) = -\left[t_1 + \Delta_1' \cos\delta + (t_2 + \Delta_2' \cos\delta)\cos k\right]\sigma_x - \left[(t_2 + \Delta_2' \cos\delta)\sin k\right]\sigma_y. \tag{D.10}$$

It is also worth remarking that the role played by the additional exponentials $e^{\pm i2\pi bn}$ is to introduce additional phases along these hoppings, which explicitly break translational symmetry. Despite this, the position dependence on n is precisely what makes the system exactly mappeable to an IQHE model in the Landau gauge. As we show in the main text, this limit can be analyzed numerically with topological markers.

Finally, as discussed in the main text, underlying the cAA model and the richness of topological quasicrystals in general is the idea of synthetic dimensions. The procedure of mapping the cAA model into a superspace model involves taking a model parameter, in this case. the modulation shift, and interpreting it as a momentum variable. This generates a higher dimensional model with an additional synthetic dimension. The opposite procedure can be performed, and the secondary role of this Appendix is to illustrate it via the example of graphene. Starting with a physical 2D model and perform a process of dimensional reduction, by reinterpreting a momentum variable as an adjustable parameter.

A simple example of this procedure, but which is often overlooked is a zig-zag edge graphene ribbon. Like the cAA model, zig-zag graphene has two sublattices A and B and, for a ribbon with N unit cells in the finite direction, the Hamiltonian is of form

$$H_{\text{g}} = -t\sum_{i=1}^{\infty}\sum_{j=1}^{N} a_{i,j}^\dagger b_{i,j} + b_{i,j}^\dagger a_{i,j+1} + b_{i,j}^\dagger a_{i+1,j} + \text{h.c.}. \tag{D.11}$$

It is then possible to Fourier transform this Hamiltonian along the infinite direction, introducing the momentum variable k, resulting in

$$H_g = -t\sum_{k}\sum_{j=1}^{N} 2\cos\left(\frac{\sqrt{3}}{2}k\right) a_{k,j}^\dagger b_{k,j} + b_{k,j}^\dagger a_{k,j+1} + \text{h.c.}. \tag{D.12}$$

If we ignore the summation in k, the Hamiltonian is simply that of a finite SSH chain with hoppings modulated by the momentum k. Thus, from the 2D graphene lattice we have constructed a modulated

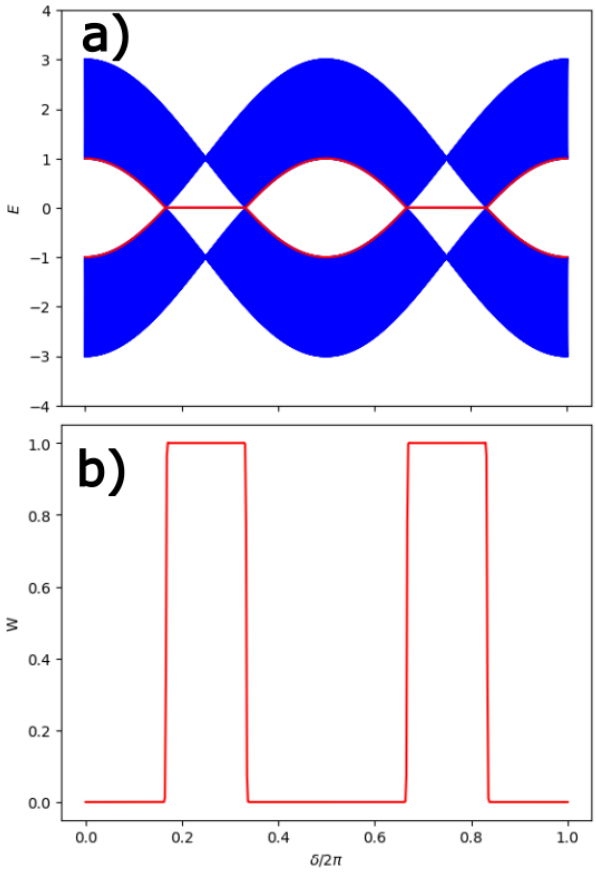

Figure 24: (a) Energy spectrum for a graphene Zig-zag ribbon, simulated using the cAA model. (b) Winding number of the SSH model resulting from dimensional reduction of the zig-zag graphene ribbon. We have $W(\delta) = 1$ when doubly degenerate edge states are present, and $W(\delta) = 0$ when the states wander into the bulk.

1D SSH model via a process of dimensional reduction. A winding number can be associated to this SSH model, and the winding number indicates the presence of the characteristic degenerate edge modes at zero energy. This is a topological interpretation of this phenomena which is often overlooked. In Fig. 24, we present the result of using the winding number topological marker presented in the main text to compute the topological invariant of the SSH model resulting from the dimensional reduction procedure when applied to a graphene zig-zag ribbon.

Finally, note that graphene can actually be mapped to a particular parameter set of the cAA model. By picking physical hoppings $t_1 = \Delta_2 = 0$, $t_2 = t$, and $\Delta_1 = 2t$, as well as a value of $b = 0$ and identifying $\sqrt{3}k/2$ with the shift δ, we can simulate graphene in the cAA model. Since graphene appears in the limit of $b = 0$, the parameter δ does not exactly play the role of a shift of the potential, but rather, by itself, it globally reduces or increases the strength of the intra-cell hopping. The connection between these models therefore definitely exists, however, the fact that no actual Aubry-André periodic modulation is present removes many of the puzzling features of the cAA model. Nonetheless, this correspondence

establishes that the concept of synthetic dimensions can be utilized, in principle, to simulate a graphene lattice in a 1D model, by accessing slices of its spectrum and tuning interaction strengths to move along the momentum direction.

Appendix E
Details on Topological Markers

This Appendix serves as a brief overview of 1D and 2D topological markers, with a very short outline of the derivation of Chen's universal topological marker [93] and Barnett and Sykes' quasicrystal markers [161]. Both approaches make use of an idea originally devised by Bianco and Resta [199], which is that the topological invariants characterizing the Hamiltonian can be represented in terms of projectors onto occupied states. One can find such representations assuming that the Hamiltonian can be represented in momentum space in some way, but even this is not the case, the projectors which are initially written as integrals over some Brillouin zone, can equivalently be written in terms of projectors onto occupied states in their real-space representation, and all formulas hold equivalently. This replacement of projectors in terms of states in real space makes it so that the obtained topological invariants can be computed even if a Brillouin zone cannot be constructed at all, such as when do not host translational symmetry.

Chen's formula for the universal topological marker relies on the fact that for Dirac models, for all dimensions d and symmetry classes, there exists a universal formula for the Chern, winding and $\mathbb{Z}_2$ invariant: If one considers the spectrally flattened Dirac Hamiltonian in momentum space $\widetilde{H}(\boldsymbol{k}) = \boldsymbol{n}(\boldsymbol{k}) \cdot \boldsymbol{\Gamma}$, where $\boldsymbol{n}(\boldsymbol{k}) = (n_1(\boldsymbol{k}), \ldots, n_d(\boldsymbol{k}))$ is a vector normalized to unity containing all momentum dependence of the Hamiltonian, and $\boldsymbol{\Gamma}$ contains all of the $2n$ Dirac matrices of n-th order, which satisfy the Clifford algebra [159]. One can then compute the degree of the mapping $\boldsymbol{n} : BZ \to S^d$, where BZ stands for the Brillouin zone (which is isomorphic to the $d-$torus T^d), and where S^d is simply the $d-$sphere spanned by the vector $\boldsymbol{n}(\boldsymbol{k})$. The degree of $\boldsymbol{n}$ is given by

$$\deg[\boldsymbol{n}] = \frac{1}{V_d} \int d^d\boldsymbol{k} \varepsilon_{i_0,\ldots i_d} n^{i_0} \partial_1 n^{i_1} \ldots \partial_d n^{i_d}, \tag{E.1}$$

where ε is the fully anti-symmetric tensor on the $d+1-$symbols $i_0, \ldots, i_d$, and $\partial_i = \partial/\partial k_i$. The integrand is simply the Jacobian $J_{\boldsymbol{k}}$ of the map $\boldsymbol{n}(\boldsymbol{k})$. The derivation of the formula given in the equation (4.16) of the main text, for the universal topological operator, and the respective marker, then goes through several steps: The first of which is establishing the fact that the Jacobian can be written a trace of a quantity involving the full Hamiltonian matrix $\widetilde{H}(\boldsymbol{k})$, as well as $\mathcal{W} = \Gamma_{d+1}\Gamma_{d+2}\cdots\Gamma_{2n}$, the product of

unused Dirac matrices in the model. This quantity $\mathcal{W}$ crops up because one makes use of the identity $\mathrm{tr}\left[\Gamma_0\Gamma_1\ldots\Gamma_{2n}\right] = 2^n c$ to simplify equation (E.1), but only d Dirac matrices are actually present in the Hamiltonian. The constant $c = \{1, -1, i, -i\}$ depends on the representation of the Dirac matrices, but eventually is absorbed into a normalization factor. One can find, after some simplifications,

$$\deg\left[\boldsymbol{n}\right] = \frac{(2\pi)^d}{2^n c V_D}\int \frac{d^d\boldsymbol{k}}{(2\pi)^d}\mathrm{tr}\left[\mathcal{W}\widetilde{H}(\boldsymbol{k})\partial_1\widetilde{H}(\boldsymbol{k})\ldots\partial_d\widetilde{H}(\boldsymbol{k})\right], \tag{E.2}$$

and now Bianco and Resta's idea can be put to use by writing the spectrally flattened Hamiltonian as $\widetilde{H} = Q - P$, where P projects into occupied bands

$$P = \int \frac{d^d\boldsymbol{k}}{(2\pi)^d}\sum_{n\ \mathrm{occ.}} \left|n(\boldsymbol{k})\right\rangle\left\langle n(\boldsymbol{k})\right|, \tag{E.3}$$

and $Q = \mathbb{1} - P$ is its complementary projector into unoccupied bands. Chen showed [93] that equation (E.1) can be written in terms of an alternating product of P and Q by making use of the position space representation of $\partial_x \equiv -i\hat{x}$. Looking at even and odd dimensions separately, Chen showed that it is possible to represent

$$\begin{aligned}
&\int \frac{d^d\boldsymbol{k}}{(2\pi)^d}\mathrm{tr}\left[\mathcal{W}\widetilde{H}(\boldsymbol{k})\partial_1\widetilde{H}(\boldsymbol{k})\ldots\partial_d\widetilde{H}(\boldsymbol{k})\right]_{d\ \mathrm{even}} \\
=&2^d i\mathrm{tr}\left[\mathcal{W}Q\hat{x}_1P\hat{x}_2\ldots Q\hat{x}_dP + \mathcal{W}P\hat{x}_1Q\hat{x}_2\ldots P\hat{x}_dQ\right], \qquad \text{(E.4)} \\
&\int \frac{d^d\boldsymbol{k}}{(2\pi)^d}\mathrm{tr}\left[\mathcal{W}\widetilde{H}(\boldsymbol{k})\partial_1\widetilde{H}(\boldsymbol{k})\ldots\partial_d\widetilde{H}(\boldsymbol{k})\right]_{d\ \mathrm{odd}} \\
=&2^d\mathrm{tr}\left[\mathcal{W}Q\hat{x}_1P\hat{x}_2\ldots P\hat{x}_dQ - \mathcal{W}P\hat{x}_1Q\hat{x}_2\ldots Q\hat{x}_dP\right], \qquad \text{(E.5)}
\end{aligned}$$

and therefore, construct a universal topological operator

$$\begin{aligned}
\hat{C} =& N_D\mathcal{W}Q\hat{x}_1P\hat{x}_2\ldots\hat{x}_dO, \\
&+ (-1)^{d+1}N_D W P\hat{x}_1Q\hat{x}_2\ldots\hat{x}_dO'
\end{aligned} \tag{E.6}$$

where the products terminate on $O = P$ and $O' = Q$ if d is odd, or $O = Q$ and $O' = P$ if d is even. The factor N_D absorbs the constant $c = \mathrm{tr}\left[\Gamma_0\Gamma_1\ldots\Gamma_{2n}\right]/2^n$ as well as additional factors of 2π, in the form of $V_d = (2\pi)^d$, and is explicitly given by

$$N_D = \frac{i^d 2^{2d-n}\pi^d}{cV_d}. \tag{E.7}$$

	Top. Inv.		
Sym. Class	$d=1$	2	3
A	0	$\deg\left[\hat{\boldsymbol{h}}\right]$	0
AIII	$\deg\left[\hat{\boldsymbol{h}}\right]$	0	$\deg\left[\hat{\boldsymbol{h}}\right]$
AI	0	0	0
BDI	$\deg\left[\hat{\boldsymbol{h}}\right]$	0	0
D	$(-1)^{\deg[\hat{\boldsymbol{h}}]}$	$\deg\left[\hat{\boldsymbol{h}}\right]$	0
DIII	$(-1)^{\deg[\hat{\boldsymbol{h}}]}$	$(-1)^{\deg[\hat{\boldsymbol{h}}]}$	$\deg\left[\hat{\boldsymbol{h}}\right]$
AII	0	$(-1)^{\deg[\hat{\boldsymbol{h}}]}$	$(-1)^{\deg[\hat{\boldsymbol{h}}]}$
CII	$2\deg\left[\hat{\boldsymbol{h}}\right]$	0	$(-1)^{\deg[\hat{\boldsymbol{h}}]}$
C	0	$2\deg\left[\hat{\boldsymbol{h}}\right]$	0
CI	0	0	$2\deg\left[\hat{\boldsymbol{h}}\right]$

Table 4: Table containing the first three dimensions of the periodic table of topological insulators and superconductors with topological invariants expressed in terms of the degree of the normalized Dirac vector $\hat{\boldsymbol{n}}$.

Replacing the trace over the degrees of freedom with a trace over real space cells, the projectors into projectors into real space states with energy less than a certain Fermi energy, as in equation (4.17) of the main text, and normalizing the expression over the size of the unit-cell L_d, one finds

$$\deg\left[\boldsymbol{n}\right] = \frac{1}{L_d}\mathrm{tr}\left[\hat{C}\right]. \tag{E.8}$$

This can be understood, as in the main text, as a summation of a local topological marker $C = \sum_{\boldsymbol{x}} \langle \boldsymbol{x}| \hat{C} |\boldsymbol{x}\rangle = \sum_{\boldsymbol{x}} \mathcal{C}(\boldsymbol{x})$ over internal sites of each unit cell. When the switch to a real space representation is performed, one instead performs the trace of the topological operator over a finite region $\mathcal{R}$ deep in the bulk for translationally invariant systems, so as to avoid the behavior of the local topological marker at the edges. This can be interpreted as summing the local topological over this region. The topological invariants for the different Altland-Zirnbauer periodic table of topological insulators can finally be calculated from $\deg\left[\boldsymbol{n}\right]$. Namely, one can make use of Table 4

The relevant classes for the main text are the BDI class in $d=1$ for the SSH model used in Chapter 4, as well as the the A class in $d=2$ for the Haldane model used in Chapter 5. In the former case, for the BDI class 1D, the topological operator is given by

$$\hat{C}^{d=1}_{\mathrm{BDI}} = \sigma_z\left[Q\hat{x}P + P\hat{x}Q\right]. \tag{E.9}$$

The operator σ_z acts within the sublattice degree of freedom of the SSH model. In the latter case, for the A class in $d = 2$ the topological operator reads

$$\hat{C}_{\mathsf{A}}^{d=2} = 2\pi i \mathbb{1} \left[Q\hat{x}PyQ - P\hat{x}QyP \right]. \tag{E.10}$$

As described above, both of these topological operators are traced over regions deep in the bulk to find the corresponding topological invariant.

Appendix F
Green's function theory for the Dirac Magnon Chern Insulator

In this Appendix I go over the equation of motion method used in deriving the Green's function (GF) for the Dirac magnon Chern insulator (DMCI) without any external perturbation. This method is exact and it dually serves as a brief recap on the theory of GFs. Firstly, however, in order to introduce the necessary notation, it is worth recalling that a DMCI is described by a ferromagnetic Heisenberg model defined for the honeycomb lattice, with nearest neighbor interactions and a Dzyaloshinskii-Moriya interaction. It can be written as

$$\begin{aligned} H = & -J \sum_{\langle i,j \rangle} \boldsymbol{S}(\boldsymbol{r}_i) \cdot \boldsymbol{S}(\boldsymbol{r}_j) \\ & + J_{DM} \sum_{\langle\langle i,j \rangle\rangle} D_{ij} \hat{\boldsymbol{z}} \cdot [\boldsymbol{S}_A(\boldsymbol{r}_i) \times \boldsymbol{S}_A(\boldsymbol{r}_j)] \qquad \text{(F.1)} \\ & + J_{DM} \sum_{\langle\langle i,j \rangle\rangle} D_{ji} \hat{\boldsymbol{z}} \cdot [\boldsymbol{S}_B(\boldsymbol{r}_i) \times \boldsymbol{S}_B(\boldsymbol{r}_j)] \,, \qquad \text{(F.2)} \end{aligned}$$

The cross product reads

$$\begin{aligned} \hat{\boldsymbol{z}} \cdot (\boldsymbol{S}(\boldsymbol{r}_i) \times \boldsymbol{S}(\boldsymbol{r}_j)) &= \hat{\boldsymbol{z}} \cdot \begin{vmatrix} \hat{\boldsymbol{x}} & \hat{\boldsymbol{y}} & \hat{\boldsymbol{z}} \\ S^x(\boldsymbol{r}_i) & S^y(\boldsymbol{r}_i) & S^z(\boldsymbol{r}_i) \\ S^x(\boldsymbol{r}_j) & S^y_j & S^z_j \end{vmatrix} \\ &= S^x(\boldsymbol{r}_i) S^y(\boldsymbol{r}_j) - S^y(\boldsymbol{r}_i) S^x(\boldsymbol{r}_j). \end{aligned}$$

Since the $S^x(\boldsymbol{r}_i)$ and $S^y(\boldsymbol{r}_i)$ can be expressed as

$$S^x(\boldsymbol{r}_i) = \frac{S^+(\boldsymbol{r}_i) + S^-(\boldsymbol{r}_i)}{2}, \qquad \text{(F.3)}$$

$$S^y(\boldsymbol{r}_i) = i\frac{S^-(\boldsymbol{r}_i) - S^+(\boldsymbol{r}_i)}{2}, \qquad \text{(F.4)}$$

in terms of spin-ladder operators, one finds

$$\begin{aligned} S^x(\boldsymbol{r}_i)S^y(\boldsymbol{r}_j) - S^y(\boldsymbol{r}_i)S^x(\boldsymbol{r}_j) =& \frac{i}{4}\left(S^+(\boldsymbol{r}_i) + S^-(\boldsymbol{r}_i)\right)\left(S^-(\boldsymbol{r}_j) - S^+(\boldsymbol{r}_j)\right) \\ & - \frac{i}{4}\left(S^-(\boldsymbol{r}_i) - S^+(\boldsymbol{r}_i)\right)\left(S^+(\boldsymbol{r}_j) + S^-(\boldsymbol{r}_j)\right) \\ =& \frac{i}{2}\left(S^+(\boldsymbol{r}_i)S^-(\boldsymbol{r}_j) - S^-(\boldsymbol{r}_i)S^+(\boldsymbol{r}_j)\right). \end{aligned} \tag{F.5}$$

This results in

$$\begin{aligned} H =& -J\sum_{\langle i,j\rangle} S^z_A(\boldsymbol{r}_i)S^z_B(\boldsymbol{r}_i) + \frac{1}{2}\left[S^+_A(\boldsymbol{r}_i)S^-_B(\boldsymbol{r}_j) + S^-_A(\boldsymbol{r}_i)S^+_B(\boldsymbol{r}_j)\right] \\ &+ J_{DM}\frac{i}{2}\sum_{\langle\langle i,j\rangle\rangle} D_{ij}\left[S^+_A(\boldsymbol{r}_i)S^-_A(\boldsymbol{r}_j) - S^-_A(\boldsymbol{r}_i)S^+_A(\boldsymbol{r}_j)\right] \\ &+ J_{DM}\frac{i}{2}\sum_{\langle\langle i,j\rangle\rangle} D_{ji}\left[S^+_B(\boldsymbol{r}_i)S^-_B(\boldsymbol{r}_j) - S^-_B(\boldsymbol{r}_i)S^+_B(\boldsymbol{r}_j)\right]. \end{aligned} \tag{F.6}$$

Using the linearized Holstein-Primakoff (HP) transformations, and keeping only terms quadratic in the spin-operators, such a Hamiltonian can be written position space as

$$\begin{aligned} H_0 =& -JNS^2z - JS\sum_{\langle i,j\rangle}\left(a^\dagger_j b_i + b^\dagger_i a_j - a^\dagger_i a_i - b^\dagger_j b_j\right) \\ &+ J_{DM}Si\sum_{\langle\langle i,j\rangle\rangle} D_{ij}\left[a^\dagger_j a_i - a^\dagger_i a_j\right] && \text{(F.7)} \\ &+ J_{DM}Si\sum_{\langle\langle i,j\rangle\rangle} D_{ji}\left[b^\dagger_j b_i - b^\dagger_i b_j\right] && \text{(F.8)} \\ \equiv& -JS\sum_{\langle i,j\rangle}\left(a^\dagger_j b_i + b^\dagger_i a_j - a^\dagger_i a_i - b^\dagger_j b_j\right) && \text{(F.9)} \\ &+ 2J_{DM}Si\sum_{\langle\langle i,j\rangle\rangle}\nu_{ij}\left[a^\dagger_i a_j - b^\dagger_i b_j\right]. && \text{(F.10)} \end{aligned}$$

which a Hamiltonian exactly identical to the Haldane model with a flux $\phi = \pi/2$, corresponding to purely imaginary NNN hoppings. The main objects necessary for the discussion both here and the main text are the retarded GFs, $G^{AA}_{ij}(t), G^{BA}_{ij}(t), G^{AB}_{ij}(t)$ and $G^{BB}_{ij}(t)$ defined explicitly in equation (5.11), and which can be grouped together in matrix form as in equation (5.13). In this Appendix, I arrive at some expression for the matrix GF G_0 for the DMCI in the absence of any external perturbations. As such, it is useful to start with the equation of motion for G^{AA}_{ij}, for which the equations of motion for the HP operators are needed, given by the Heisenberg equations

$$\begin{aligned}\frac{d}{dt}a_i(t) =& i\left[H, a_i\right] \\ =& iJSza_i - iJS\sum_{k\in V(i)} b_k - 2J_{DM}S\sum_{k\in V_2(i)}\nu_{ik}a_k, \end{aligned} \tag{F.11}$$

$$\begin{aligned}\frac{d}{dt}b_i(t) =& i\left[H, b_i\right] \\ =& iJSzb_l - iJS\sum_{l\in V(i)} a_l + 2J_{DM}S\sum_{k\in V_2(i)}\nu_{ik}b_k. \end{aligned} \tag{F.12}$$

Here, I have employed the notation $V(i)$ to denote the set of nearest neighbors of the site i, and $V_2(i)$ to denote the set of second nearest neighbors. Using these equations, it is simple to show that

$$\frac{d}{dt}G_{ij}^{AA}(t) = -i\delta(t) + iJSzG_{ij}^{AA}(t) - iJS\sum_{k\in V(i)} G_{kj}^{BA}(t) - 2J_{DM}S\sum_{k\in V_2(i)}\nu_{ik}G_{kj}^{AA}(t), \tag{F.13}$$

$$\frac{d}{dt}G_{ij}^{BA}(t) = iJSzG_{ij}^{BA}(t) - iJS\sum_{k\in V(i)} G_{kj}^{AA}(t) + 2J_{DM}S\sum_{k\in V_2(i)}\nu_{ik}G_{kj}^{BA}(t) + iB\delta_{i0}G_{0j}^{BA}(t). \tag{F.14}$$

$$\frac{d}{dt}G_{ij}^{AB}(t) = iJSzG_{ij}^{AB}(t) - iJS\sum_{k\in V(i)} G_{kj}^{BB}(t) - 2J_{DM}S\sum_{k\in V_2(i)}\nu_{ik}G_{kj}^{AB}(t), \tag{F.15}$$

$$\frac{d}{dt}G_{ij}^{BB}(t) = -i\delta(t) + iJSzG_{ij}^{BB}(t) - iJS\sum_{k\in V(i)} G_{kj}^{AB}(t) + 2J_{DM}S\sum_{k\in V_2(i)}\nu_{ik}G_{kj}^{BB}(t). \tag{F.16}$$

Note that only the AA and BB GFs include Dirac delta function terms. One can transform these equations into frequency space, which renders it possible to transform the differential equations into a set of coupled linear equations

$$\omega G_{ij}^{BB}(\omega) = 1 - JSzG_{ij}^{BB}(\omega) + JS\sum_{k\in V(i)} G_{kj}^{AB}(\omega) + i2J_{DM}S\sum_{k\in V_2(i)}\nu_{ik}G_{kj}^{BB}(\omega), \tag{F.17}$$

$$\omega G_{ij}^{AA}(\omega) = 1 - JSzG_{ij}^{AA}(\omega) + JS\sum_{k\in V(i)} G_{kj}^{BA}(\omega) - i2J_{DM}S\sum_{k\in V_2(i)}\nu_{ik}G_{kj}^{AA}(\omega), \tag{F.18}$$

$$\omega G_{ij}^{BA}(\omega) = -JSzG_{ij}^{BA}(\omega) + JS\sum_{k\in V(i)} G_{kj}^{AA}(\omega) + i2J_{DM}S\sum_{k\in V_2(i)}\nu_{ik}G_{kj}^{BA}(\omega), \tag{F.19}$$

$$\omega G_{ij}^{AB}(\omega) = -JSzG_{ij}^{AB}(\omega) + JS\sum_{k\in V(i)} G_{kj}^{BB}(\omega) - i2J_{DM}S\sum_{k\in V_2(i)}\nu_{ik}G_{kj}^{AB}(\omega). \tag{F.20}$$

These equations can furthermore be double-Fourier transformed into momentum space quite generically via

$$G^{\alpha\beta}_{\boldsymbol{k}_1,\boldsymbol{k}_2}(\omega) = \sum_i e^{i\boldsymbol{k}_1\cdot\boldsymbol{R}_i} e^{-i\boldsymbol{k}_2\cdot\boldsymbol{R}_j} G^{\alpha\beta}_{ij}(\omega). \tag{F.21}$$

Furthermore, it is useful to introduce here what are often called the structure factors

$$\gamma(\boldsymbol{k}) = \frac{1}{z}\sum_{i=1}^{3} e^{-i\boldsymbol{k}\cdot\boldsymbol{\delta}}, \tag{F.22}$$

$$\xi(\boldsymbol{k}) = \frac{1}{z}\sum_{i=1}^{3} 2i\sin\left(\boldsymbol{k}\cdot\boldsymbol{a}_i\right). \tag{F.23}$$

In momentum and frequency space, the equations of motion simply read, at the cost of the structure factors

$$\omega G^{BB}_{\boldsymbol{k}_1,\boldsymbol{k}_2}(\omega) = N\delta_{\boldsymbol{k}_1,\boldsymbol{k}_2} - JSzG^{BB}_{\boldsymbol{k}_1,\boldsymbol{k}_2}(\omega) + JSz\gamma^*(\boldsymbol{k}_1)G^{AB}_{\boldsymbol{k}_1\boldsymbol{k}_2}(\omega) + 2iJ_{DM}Sz\xi(\boldsymbol{k}_1)G^{BB}_{\boldsymbol{k}_1\boldsymbol{k}_2}(\omega), \tag{F.24}$$

$$\begin{aligned}\omega G^{BA}_{\boldsymbol{k}_1,\boldsymbol{k}_2}(\omega) = &- JSzG^{BA}_{\boldsymbol{k}_1,\boldsymbol{k}_2}(\omega) + JSz\gamma^*(\boldsymbol{k}_1)G^{AA}_{\boldsymbol{k}_1\boldsymbol{k}_2}(\omega) + 2iJ_{DM}Sz\xi(\boldsymbol{k}_1)G^{BA}_{\boldsymbol{k}_1\boldsymbol{k}_2}(\omega)\\ &- B\frac{1}{N}\sum_{\boldsymbol{k}} G^{BA}_{\boldsymbol{k}\boldsymbol{k}_2}(\omega),\end{aligned} \tag{F.25}$$

$$\omega G^{AA}_{\boldsymbol{k}_1,\boldsymbol{k}_2}(\omega) = N\delta_{\boldsymbol{k}_1,\boldsymbol{k}_2} - JSzG^{AA}_{\boldsymbol{k}_1,\boldsymbol{k}_2}(\omega) + JSz\gamma(\boldsymbol{k}_1)G^{BA}_{\boldsymbol{k}_1,\boldsymbol{k}_2}(\omega) - 2iJ_{DM}Sz\xi(\boldsymbol{k}_1)G^{AA}_{\boldsymbol{k}_1,\boldsymbol{k}_2}(\omega), \tag{F.26}$$

$$\omega G^{AB}_{\boldsymbol{k}_1,\boldsymbol{k}_2}(\omega) = - JSzG^{AB}_{\boldsymbol{k}_1,\boldsymbol{k}_2}(\omega) + JSz\gamma(\boldsymbol{k}_1)G^{BB}_{\boldsymbol{k}_1,\boldsymbol{k}_2}(\omega) - 2iJ_{DM}Sz\xi(\boldsymbol{k}_1)G^{AB}_{\boldsymbol{k}_1,\boldsymbol{k}_2}(\omega). \tag{F.27}$$

Grouping every equation together into the convenient form of a matrix equality, one finds

$$\begin{bmatrix} \omega - JSz - 2iJ_{DM}Sz\xi(\boldsymbol{k}_1) & JSz\gamma(\boldsymbol{k}_1) \\ JSz\gamma^*(\boldsymbol{k}_1) & \omega - JSz + 2iJ_{DM}Sz\xi(\boldsymbol{k}_1) \end{bmatrix} G_{\boldsymbol{k}_1,\boldsymbol{k}_2}(\omega) = N\delta_{\boldsymbol{k}_1,\boldsymbol{k}_2}\begin{bmatrix} 1 & 0 \\ 0 & 1 \end{bmatrix}. \tag{F.28}$$

This leads to a natural definition of the zeroth order GF

$$\left[G^0_{\boldsymbol{k}_1}(\omega)\right]^{-1} \equiv \begin{bmatrix} \omega - JSz - 2iJ_{DM}Sz\xi(\boldsymbol{k}_1) & JSz\gamma(\boldsymbol{k}_1) \\ JSz\gamma^*(\boldsymbol{k}_1) & \omega - JSz + 2iJ_{DM}Sz\xi(\boldsymbol{k}_1) \end{bmatrix}. \tag{F.29}$$

In the absence of any perturbation to the system, equation (F.28) says that the total GF is simply given by the unperturbed GF $G_{\boldsymbol{k}_1,\boldsymbol{k}_2}(\omega) = N\delta_{\boldsymbol{k}_1,\boldsymbol{k}_2}G^0_{\boldsymbol{k}_1}(\omega)$.

Work performed in the framework of the project CERN/FIS-COM/0004/2021 funded by the Portuguese Foundation for Science and Technology (FCT)